

Christoph Kords

On the role of dislocation transport in the constitutive description of crystal plasticity

ON THE ROLE OF DISLOCATION TRANSPORT IN
THE CONSTITUTIVE DESCRIPTION OF
CRYSTAL PLASTICITY

Von der Fakultät für Georessourcen und Materialtechnik
der Rheinisch-Westfälischen Technischen Hochschule Aachen

zur Erlangung des akademischen Grades eines
Doktors der Ingenieurwissenschaften

genehmigte Dissertation

vorgelegt von **Dipl.-Ing.**

Christoph Kords

aus Walsrode

Berichter: Prof. Dr.-Ing. Dierk Raabe
PD Dr. rer. nat. Franz Roters
Univ.-Prof. Dr. rer. nat. Dr. h. c. Günter Gottstein

Tag der mündlichen Prüfung: 28.August.2013

Diese Dissertation ist auf den Internetseiten der Hochschulbibliothek online verfügbar

Copyright © 2013 Christoph Kords

Printed and published by epubli GmbH, Berlin, www.epubli.de

ISBN 978-3-8442-7741-8

Acknowledgments

This work summarizes most of the research that I have done during my PhD time at the Max-Planck-Institut für Eisenforschung (MPIE) in Düsseldorf, Germany, in the Department for Microstructure Physics and Alloy Design.

First of all, I would like to thank Prof. Dierk Raabe for giving me the opportunity to pursue my PhD at his department, where I not only found excellent facilities to explore the fascinating world of materials science, but also an inspiring and convivial atmosphere. Many thanks go to Dr. Philip Eisenlohr, who initiated my PhD project, and Dr. Franz Roters for letting me be part of the simulation and theory group; their support and expertise have been most important for developing this work. I would also like to thank my examination committee consisting of the advisors Prof. Dierk Raabe, Dr. Franz Roters, and Prof. Günter Gottstein and the chairman Prof. Reinhard Conradt.

Secondly, I would like to thank all those who helped to realize this work, be it with technical support, discussions, or proofreading. Special thanks go to the development group of the simulation toolbox DAMASK, which the presented model is part of, and, in particular, to Martin Diehl and Dr. Pratheek Shanthraj, who implemented most of the spectral solver part. Furthermore, I would like to thank Prof. Bob Svendsen for enlightening discussions and his critical comments about the model. I owe thanks to Prof. Jeffrey Kysar and Dr. Jui-Chao Kuo for their well-thought experiments, which served as a major source for the validation of the simulation results.

My time at the MPIE has not only increased my knowledge about materials science, but also personally enriched my life. I would like to thank all my friends, colleagues and former colleagues at the MPIE for making this PhD project such a wonderful experience; I really enjoyed working with you.

I sincerely thank my family for their lifelong support and their confidence in me: my parents Christian and Elisabeth Kords, without whom all this would not have been possible, and my sisters Barbara Kords and Henrike Fink. Last, but not least, I would like to express me deepest gratitude to the two most important persons in my life: Silja and our little son Emil; your smiles are an eternal source of energy and motivation for me even when I cannot be with you.

Contents

Introduction and background 13

1 Introduction 15

2 Background 19

- 2.1 The ideal crystal 19
- 2.2 Defects in real crystals 20
- 2.3 Continuum mechanical framework of deformation 22
- 2.4 Connection between kinematics and dislocation content 23

Theory 25

3 Constitutive laws 27

- 3.1 Parametrization of microstructure 27
- 3.2 Microstructure evolution 30
- 3.3 Dislocation kinetics 37

4 Implementation 43

- 4.1 Solution of the mechanical boundary value problem 43
- 4.2 Coupling of elasticity and plasticity 45
- 4.3 Internal state variables 54

Validation and comparison to experiments 59

5 Validation of the dislocation transport equations 61

- 5.1 Problem setup 61
- 5.2 Results 63
- 5.3 Discussion 64
- 5.4 Conclusions 67

6 Comparison of discrete and continuum dislocation dynamics simulations 69

- 6.1 Problem setup 69
- 6.2 Comparison of DDD and CDD simulation results for a plastic inclusion under different external stresses 73
- 6.3 Geometric invariance 79
- 6.4 Kinematic invariance 82
- 6.5 Influence of dislocation correlation 85
- 6.6 Conclusions 90

7 Simple shear of an Aluminum bi-crystal with a small angle tilt grain boundary 93

7.1 Problem setup 93

7.2 Results 95

7.3 Discussion 100

7.4 Conclusions 102

8 Indentation of single-crystalline nickel with a wedge indenter 105

8.1 Problem setup 106

8.2 Results 107

8.3 Discussion 114

8.4 Conclusions 121

Summary and outlook 123

9 Summary and outlook 125

Appendix 129

A Additional material 131

A.1 Stress and strain measures 131

A.2 Stress field of a straight edge and screw dislocation 131

A.3 Stable dislocation dipole height 132

A.4 Partial derivative of the plastic velocity gradient 132

A.5 Analysis of the linearized partial differential equation for a dislocation flux with flowstress 133

A.6 Active slip systems in an fcc crystal under line load in $[110]$ direction 135

A.7 Geometrically necessary dislocation density derived from plastic shear gradients 136

A.8 Efficient cutback algorithm 137

B Notation and tensor operations 141

Bibliography 143

Abstract 151

Zusammenfassung 153

Nomenclature

Acronyms and abbreviations

bcc	body-centered cubic, page 17
BVP	Boundary Value Problem, page 41
CDD	Continuum Dislocation Dynamics, page 13
CRSS	Critical Resolved Shear Stress, page 99
DDD	Discrete Dislocation Dynamics, page 13
DIC	Digital Image Correlation, page 91
EBS	Electron BackScatter Diffraction, page 104
fcc	face-centered cubic, page 17
FE	Finite Element, page 41
FEM	Finite Element Method, page 41
FV	Finite Volume, page 52
GND	Geometrically Necessary Dislocations, page 20
hex	hexagonal, page 17
IP	Integration Point, page 41
ODE	Ordinary Differential Equation, page 49
PDE	Partial Differential Equation, page 35
SSD	Statistically Stored Dislocation, page 19

Indices, sub-, and superscripts

0	initial value, page 25
b	blocked status (of a dislocation), page 26
D	deformed configuration, page 20
e	edge character (of a dislocation), page 26
e	elastic, page 20
P	PEIERLS, page 37
p	plastic, page 20
R	reference configuration, page 20
s	screw character (of a dislocation), page 26
S	solid-solution, page 37
SD	self diffusion, page 39
u	unblocked status (of a dislocation), page 26
ξ, ζ	slip system, page 21

Symbols

A	area, page 19	m^2
a	coefficient indicating the interaction strength between two slip systems, page 36	
a^n	normal of interface n , page 52	
b	length of BURGERS vector, page 19	m

\mathbf{b}	BURGERS vector, page 21	m
c_{at}	atomic concentration (of solid solution particles), page 37	
\mathbb{C}	elasticity tensor, stiffness, page 21	Pa
\hat{d}	maximum stable dipole height, page 27	m
\check{d}	minimum stable dipole height, page 27	m
d_{obst}	size of solid solution particles, page 37	m
D_{SD}	self diffusivity, page 39	$\text{m}^2 \text{s}^{-1}$
E_e	GREEN-LAGRANGE strain, page 21	
F	deformation gradient, page 20	
F_e	elastic deformation gradient, page 20	
f^n	dislocation flux vector at neighbor n , page 52	$\text{m}^{-1} \text{s}^{-1}$
f	dislocation flux density, page 30	$\text{m}^{-1} \text{s}^{-1}$
\mathbf{f}	dislocation flux vector, page 30	$\text{m}^{-1} \text{s}^{-1}$
F_p	plastic deformation gradient, page 20	
\bar{f}^n	mean dislocation flux vector at interface n , page 52	$\text{m}^{-1} \text{s}^{-1}$
g_{Δ}	constitutive function for jumps in the time evolution of the state, page 44	
g	constitutive function for the time evolution of the state, page 43	
ΔH_{SD}	activation enthalpy for self diffusion, page 39	J
h	constitutive function for the plastic velocity gradient, page 43	s^{-1}
k_1	parameter controlling the edge contribution to the dislocation production rate, page 32	
k_2	scaling parameter for the dislocation production rate, page 32	
l	activation length, page 37	m
L_p	plastic velocity gradient, page 21	s^{-1}
\mathbf{m}	direction of dislocation velocity (unit vector), page 26	
\mathbf{n}	slip system normal, page 21	
\mathbf{O}	crystal orientation, page 25	
P	probability, page 37	
Q	activation free energy, page 37	J
\mathbf{R}	(lattice) rotation from initial to current orientation, page 28	
s	jump width, page 37	m
\mathbf{s}	direction of slip, page 21	
\mathbf{S}	PIOLA-KIRCHHOFF stress of second kind, page 21	Pa
t	time, page 38	s
T	temperature, page 37	K
\mathbf{U}	stretch tensor, page 25	
v	dislocation velocity, page 20	m s^{-1}
\mathbf{v}	dislocation velocity vector, page 29	m s^{-1}
V	volume, page 19	m^3
w_k	width of double kinks, page 37	m
α	KRÖNER-NYE tensor, page 21	
β_e	elastic distortion tensor, page 21	
β_p	plastic distortion tensor, page 21	
γ	plastic slip/shear, page 19	
$\dot{\gamma}$	rate of plastic slip, page 19	s^{-1}
η	viscosity, page 38	Pa s
λ	mean free path between obstacles, page 38	m
λ_f	mean spacing between forest dislocations, page 28	m
μ	shear modulus, page 27	Pa
ν	Poisson's ratio, page 27	

ν_a	attempt frequency for thermal activation, page 38	s^{-1}
ρ_b	blocked monopolar dislocation density, page 27	m^{-2}
ρ_{\pm}	dipolar dislocation density, page 27	m^{-2}
ρ_u	unblocked/free monopolar dislocation density, page 27	m^{-2}
ρ	dislocation density, page 25	m^{-2}
ρ_{Δ}	excess dislocation density, page 28	m^{-2}
ρ_f	forest dislocation density, page 28	m^{-2}
σ	CAUCHY stress, page 21	Pa
τ_{cr}	critical resolved shear stress for dislocation slip, page 36	Pa
τ_{eff}	effectively acting resolved shear stress, page 36	Pa
τ_P	PEIERLS stress, page 38	Pa
τ	shear stress projected onto the slip plane, page 21	Pa
τ_S	solid solution strength, page 38	Pa
Φ	evolution rate for dislocation density, page 31	$m^{-2} s^{-1}$
χ	transmissivity of an interface for dislocations, page 31	
Ψ	temporal jump in dislocation density, page 32	m^{-2}
Ω	atomic volume, page 39	m^3
ω	internal state variables, page 43	

Introduction and background

1

Introduction

In the last decades, the numerical prediction of the deformation behavior of materials has become more and more important. On the one hand, there is an ever growing demand for accurate simulation tools due to new fields of application. As example may serve, the simulation of single-crystalline turbine blades that have to withstand extreme conditions in terms of temperature and forces; another example are small-scale components used in medicine or electronics that can exhibit a completely different mechanical response than large-scale bulk material. On the other hand, the technical advance concerning the resources of computer simulation allows to apply models of increasing complexity that are able to represent materials to finer and finer detail both in terms of spatial accuracy as well as regarding the description of the physical material behavior.

In this respect, the simulation of the deformation behavior of metals is particularly challenging due to the large number of space and time scales involved. This led to an exciting diversity of model approaches ranging from an atomistic scale to large components. Of particular interest for this work are those approaches that explicitly model the behavior of dislocations, such as discrete dislocation dynamics (DDD), dislocation-based constitutive models of crystal plasticity, and the more recently emerged theory of continuum dislocation dynamics (CDD) models.

The most straightforward description is done in the discrete dislocation dynamics, which accounts for every dislocation line in a discretized fashion at typically high spatial resolution. In this approach the equation of motion for every dislocation segment is solved numerically by evaluating the superposition of the stress fields generated by all dislocations (and considering any additionally applied boundary conditions). Discrete dislocation dynamics can be simplified to two-dimensional cases (*e.g.* Van der Giessen and Needleman¹), or treat the dislocations in full three-dimensional space (*e.g.* Kubin et al.,² Zbib et al.,³ Schwarz,⁴ Cai et al.,⁵ Weygand et al.,⁶ Motz et al.⁷), or blend both by incorporating kinematic knowledge of the three-dimensional dislocation reactions into two-dimensional calculations (*e.g.* Benzerga et al.⁸). Knowledge of the possible dislocation

¹ E. Van der Giessen and A. Needleman. Discrete dislocation plasticity: a simple planar model. *Modelling Simul. Mater. Sci. Eng.*, 3:689–735, 1995

² L.P. Kubin, G. Canova, M. Condat, B. Devincre, V. Pontikis, and Y. Bréchet. Dislocation microstructures and plastic flow: a 3D simulation. *Solid State Phenomena*, 23–24:455–472, 1992

³ H.M. Zbib, M. Rhee, and J.P. Hirth. On plastic deformation and the dynamics of 3D dislocations. *Int. J. Mech. Sci.*, 40:113–127, 1998

⁴ K.W. Schwarz. Simulations of dislocations on the mesoscopic scale. I. Methods and examples. *J. Appl. Phys.*, 85:108–119, 1999

⁵ W. Cai, V.V. Bulatov, T.G. Pierce, M. Hiratani, M. Rhee, M. Bartelt, and M. Tang. *Solid Mechanics and Its Applications*, volume 115, chapter Massively-parallel dislocation dynamics simulations, page 1. Kluwer Academic, Dordrecht, The Netherlands, 2004

⁶ D. Weygand, L.H. Friedman, E. Van der Giessen, and A. Needleman. Aspects of boundary-value problem solutions with three-dimensional dislocation dynamics. *Modelling Simul. Mater. Sci. Eng.*, 10:437–468, 2002

⁷ C. Motz, D. Weygand, J. Senger, and P. Gumbsch. Initial dislocation structures in 3-D discrete dislocation dynamics and their influence on microscale plasticity. *Acta Mater.*, 57(6):1744–1754, 2009. DOI: 10.1016/j.actamat.2008.12.020

⁸ A.A. Benzerga, Y. Bréchet, A. Needleman, and E. Van der Giessen. Incorporating three-dimensional mechanisms into dislocation dynamics. *Modelling Simul. Mater. Sci. Eng.*, 12:159–196, 2004

reactions and their respective energetics are a necessary ingredient in all above calculations, which can be informed from calculations at lower (atomistic) scale. Such discrete models of plasticity account for the heterogeneity of the micromechanical problem and contain many of the key details of dislocation mechanics, for instance their tendency to cluster and the presence of spatio-temporal correlations. The discrete representation, however, presently requires a massive computational effort on their mutual long-range interaction. Hence, simulations turn very costly with increasing segment count, which limits strains to only a few percent even on high-performance computing hardware for dislocation multiplication rates typical of bulk deformation.

In contrast to DDD, dislocation-based constitutive models of crystal plasticity represent the dislocation content by a field quantity termed dislocation density, which measures the line length of dislocations per volume. In these models, the constitutive response depends on the evolution of the dislocation density, which is formulated in rate equations (*e.g.* Kocks,⁹ Gottstein and Argon,¹⁰ Estrin et al.,¹¹ Roters et al.,¹² Ma and Roters,¹³ Cheong and Busso¹⁴). This statistical approach allows to also address problems concerning large strains or large time scales (*e.g.* creep) in a computationally efficient manner. However, predictions often lack accuracy when the dimensions of the microstructure and/or the deforming volume decreases well into the micrometer range. Then, the plastic response of crystalline materials changes noticeably (see *e.g.* Fleck et al.,¹⁵ Dehm,¹⁶ Stölken and Evans,¹⁷ Uchic et al.¹⁸ for experimental evidence). At this length scale, the motion of dislocations, which is the origin of plastic slip, becomes apparent, since it may on the one hand lead to accumulation of dislocations where the boundary conditions are not uniform; on the other hand, it may lead to starvation in areas where dislocation multiplication does not suffice to compensate the outflow of dislocations, *i.e.*, where there are not enough active dislocation sources. Any local constitutive model naturally has to fail in the prediction of these effects, since the dislocation density may evolve in time, but does not account for any redistribution in space.

For this reason, a new class of simulation approaches has emerged in the recent years that tries to combine the efficiency of the continuum crystal plasticity approaches with the detailed description of dislocation motion in the discrete dislocation dynamics. These so-called continuum dislocation dynamics (CDD) models treat the dislocation content as continuously defined dislocation density that evolves in time but is also transported in space. They differ in the degree of detail for the description of the dislocation content. The possibly closest description to DDD is achieved when the discrete, curved dislocation segments are represented by a higher-order dislocation density tensor that retains information about the line direction and the curvature. With this description introduced by Hochrainer¹⁹ it is possible to rigorously

⁹ U.F. Kocks. Laws for work-hardening and low-temperature creep. *J. Eng. Mater. Tech. (ASME-H)*, 98:76–85, 1976

¹⁰ G. Gottstein and A.S. Argon. Dislocation theory of steady state deformation and its approach in creep and dynamic tests. *Acta Metallurgica*, 35(6): 1261–1271, 1987. ISSN 0001-6160. DOI: 10.1016/0001-6160(87)90007-1

¹¹ Y. Estrin, L.S. Tóth, A. Molinari, and Y. Bréchet. A dislocation based model for all hardening stages in large strain deformation. *Acta Mater.*, 46(15): 5509–5522, 1998. DOI: 10.1016/S1359-6454(98)00196-7

¹² F. Roters, D. Raabe, and G. Gottstein. Work hardening in heterogeneous alloys – a microstructural approach based on three internal state variables. *Acta Materialia*, 48(17):4181–4189, 2000. DOI: 10.1016/S1359-6454(00)00289-5

¹³ A. Ma and F. Roters. A constitutive model for fcc single crystals based on dislocation densities and its application to uniaxial compression of aluminium single crystals. *Acta Mater.*, 52(12):3603–3612, 2004. DOI: 10.1016/j.actamat.2004.04.012

¹⁴ K.-S. Cheong and E.P. Busso. Discrete dislocation density modelling of single phase FCC polycrystal aggregates. *Acta Materialia*, 52(19):5665–5675, 2004. DOI: 10.1016/j.actamat.2004.08.044

¹⁵ N.A. Fleck, G.M. Muller, M.F. Ashby, and J.W. Hutchinson. Strain gradient plasticity: Theory and experiment. *Acta Metall. Mater.*, 42(2):475–487, 1994. DOI: 10.1016/0956-7151(94)90502-9

¹⁶ G. Dehm. Miniaturized single-crystalline fcc metals deformed in tension: New insights in size-dependent plasticity. *Progress in Materials Science*, 54(6):664–688, 2009. ISSN 0079-6425. DOI: 10.1016/j.pmatsci.2009.03.005

¹⁷ J.S. Stölken and A.G. Evans. A microbend test method for measuring the plasticity length scale. *Acta Materialia*, 46(14):5109–5115, 1998. DOI: 10.1016/S1359-6454(98)00153-0

¹⁸ M.D. Uchic, D.M. Dimiduk, J.N. Florando, and W.D. Nix. Sample Dimensions Influence Strength and Crystal Plasticity. *Science*, 305(5686): 986–989, 2004. ISSN 0036-8075. DOI: 10.1126/science.1098993

¹⁹ T. Hochrainer. *Evolving systems of curved dislocations: Mathematical foundations of a statistical theory*. PhD thesis, Universität Karlsruhe (TH), Aachen, 2006

formulate evolution laws for the dislocation density based only on the motion of dislocations. When supplemented by a kinetic law, this formulation captures the kinematics of crystal plasticity to very fine detail (see, for instance, Sandfeld et al.²⁰). Nevertheless, in order to reduce the still substantial computational effort involved, suitable simplifications of this large configuration space are sought. Among the proposed simplifications are the restriction to two excess densities of edge and screw character plus their mean curvature and the total dislocation content,²¹ or four densities of straight edge and screw dislocations of opposite signs,^{22,23} or one excess density and the total dislocation density when restricting the picture to two dimensions,²⁴ or a single, but spatially variable, line direction.²⁵ To date, no definite conclusion has been reached on how to best capture the dislocation dynamics and associated structure evolution in a continuum framework.

The latter works will serve as a starting point for this thesis. A physics-based constitutive model will be developed that includes dislocation transport in a similar fashion to Arsenlis and Parks [2002]. One aim of this work is to improve the understanding of what happens at the transition from the discrete to the continuum description.

There is still little application of the CDD to problems that allow for a direct comparison to experiments and a validation of the obtained effects—perhaps also due to the non-trivial implementation of the constitutive equations in a crystal plasticity framework. Hence, a second goal is the comparison to existing experimental references in order to analyze the impact of such a theory on the simulation of “real” microstructures.

Outline of the thesis

Chapter 2 is devoted to an introduction of the notion of crystal defects and to the definition of basic terms and equations.

Chapter 3 of the thesis starts by introducing the constitutive equations of the model: the parametrization of the dislocation structure in terms of state variables, the evolution equations of these state variables with special focus on the transport equations of the dislocation density, and the kinetics of dislocations.

Chapter 4 presents the implementation of the constitutive model. This concerns the coupling of the constitutive model with a solver for the mechanical boundary value problem and the internal time integration of the stress. More important is the integration of the state variables, since the nonlocal nature of the constitutive model requires additional effort compared to the usually employed rate equations in classical crystal plasticity modeling.

²⁰ S. Sandfeld, T. Hochrainer, P. Gumbsch, and M. Zaiser. Numerical implementation of a 3D continuum theory of dislocation dynamics and application to micro-bending. *Philosophical Magazine*, 90(27-28):3697–3728, 2010. ISSN 1478-6435. DOI: 10.1080/14786430903236073

²¹ S. Sandfeld, T. Hochrainer, M. Zaiser, and P. Gumbsch. Continuum modeling of dislocation plasticity: Theory, numerical implementation, and validation by discrete dislocation simulations. *Journal of Materials Research*, 26(05):623–632, 2011. ISSN 0884-2914. DOI: 10.1557/jmr.2010.92

²² D. Walgraef and E.C. Aifantis. On the formation and stability of dislocation patterns—I: One-dimensional considerations. *International Journal of Engineering Science*, 23(12):1351–1358, 1985. DOI: 10.1016/0020-7225(85)90113-2

²³ A. Arsenlis and D.M. Parks. Modeling the evolution of crystallographic dislocation density in crystal plasticity. *J. Mech. Phys. Solids*, 50(9):1979–2009, 2002. DOI: 10.1016/S0022-5096(01)00134-X

²⁴ S. Yefimov. *Discrete dislocation and nonlocal crystal plasticity modelling*. PhD thesis, Rijksuniversiteit Groningen, 2004

²⁵ R. Sedláček, J. Kratochvíl, and E. Werner. The importance of being curved: bowing dislocations in a continuum description. *Philosophical Magazine*, 83(31):3735–3752, 2003. ISSN 1478-6435. DOI: 10.1080/14786430310001600213

Chapter 5 analyses the most essential part of the constitutive model, namely the dislocation flux. For a two-dimensional cross-section of a single expanding dislocation loop, two important properties are evaluated: the conservation of dislocation density in the course of dislocation transport; and the stress field that a dislocation exerts in an elastic medium.

Chapter 6 focuses on the comparison of discrete dislocation dynamics results with the present continuum formulation of dislocation dynamics. Three main questions are addressed:

1. How well do discrete and continuum dislocation dynamics simulations match?
2. Does one observe any size effect?
3. What is the role of correlation in a DDD system and how can one account for this in a continuum theory?

Chapter 7 presents the simulation of an existing experiment:²⁶ a simple shear test of an Aluminum bicrystal separated by a small-angle tilt grain boundary. Comparison of simulation and experiment is made for three different models, namely a simple phenomenological model, a local variant of the presented physics-based model that does not account for dislocation fluxes, and the full nonlocal model. A detailed analysis of the simulation results explains the success of the physics-based model to match experiment and the failure of the phenomenological model. The minor influence of the dislocation flux in the nonlocal model variant is discussed and contrasted to earlier simulation approaches to the same experiment by Ma.²⁷

Chapter 8 presents the application of the model to an existing indentation experiment in single-crystalline Nickel.²⁸ This specific experiment is chosen, since its special planar geometry and the resulting limitation of active slip systems allows to derive the geometrically necessary dislocation (GND) density under the indenter from experimentally measured lattice rotations. The simulated rotation patterns and the evolution of the GND density under the indenter is shown to match the experimental observations. A detailed analysis of the involved plastic slips and lattice rotations explains the distribution of the GND density and the formation of an antisymmetry boundary under the indenter. Comparison to a local model variant without dislocation fluxes shows the importance of the dislocation flux in this example having an effect on the evolution of the microstructure, as well as on the mechanical behavior.

Chapter 9 summarizes the major results of the thesis, gives a critical assessment, and discusses continuations of and extension to the presented model.

²⁶ J.C. Kuo. *Mikrostrukturmechanik von Bikristallen mit Kippkornengrenzen*. PhD thesis, RWTH Aachen, 2004

²⁷ A. Ma. *Modeling the constitutive behavior of polycrystalline metals based on dislocation mechanisms*. PhD thesis, RWTH Aachen, 2006

²⁸ J.W. Kysar, Y. Saito, M.S. Oztog, D. Lee, and W.T. Huh. Experimental lower bounds on geometrically necessary dislocation density. *International Journal of Plasticity*, 26(8): 1097–1123, 2010. ISSN 0749-6419. DOI: 10.1016/j.ijplas.2010.03.009

2

Background

2.1 The ideal crystal

The atomic structure of metals is characterized by an undirected force between the atoms. As a result, the atoms in metals tend to arrange in very regular, closed packed structures, which are reminiscent of a stacking of layers of hard spheres. In a highly pure grown metal, this also macroscopically leads to a regular shape, which is typical for pure crystalline matter.

The crystalline structure can be described by an idealized mathematical concept: the crystal lattice. It envisages the atoms as points on a regular grid with defined distances and angles. Most of the metallic crystals form one of the following three lattice types: face-centered cubic (fcc), body-centered cubic (bcc), and hexagonal (hex). The face-centered cubic lattice can be described by a cubic cell with an atom sitting in each of the eight corners and in the center of each of the six faces (see fig. 2.1). This smallest repeating unit of the lattice structure is termed unit cell. In an ideal crystal with all atoms having the same size, the fcc structure corresponds to the closest three-dimensional packing of spheres that is possible. The body-centered lattice can also be described by a cubic unit cell with one atom in each corner, but, in contrast to the fcc lattice, with one further atom in the center of the cell. This results in a slightly less dense packing than for the fcc case. The third important crystal lattice structure, the hexagonal lattice, can be described by layers of a hexagonal grid. The unit cell consists of two triangular prisms. If three of the unit cells are attached to each other, one obtains the often used representation of a hexagonal prism. The hexagonal lattice resembles the fcc lattice, since it can also describe a closed packed lattice called hexagonally closed packed (hcp), if all atoms are of same size. Then, the two lattice types only differ in the stacking order of the closed packed planes.

Directions and planes in the crystal lattice are usually described by MILLER indices. For directions, they denote the coordinates given in a system defined by the edges of the unit cell with the length 1 corresponding to the respective length of the unit cell edges. The coordinates are always given as smallest possible integers, *i.e.*, a direction $(0, 1/2, 1/3)$ in the cubic lattice corresponds to MILLER

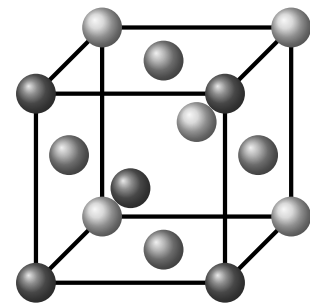


Figure 2.1: Unit cell of the face-centered cubic lattice structure.

indices $[032]$. While a specific direction is given in square brackets $[hkl]$, symmetrically equivalent directions are denoted by sharp brackets $\langle hkl \rangle$. Lattice planes are denoted by normal brackets (uvw) for specific planes and curly brackets for symmetrically equivalent planes $\{uvw\}$. For the lattice planes the indices describe the reciprocal of the intersection point coordinates of the plane with the unit cell axes. A similar notation is possible for the hexagonal lattice type.

2.2 Defects in real crystals

Real crystalline metals do not preserve the perfect lattice structure. In contrast, they contain an abundance of defects. Compared to other types of bondings between atoms, *e.g.*, the ionic bonding, metallic bonds are relatively weak. This facilitates the creation and motion of defects in the material—and in the end the deformation of metals. The different types of defects in metals can be classified according to their dimensionality:

- 0-dimensional: vacancies, interstitial and substitutional atoms
- 1-dimensional: dislocations
- 2-dimensional: grain- and phase boundaries, stacking faults

Three-dimensional defects can usually be characterized by their two-dimensional interfaces. Especially dislocations play an important role for the deformability of a metal as will be seen later and are of particular interest for this work.

The concept of the dislocation The concept of the dislocation was introduced in the early twentieth century by Volterra,¹ however, without making the connection to crystalline matter. He explored the properties of a line singularity in a continuous elastic body. This line singularity can be produced when a cylindrical body is cut, the two newly exposed surfaces are laterally translated with respect to each other, and then again joint. The boundary of the cut constitutes a line singularity, which Volterra [1907] called dislocation.

Inside a crystal, a dislocation describes the border of an area between two regions that are laterally shifted with respect to each other (see fig. 2.2). For the fcc lattice, the displacement usually takes place on the closed packed lattice plane $\{111\}$ along the closed packed direction $\langle 110 \rangle$ on this plane. The actual displacement step is denoted **BURGERS vector** \mathbf{b} . For a dislocation in an fcc crystal lattice it amounts to $\mathbf{b} = \frac{1}{2}\langle 110 \rangle$. Since an area inside a volume always has a closed border, also a dislocation does not simply end inside a crystal. However, the area may reach the surface of the material (as indicated in fig. 2.2) and the distorted lattice can locally relax there. The tangent vector along the dislocation line is termed dislocation line direction \mathbf{l} . According to the orientation of the line direction, different dislocation types are distinguished. If the line

¹ V. Volterra. Sur l'équilibre des corps élastiques multiplement connexes. *Ann. Sci. Ecole Norm. Super.*, 24:401–517, 1907

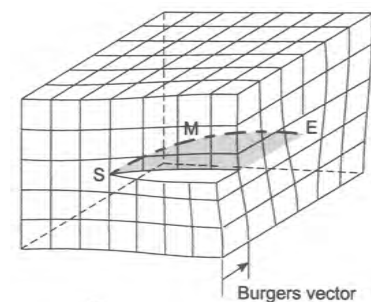
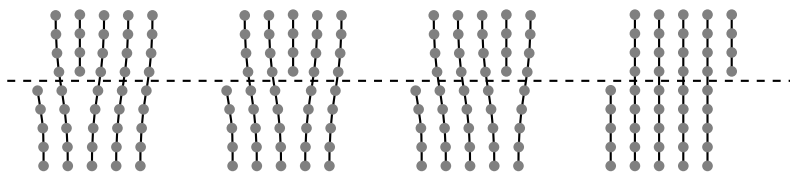


Figure 2.2: Schematic of a part of a dislocation with edge (E), screw (S), and mixed (M) character. Image is taken from Hull and Bacon [2001].

direction is perpendicular to the BURGERS vector, one speaks of edge dislocations; if both are parallel, the dislocation has screw type. However, due to the often irregular shape of a dislocation, a mix of both types is present in most part of the dislocation. A segment of a dislocation can now be completely described by three quantities: the BURGERS vector \mathbf{b} , the line direction \mathbf{l} , and the lattice/slip plane on which the dislocation resides.

Dislocations as source of plastic deformation Independently of each other, Orowan,² Taylor,³ and Polanyi⁴ discovered that the concept of a dislocation can explain the high deformability of metals. Until then, it had been unclear, why the stress that is needed to permanently deform a metal was much lower than expected. A permanent deformation of a crystal—also called plastic deformation—occurs when atomic planes in the crystal lattice slide over each other (see fig. 2.3). In a perfect crystal this can only be accomplished by simultaneous motion of all atoms in the lattice plane. However, Frenkel⁵ showed that the stress needed for this mechanism to occur is much higher than the experimentally observed stresses. The presence of dislocations in the material, however, facilitates the permanent deformation of crystals at much lower stresses. Under a positive applied shear stress a dislocation loop expands (and shrinks if the applied shear stress is negative). The expanding dislocation line leads to a propagation of the lattice discontinuity through the crystal (see fig. 2.4). Since this rearrangement of the atoms happens only locally, the stress that is needed to drive this motion is much lower than a simultaneous motion of all atoms in the lattice plane. Macroscopically, the expansion of dislocation loops results in a shear deformation of the solid and, if the dislocation reaches the surface, in visible steps on the surface.



The rate at which the the crystal is sheared directly relates to the evolution rate of the slipped area A per volume V :

$$\dot{\gamma} = \frac{b\dot{A}}{V} \quad (2.1)$$

Dislocation measures Since the amount of dislocations in a crystal heavily influences the deformation behavior of the material, it is important to quantify the dislocation content. A scalar measure of the dislocation content is the dislocation density ρ , which is defined as the total length of dislocation lines per unit volume. A subset of the total dislocation content are the so-called statistically stored dislocations (SSD), which comprise all dislocations that can be

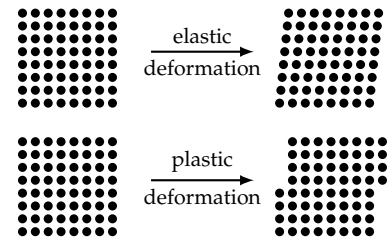


Figure 2.3: Elastic and plastic deformation of a crystal.

² E. Orowan. Zur Kristallplastizität I.–III. *Z. Phys.*, 89:605–659, 1934

³ G. Taylor. The Mechanism of Plastic Deformation of Crystals. Part I. Theoretical. *Proceedings of the Royal Society of London. Series A, Containing Papers of a Mathematical and Physical Character (1905-1934)*, 145(855):362–387, 1934. DOI: 10.1098/rspa.1934.0106

⁴ M. Polanyi. Über eine Art Gitterstörung, die einen Kristall plastisch machen könnte. *Z. Phys.*, 89:660–664, 1934

⁵ J. Frenkel. Zur Theorie der Elastizitätsgrenze und der Festigkeit kristallinischer Körper. *Zeitschrift für Physik*, 37:572–609, 1926

Figure 2.4: Schematic sequence showing an edge dislocation moving through a crystal. The dashed line indicates the slip plane.

combined with other dislocations such that the vector sum of the line directions equals zero. Those dislocations that are left after the summation form a signed quantity called geometrically necessary dislocation density (GND density). The term is reminiscent of the connection to a geometric shape change of the material that can only be explained by the presence of GNDs.⁶

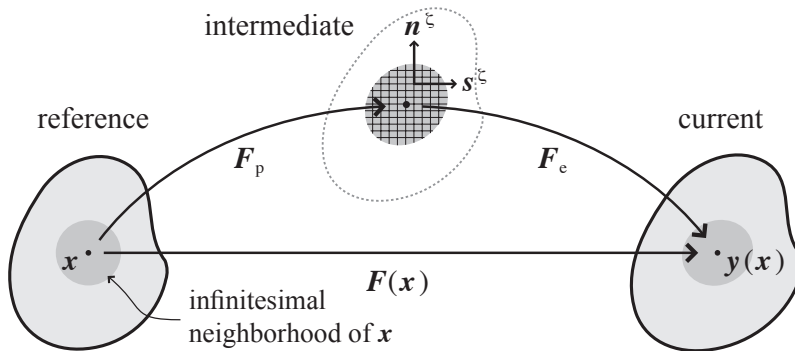
One has to keep in mind that both the statistically stored and the geometrically necessary dislocation density depend on the length scale on which they are defined, *i.e.*, the size of the averaging volume (see fig. 2.5).

With the dislocation density at hand, the rate of plastic slip can be defined via the average dislocation velocity v .⁷

$$\dot{\gamma} = \rho v b \quad (2.2)$$

2.3 Continuum mechanical framework of deformation

The description of the kinematics follows the established continuum mechanical framework of finite strain, recalled, for instance, by Roters et al.⁸ Consider an infinite number of particles, also termed material points, aggregated into a deformable body (or continuum). This body shall occupy the regions \mathbb{B}_0 and \mathbb{B} in three-dimensional Euclidean space \mathbb{R}^3 at two different times t_0 and t . \mathbb{B}_0 denotes the undeformed (or “reference”, subscript “R”) configuration and \mathbb{B} the deformed (or “current”, subscript “D”) configuration. The motion from the undeformed to the deformed configuration follows a mapping $\mathbf{y}(\mathbf{x}) : \mathbf{x} \in \mathbb{B}_0 \mapsto \mathbf{y} \in \mathbb{B}$. The local deformation in an infinitesimal neighborhood $\delta\mathbf{x}$ of material point \mathbf{x} can be linearly approximated by the deformation gradient $\mathbf{F} = \partial\mathbf{y}/\partial\mathbf{x}$, which, in the general case, varies with material point position.



The multiplicative decomposition of the deformation gradient

$$\mathbf{F} = \mathbf{F}_e \mathbf{F}_p \quad (2.3)$$

introduces a stress-free intermediate (or “lattice”) configuration (see fig. 2.6) by conceptually splitting the deformation into a purely

⁶ M.F. Ashby. The deformation of plastically non-homogeneous materials. *Philosophical Magazine*, 21(170):399–424, 1970. DOI: 10.1080/14786437008238426

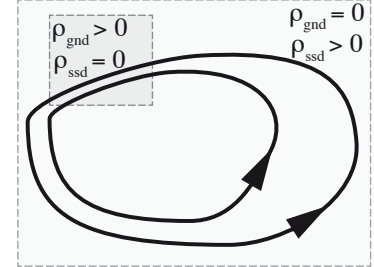


Figure 2.5: Two dislocation loops with same line orientation sense. Depending on the probed volume, either only geometrically necessary dislocation density ρ_{gnd} or only statistically stored dislocation density ρ_{ssd} is measured.

⁷ E. Orowan. Problems of plastic gliding. *Proc. Phys. Soc.*, 52(1):8–22, 1940. DOI: 10.1088/0959-5309/52/1/303

⁸ F. Roters, P. Eisenlohr, L. Hantcherli, D.D. Tjahjanto, T.R. Bieler, and D. Raabe. Overview of constitutive laws, kinematics, homogenization, and multiscale methods in crystal plasticity finite element modeling: theory, experiments, applications. *Acta Materialia*, 58:1152–1211, 2010. DOI: 10.1016/j.actamat.2009.10.058

Figure 2.6: Multiplicative decomposition of the total deformation gradient \mathbf{F} into two parts. The plastic deformation gradient \mathbf{F}_p relates the reference and intermediate configurations. Next, the transformation from the intermediate to the current configuration is characterized by the elastic deformation gradient \mathbf{F}_e . The crystal lattice remains undistorted in the intermediate configuration since dislocation glide rearranges the lattice in a translation-invariant fashion. The slip plane normal \mathbf{n}^ζ and slip direction \mathbf{s}^ζ are exemplarily shown for one slip system ζ .

inelastic (or plastic) part, F_p , and a remaining “elastic” part, F_e , which accounts for (linear) elastic distortions of the crystal lattice and additionally rigid rotation of the entire body.^{9,10,11} Based on the right CAUCHY–GREEN deformation tensor, an elastic strain measure is given by the GREEN–LAGRANGE strain tensor:

$$E_e = \frac{1}{2} \left(F_e^T F_e - I \right). \quad (2.4)$$

The second PIOLA–KIRCHHOFF stress S , as its work-conjugate stress measure in the intermediate configuration, is related to this elastic strain tensor through

$$S = \det F_e F_e^{-1} \sigma F_e^{-T} = \mathbb{C} : E \quad (2.5)$$

with \mathbb{C} being the fourth-order elasticity tensor and σ the CAUCHY stress derived by mapping the second PIOLA–KIRCHHOFF stress from the intermediate into the current configuration.

Plastic deformation is driven by S and in the present case assumed to be mediated exclusively by dislocation glide on slip systems defined by two unit vectors \mathbf{n} and \mathbf{s} as the slip plane normal and slip direction with the latter being parallel to the respective BURGERS vector \mathbf{b} of length b . The shear rates $\dot{\gamma}^\xi$ resulting from corresponding changes in slipped area on systems $\xi = 1, \dots, N$ contribute additively to the plastic velocity gradient¹²

$$L_p = \sum_{\xi} \dot{\gamma}^\xi (\tau^\xi) \mathbf{s}^\xi \otimes \mathbf{n}^\xi, \quad (2.6)$$

which in turn results in an evolution of the plastic deformation gradient at the rate

$$\dot{F}_p = L_p F_p. \quad (2.7)$$

The driving force for dislocation motion is provided by the resolved shear stress

$$\tau^\xi = S : \left(\mathbf{s}^\xi \otimes \mathbf{n}^\xi \right), \quad (2.8)$$

which is the second PIOLA–KIRCHHOFF stress S projected onto the slip system.

2.4 Connection between kinematics and dislocation content

Already in the 1950s Kröner¹³ and Nye¹⁴ pointed out a fundamental link between the kinematics of deformation and the dislocation content associated with it. Their findings are based on a linear theory of strains, hence the multiplicative decomposition of the deformation gradients (see eq. (2.3)) turns into an additive decomposition of so-called distortions.¹⁵

$$\beta = \beta_e + \beta_p \quad (2.9)$$

⁹ B.A. Bilby, L.R.T. Gardner, and A.N. Stroh. Continuous distributions of dislocations and the theory of plasticity. In *Proc. 9th Int. Congr. Appl. Mech.*, volume 8, pages 35–44, Bruxelles, 1957. Université de Bruxelles

¹⁰ E. Kröner. Allgemeine Kontinuumstheorie der Versetzungen und Eigenspannungen. *Arch. Ration. Mech. An.*, 4:273–334, 1960

¹¹ E.H. Lee and D.T. Liu. Finite-Strain Elastic–Plastic Theory with Application to Plane-Wave Analysis. *J. Appl. Phys.*, 38(1):19–27, 1967. DOI: 10.1063/1.1708953; and E.H. Lee. Elastic-plastic deformation at finite strains. *J. Appl. Mech. ASME*, 36(1):1–6, 1969

¹² J.R. Rice. Inelastic constitutive relations for solids: an internal variable theory and its application to metal plasticity. *J. Mech. Phys. Solids*, 19: 433–455, 1971

¹³ E. Kröner. *Kontinuumstheorie der Versetzungen und Eigenspannungen*, volume 5 of *Ergebnisse der angewandten Mathematik*. Springer, Berlin, 1958

¹⁴ J.F. Nye. Some geometrical relations in dislocated crystals. *Acta Metall.*, 1 (2):153–162, 1953. DOI: 10.1016/0001-6160(53)90054-6

¹⁵ The nonlinear version of the theory is much more complicated, but qualitatively gives the same result.

Kröner [1958] introduced a tensor $\boldsymbol{\alpha}$ that is associated with the net BURGERS content \mathbf{b}_C of a BURGERS circuit C around a surface S in a crystal:

$$\int_S dS \cdot \boldsymbol{\alpha} = \mathbf{b}_C \quad (2.10)$$

Then, he showed that this dislocation tensor $\boldsymbol{\alpha}$ can be directly related to the plastic distortion $\boldsymbol{\beta}_p$ by virtue of the differential curl operation:

$$\boldsymbol{\alpha} = \text{curl } \boldsymbol{\beta}_p \quad (2.11)$$

and—under the assumption that the deformed body remains compact—also to the negative curl of the elastic distortion:

$$\boldsymbol{\alpha} = -\text{curl } \boldsymbol{\beta}_e. \quad (2.12)$$

This implies that given that the total distortion of a crystal is compatible, *i.e.*, the body is not torn apart, the plastic incompatibility directly relates to the net BURGERS content in the material. Nye [1953] came to the same result, however based on somewhat different arguments related to the lattice curvature.

Theory

3

Constitutive laws

3.1 Parametrization of microstructure

The properties of a material are characterized by its microstructure, which has to be parametrized in order to model the material behavior. However, due to the abundance of properties that influence the material behavior, there is no unique way of parametrizing the microstructure. One always has to pick those properties that are decisive for the current considerations. The present constitutive model will be based on two main microstructural properties that describe the state of the material and may evolve during the simulation. The first is the crystal lattice and its orientation in space, which entails a finite number of discrete deformation modes. Secondly, the dislocation structure will be considered in terms of dislocation densities of different kinds. All other microstructural parameters in this model will either be deduced from these two; or they are considered as material constants that do not evolve and rather serve as input parameters of the constitutive model.

3.1.1 Crystal orientation

The crystal orientation is a rotation that transfers the sample coordinate system into the crystal or lattice coordinate system. Hence, the orientation is by concept included in the elastic deformation gradient, which is a mapping from the lattice to the current configuration:

$$\mathbf{F}_e = \mathbf{O}^T \mathbf{U}, \quad (3.1)$$

where \mathbf{U} is the elastic stretch tensor. In case of an undeformed reference state, this stretch is initially equal to identity. Then, the initial crystal orientation \mathbf{O}_0 corresponds to

$$\mathbf{O}_0 = \mathbf{F}_{e0}^T. \quad (3.2)$$

3.1.2 Dislocation structure

The complex dislocation structure has to be simplified and is approximated by different densities ρ^ξ per slip system $\xi = 1, \dots, N$

ξ	slip plane	slip direction
1		$[0\bar{1}\bar{1}]$
2	(111)	$[\bar{1}01]$
3		$[1\bar{1}0]$
4		$[0\bar{1}\bar{1}]$
5	$(\bar{1}\bar{1}1)$	$[101]$
6		$[\bar{1}\bar{1}0]$
7		$[0\bar{1}\bar{1}]$
8	$(1\bar{1}\bar{1})$	$[\bar{1}01]$
9		$[110]$
10		$[011]$
11	$(\bar{1}1\bar{1})$	$[101]$
12		$[\bar{1}\bar{1}0]$

Table 3.1: Naming convention used for fcc slip systems

(table 3.1 denoting the fcc slip systems as an example). A distinction between the different densities on a specific slip system can be made via:

- the dislocation character c : edge (subscript “e”) or screw (subscript “s”),
- the dislocation polarity: monopolar density of positive or negative sign (subscript + or -), or unsigned dipolar density (subscript \pm),
- and the dislocation status: free (subscript “u” for unblocked) or blocked (subscript “b”).

As an example, Q_{e-u}^3 denotes the density of unblocked negative edge dislocations on slip system 3.

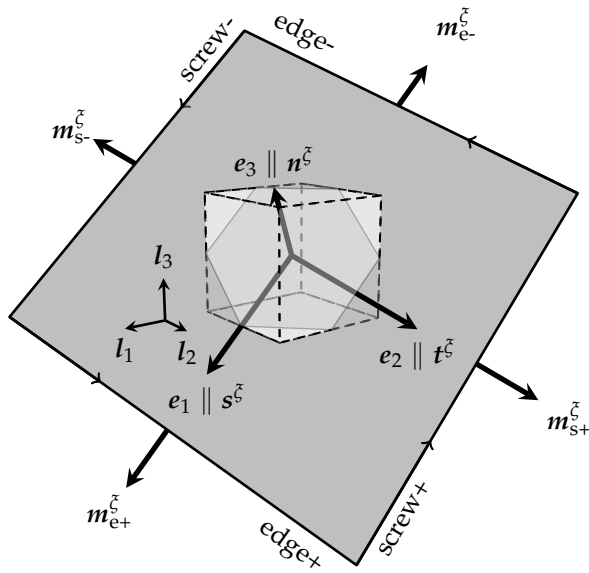


Figure 3.1: Schematic dislocation loop (dark shade) on its slip plane with normal n^ξ , slip direction s^ξ , and positive line direction of positive edge dislocations t^ξ defining (thick) slip system triad e_1, e_2, e_3 . Arrows along the loop periphery indicate positive line direction giving rise to the convention for signed dislocation characters as shown. The small (dashed) interior cube illustrates the crystal unit cell orientation with the lattice basis l_1, l_2, l_3 . A displacement step by b^ξ occurs when passing from below to above the shaded slip plane, *i.e.*, along its normal n^ξ .

Monopolar dislocation density A positive or negative sign reflects the monopolar nature of a single dislocation's stress field. Figure 3.1 illustrates the convention adopted in this work for the sign of edge and screw dislocations on a slip plane. The signed character of these dislocations entails a directionality of their motion under given resolved shear stress. According to fig. 3.1, for a positive shear increment, *i.e.*, increase in the slipped area by loop expansion, these directions of motion m follow as:

$$m_{e+}^\xi = s^\xi \quad (3.3a)$$

$$m_{e-}^\xi = -s^\xi \quad (3.3b)$$

$$m_{s+}^\xi = t^\xi \quad (3.3c)$$

$$m_{s-}^\xi = -t^\xi \quad (3.3d)$$

t^ξ being a unit vector in positive line direction of a positive edge dislocation:

$$t^\xi = n^\xi \times s^\xi. \quad (3.4)$$

Accordingly, the plastic shear rate can be split into four parts for the four types $p \in \{e+, e-, s+, s-\}$ of monopolar dislocation populations.

$$\dot{\gamma}^\zeta = \sum_p \dot{\gamma}_p^\zeta = \sum_p \rho_p^\zeta v_p^\zeta b \quad (3.5)$$

Furthermore, a distinction into free and blocked status is made for the monopolar densities depending on their ability to move in the direction dictated by the resolved shear stress (blocked, for instance, by a grain boundary).

$$\rho_p^\zeta = \rho_{pu}^\zeta + |\rho_{pb}^\zeta| \quad (3.6)$$

The blocked density is a signed quantity, since immobility always applies to one direction of motion only¹. This direction can be determined by multiplying the direction of motion as specified in eq. (3.3) by the sign of the blocked density. Thus, the density is able to move (again) provided the sign of the resolved shear stress is opposite to the sign of the respective blocked density.

Dipole dislocation density The presence of stable dipoles enables dislocation annihilation and is explicitly accounted for in the present parameterization. Stable dipoles contain two monopolar dislocations of the same character but opposite sign, hence two dipole densities, $\rho_{e\pm}^\zeta$ and $\rho_{s\pm}^\zeta$, per slip system are tracked and sum up to the overall dipole density on slip system ζ .

$$\rho_\pm^\zeta = \rho_{e\pm}^\zeta + \rho_{s\pm}^\zeta \quad (3.7)$$

These densities quantify the length per volume contributed by both constituents, thus dislocations changing between monopolar and dipolar state do not alter the sum of both densities.

A dipole will be stable against dissociation under the resolved shear stress τ if the mutual elastic interaction between the two constituents is strong enough, *i.e.*, if the distance between the glide planes of the two dislocations does not exceed

$$\hat{d}_e = \frac{\mu b}{8\pi(1-\nu)} \frac{1}{|\tau|} \quad (3.8a)$$

$$\hat{d}_s = \frac{\mu b}{4\pi} \frac{1}{|\tau|} \quad (3.8b)$$

with μ the shear modulus and ν Poisson's ratio (see appendix A.3). On the other hand, there exists a minimum glide plane separation, \check{d}_c , below which the dipole spontaneously disintegrates by either producing point defects (edge dipoles) or immediate cross-slip (screw dipoles).²

The constituents in such a dipole are linked, which means that motion of this pair is not changing the overall slipped area, and no further shear is contributed by it.

¹ Note, that the usage of the term "immobility" differs from the usually implied notion of dislocation locks.

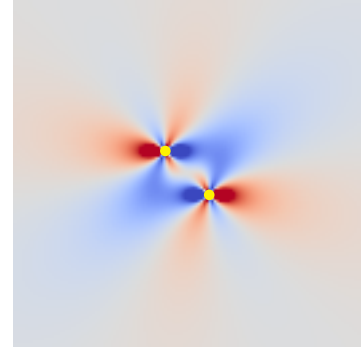


Figure 3.2: Stress field of an edge dipole. The positions of the dislocations are marked by yellow dots.

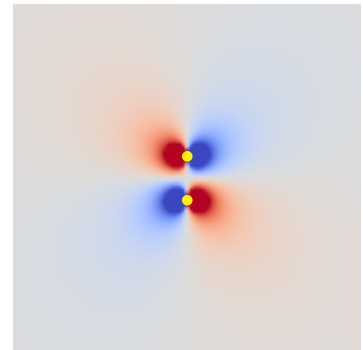


Figure 3.3: Stress field of a screw dipole. The positions of the dislocations are marked by yellow dots.

² U. Essmann and H. Mughrabi. Annihilation of dislocations during tensile and cyclic deformation and limits of dislocation densities. *Philosophical Magazine A*, 40(6):731–756, 1979. DOI: 10.1080/01418617908234871

Total and excess density The polar nature of densities allows to discriminate between the total dislocation densities

$$\varrho^{\zeta} = \varrho_e^{\zeta} + \varrho_s^{\zeta} \quad (3.9a)$$

$$\varrho_e^{\zeta} = \overbrace{\varrho_{e+}^{\zeta} + \varrho_{e-}^{\zeta} + \varrho_{e\pm}^{\zeta}} \quad (3.9b)$$

$$\varrho_s^{\zeta} = \overbrace{\varrho_{s+}^{\zeta} + \varrho_{s-}^{\zeta} + \varrho_{s\pm}^{\zeta}} \quad (3.9c)$$

and the (either positive or negative) excess densities of edge and screw character

$$\varrho_{\Delta e}^{\zeta} = \varrho_{e+}^{\zeta} - \varrho_{e-}^{\zeta} \quad (3.9d)$$

$$\varrho_{\Delta s}^{\zeta} = \varrho_{s+}^{\zeta} - \varrho_{s-}^{\zeta} \quad (3.9e)$$

Forest dislocation density Following Ma and Roters,³ the density on any particular system ζ can be projected with respect to system $\bar{\zeta}$ into a corresponding forest density. By summation of the contribution of each slip system ζ the overall forest density on system $\bar{\zeta}$ results as:

$$\varrho_f^{\bar{\zeta}} = \varrho_e^{\zeta} \left| \mathbf{n}^{\bar{\zeta}} \cdot \mathbf{t}^{\zeta} \right| + \varrho_s^{\zeta} \left| \mathbf{n}^{\bar{\zeta}} \cdot \mathbf{s}^{\zeta} \right| \quad (3.10)$$

The mean spacing between forest dislocations piercing through slip system $\bar{\zeta}$ can be derived from the forest dislocation density:

$$\lambda_f^{\bar{\zeta}} = \frac{1}{\sqrt{\varrho_f^{\bar{\zeta}}}} \quad (3.11)$$

3.2 Microstructure evolution

3.2.1 Crystal rotation

In the course of deformation the orientation of the crystal lattice changes. The rotation that translates the initial crystal orientation \mathbf{O}_0 into the current crystal orientation \mathbf{O} is called crystal rotation \mathbf{R} :

$$\mathbf{O} = \mathbf{R}\mathbf{O}_0 \quad (3.12)$$

and stems from either local elastic lattice distortion or global rigid body rotation. The current crystal orientation rotates the current sample coordinate system into the lattice coordinate system. Hence, it can be obtained by splitting the elastic deformation gradient into a rotation part and the stretch \mathbf{U} by means of a polar decomposition (see eq. (3.1)):

$$\mathbf{F}_e = \mathbf{O}^T \mathbf{U} = (\mathbf{R}\mathbf{O}_0)^T \mathbf{U} \quad (3.13)$$

We make use of the eigendecomposition of the symmetric tensor $\mathbf{F}_e^T \mathbf{F}_e$ (with λ_i as the eigenvalues and \mathbf{v}_i as the eigenvectors)

$$\mathbf{F}_e^T \mathbf{F}_e \mathbf{v}_i = \lambda_i \mathbf{v}_i \quad (3.14)$$

³ A. Ma and F. Roters. A constitutive model for fcc single crystals based on dislocation densities and its application to uniaxial compression of aluminium single crystals. *Acta Mater.*, 52(12):3603–3612, 2004. DOI: 10.1016/j.actamat.2004.04.012

to get the (symmetric) stretch tensor \mathbf{U} .

$$\mathbf{U} = \sum_{i=1}^3 \sqrt{\lambda_i} \mathbf{v}_i \otimes \mathbf{v}_i \quad (3.15)$$

Then, one can solve eq. (3.13) for the rotation tensor \mathbf{R} by making use of the inverse of the stretch tensor.

$$\mathbf{R} = \mathbf{U}^{-1} \mathbf{F}_e^T \mathbf{O}_0^T \quad (3.16)$$

3.2.2 Dislocation transport inside a single crystal

The equations for the dislocation transport will be derived from basic equations of dislocation theory, which are, however, based on continuous fields. Since internal boundaries, such as grain or phase boundaries constitute discontinuities in the plastic strain fields, we will assume a single crystalline material for the moment. Then, we can drop the distinction between blocked and unblocked dislocations as introduced in section 3.1.2, since the notion of blocked dislocations is only needed at discontinuities of the plastic strain field. At a later stage, special care will be taken of these discontinuities (see sections 3.2.3 and 4.3.1).

The state of dislocation in a crystal lattice can be constructed from superposition of the contributions of all dislocation segments present in a given volume (including the case of multiple slip) as $\int \mathbf{l} \otimes \mathbf{b} \, d\varrho$, where \mathbf{l} denotes a unit vector along the dislocation line direction. This state of dislocation corresponds to the so-called KRÖNER-NYE tensor $\boldsymbol{\alpha}$,^{4,5} which in turn is equivalent to the negative curl (incompatibility) of the plastic distortion $\boldsymbol{\beta}_p$. The contribution per individual slip system to this state reads

$$\sum_p \varrho_p^{\xi} \mathbf{l}_p^{\xi} \otimes \mathbf{b} = \boldsymbol{\alpha}^{\xi} = -\text{curl } \boldsymbol{\beta}_p^{\xi}. \quad (3.17)$$

Since segments of opposite line direction cancel out in above sum, only the excess density contributes to incompatibility.⁶

$$\sum_c \varrho_{\Delta c} \mathbf{l}_{c+} \otimes \mathbf{b} = \boldsymbol{\alpha} = -\text{curl}(\gamma \mathbf{n} \otimes \mathbf{s}) \quad (3.18)$$

To arrive at the rate of change of dislocation content, eq. (3.18) is differentiated with respect to time t .

$$\partial_t (\varrho_{\Delta e} \mathbf{l}_{e+} + \varrho_{\Delta s} \mathbf{l}_{s+}) \otimes \mathbf{b} = -\text{curl}(\dot{\gamma}/b \mathbf{n}) \otimes \mathbf{b} \quad (3.19)$$

Without loss of generality we choose our coordinate system as shown in fig. 3.1 to transform eq. (3.19) into

$$\partial_t \begin{pmatrix} \varrho_{\Delta s} \\ -\varrho_{\Delta e} \\ 0 \end{pmatrix} = -\text{curl} \begin{pmatrix} 0 \\ 0 \\ \dot{\gamma}/b \end{pmatrix} = \begin{pmatrix} -\text{grad}_t \dot{\gamma}/b \\ \text{grad}_s \dot{\gamma}/b \\ 0 \end{pmatrix}, \quad (3.20)$$

which reflects the increase of (positive) excess density resulting from a (negative) gradient in the slip rate along the (positive)

⁴J.F. Nye. Some geometrical relations in dislocated crystals. *Acta Metall.*, 1 (2):153–162, 1953. DOI: 10.1016/0001-6160(53)90054-6

⁵E. Kröner. *Kontinuumstheorie der Versetzungen und Eigenspannungen*, volume 5 of *Ergebnisse der angewandten Mathematik*. Springer, Berlin, 1958

⁶In the following the superscript ξ for the slip system will be dropped.

direction of dislocation motion:

$$\partial_t \varrho_{\Delta s} = - \text{grad}_t (\varrho_{e+} v_{e+} + \varrho_{e-} v_{e-} + \varrho_{s+} v_{s+} + \varrho_{s-} v_{s-}) \quad (3.21a)$$

$$\partial_t \varrho_{\Delta e} = - \text{grad}_s (\varrho_{e+} v_{e+} + \varrho_{e-} v_{e-} + \varrho_{s+} v_{s+} + \varrho_{s-} v_{s-}), \quad (3.21b)$$

where eq. (3.5) was substituted for the shear rate.

To uncouple the equation system of all four dislocation types we note that the dislocation densities of same character but opposite sign evolve independent of each other:

$$\partial_t \varrho_{e+} + \text{grad}_s (\varrho_{e+} v_e) = - \kappa_{es} \text{grad}_s (\varrho_s v_s) \quad (3.22a)$$

$$\partial_t \varrho_{e-} - \text{grad}_s (\varrho_{e-} v_e) = (1 - \kappa_{es}) \text{grad}_s (\varrho_s v_s) \quad (3.22b)$$

and

$$\partial_t \varrho_{s+} + \text{grad}_t (\varrho_{s+} v_s) = - \kappa_{se} \text{grad}_t (\varrho_e v_e) \quad (3.22c)$$

$$\partial_t \varrho_{s-} - \text{grad}_t (\varrho_{s-} v_s) = (1 - \kappa_{se}) \text{grad}_t (\varrho_e v_e), \quad (3.22d)$$

with κ_{es} and κ_{se} denoting arbitrary fractions of one. The right-hand side terms in eqs. (3.22a) to (3.22d) reflect the fact that a gradient in slip caused by one character of dislocations results in changes in the other character (here: formation or annihilation of kinks). In the present treatment, such effects are considered to be of second order, which is tantamount to the assumption of straight dislocations that are not interconnected. Dropping these terms transforms above evolution equations for the dislocation densities into pure transport equations.

$$\partial_t \varrho_{e+} + \text{grad}_s (\varrho_{e+} v_e) = 0 \quad (3.23a)$$

$$\partial_t \varrho_{e-} - \text{grad}_s (\varrho_{e-} v_e) = 0 \quad (3.23b)$$

and

$$\partial_t \varrho_{s+} + \text{grad}_t (\varrho_{s+} v_s) = 0 \quad (3.23c)$$

$$\partial_t \varrho_{s-} - \text{grad}_t (\varrho_{s-} v_s) = 0 \quad (3.23d)$$

In the following we denote the product of the unblocked dislocation density and velocity of type p on slip system ζ as dislocation flux $f_p^\zeta = \varrho_{pu}^\zeta v_p^\zeta$ with its scalar magnitude $f_p^\zeta = \varrho_{pu}^\zeta |v_p^\zeta|$. For the regular case inside a single crystal we can then summarise eqs. (3.23a) to (3.23d) as

$$\partial_t \varrho_{pu}^\zeta + \text{div} f_p^\zeta = 0. \quad (3.24)$$

3.2.3 Dislocation transport at discontinuities

The dislocation transport can be altered at internal or external surfaces, such as grain or phase boundaries as well as free surfaces. These interfaces constitute a discontinuity in the dislocation flux. Hence, the derivative needed for the transport eq. (3.24) is not defined at this point. However, reformulating eq. (3.24) in terms of finite volumes, one is able to give physically meaningful expressions around the discontinuities. The exact treatment is explained in detail in section 4.3.1. Here, we will focus on the physical motivation and the basic concepts.

Free surfaces As no dislocations can enter the material from beyond the free surface, the entering flux density⁷ is always zero.⁸ On the other hand, the leaving flux remains unaltered, if there is no additional obstacle at the surface, as, *e.g.*, an oxide layer. Such an oxide layer changes the character of the interface from an external free surface to an internal phase boundary.

Grain/phase boundaries Both grain and phase boundaries form discontinuities in the crystal lattice and as such act as an obstacle against dislocation motion. This gives rise to various reactions, such as dislocation absorption, transmission, reflection, and nucleation (for details on the reactions of dislocations with grain boundaries see *e.g.* Livingston and Chalmers,⁹ Darby et al.,¹⁰ Shen et al.,¹¹ and Lee et al.¹²). Here, we represent these interactions as an effective property of the interface that changes the transmissivity for dislocations. A reduced transmissivity of the interface impedes the flux of dislocations, so that only part of the dislocations crosses the boundary. Technically, this is realized by a reduction of the dislocation flux across the interface by a factor $0 \leq \chi < 1$ called “transmissivity”. Any remainder of the dislocation flux gets stuck in front of the boundary and is left there as blocked dislocation density. Hence, an interface with reduced transmissivity behaves as a source for blocked dislocation density in front of it, and as a sink for (unblocked) density behind it.

This rather simplistic approach has the advantage of a flexible and straight-forward implementation. In contrast to other approaches (see *e.g.* Arsenlis et al.,¹³ Bayley et al.,¹⁴ Puri et al.¹⁵), it does not require any additional boundary conditions for the dislocation density or flux. This enables to easily control the properties of the interface, and even to specify different properties for different density types, slip systems, stress states, *etc.*

3.2.4 Dislocation generation

New dislocations are generated in the course of plastic deformation and lead to an increase of the dislocation density. Here, we regard multiple cross slip of screw dislocations as the most relevant mechanism for dislocation multiplication. Screw dislocations change their habit slip plane, *i.e.* cross glide, if they encounter an obstacle that impedes further loop expansion on the primary slip plane, and if at the same time dislocation glide on a collinear system is possible. When relating the obstacles that promote cross slip to the dislocation forest, the multiplication rate due to multiple cross slip of screws linearly depends on the inverse of the forest dislocation spacing. With $|\dot{\gamma}_s|/b$ as the rate of slipped area per volume due to glide of screw dislocations one obtains the relationship

$$\text{mult } \Phi_{pu} \propto \frac{|\dot{\gamma}_s|}{b \lambda_f}. \quad (3.25)$$

⁷ An entering flux of dislocations is identified by a positive component of its flux vector in direction of the inward pointing surface normal.

⁸ Although dislocations can be generated at a free surface, this contribution would rather be incorporated into the evolution equations as additional source term at the surface, and not as a dislocation flux.

⁹ J.D. Livingston and B. Chalmers. Multiple slip in bicrystal deformation. *Acta Metallurgica*, 5(6):322–327, 1957. ISSN 0001-6160. DOI: 10.1016/0001-6160(57)90044-5

¹⁰ T.P. Darby, R. Schindler, and R.W. Balluffi. On the interaction of lattice dislocations with grain boundaries. *Philosophical Magazine A*, 37(2):245–256, 1978. ISSN 0141-8610. DOI: 10.1080/01418617808235438

¹¹ Z. Shen, R.H. Wagoner, and W.A.T. Clark. Dislocation and grain boundary interactions in metals. *Acta Metallurgica*, 36(12):3231–3242, 1988. DOI: 10.1016/0001-6160(88)90058-2

¹² T.C. Lee, I.M. Robertson, and H.K. Birnbaum. TEM in situ deformation study of the interaction of lattice dislocations with grain boundaries in metals. *Philosophical Magazine A*, 62(1):131–153, 1990. ISSN 0141-8610. DOI: 10.1080/01418619008244340

¹³ A. Arsenlis, D.M. Parks, R. Becker, and V.V. Bulatov. On the evolution of crystallographic dislocation density in non-homogeneously deforming crystals. *J. Mech. Phys. Solids*, 52:1213–1246, 2004. DOI: 10.1016/j.jmps.2003.12.007

¹⁴ C.J. Bayley, W.A.M. Brekelmans, and M.G.D. Geers. A comparison of dislocation induced back stress formulations in strain gradient crystal plasticity. *Int. J. Solids Struct.*, 43(24):7268–7286, 2006. DOI: 10.1016/j.ijsolstr.2006.05.011

¹⁵ S. Puri, A. Acharya, and A.D. Rollett. Controlling Plastic Flow across Grain Boundaries in a Continuum Model. *Metallurgical and Materials Transactions A*, 42(3):669–675, 2011. ISSN 1073-5623. DOI: 10.1007/s11661-010-0257-8

In the following, any source or sink term for the dislocation density will be denoted by Φ and goes to the right-hand side of eq. (3.24). Dislocations of edge type contribute to a minor extent to the production of new dislocation line length by loop expansion or—for very high concentration of vacancies—by Bardeen-Herring sources.¹⁶

For the total dislocation generation we define an effective rate

$$\text{mult } \Phi_{pu} = \frac{|k_1 \dot{\gamma}_e + \dot{\gamma}_s|}{k_2 b \lambda_f} = \frac{(k_1 f_e + f_s) \sqrt{\rho_f}}{k_2}, \quad (3.26)$$

with $0 < k_1 \leq 1$ as parameter that controls the edge contribution to dislocation generation, and with a second (phenomenological) scaling parameter $10 \lesssim k_2 \lesssim 100$.

3.2.5 Change of dislocation state

A change in the dislocation state comprises all reactions that lead to a relabeling of the dislocation. Here, this refers to either a change in the polarity (monopolar/dipolar) or in the status (blocked/unblocked). The equations for the rate of formation and dissociation of dipolar dislocations are based on the work of Eisenlohr.¹⁷

Remobilization of monopolar dislocations Blocked dislocations can be remobilized if the resolved shear stress changes sign. Then, the direction of dislocation motion is reversed and the formerly immobile dislocations move in opposite direction. If we assume that all blocked dislocations instantaneously remobilize, the entire blocked dislocation density is converted to unblocked dislocation density.

$$\text{remob } \Psi_{pb} = - |q_{pb}| \quad (3.27)$$

$$\text{remob } \Psi_{pu} = |q_{pb}| \quad (3.28)$$

Since the rate associated with this instantaneous change in dislocation state is infinite, the above reaction is not formulated as rate equation, but as a step function Ψ .

Dipole formation To arrive at the transformation rate of monopolar to dipolar dislocations, it is helpful to consider the volume fraction

$$d \ln V = \frac{dV}{V} = 2 \hat{d}_c \frac{dA}{V} = 2 \hat{d}_c \frac{|d\gamma_c|}{b} = 2 \hat{d}_c f_c dt \quad (3.29)$$

that is sampled by gliding monopolar dislocations of character c per shear increment $d\gamma_c$. A dipole is formed if a gliding dislocation hits a dislocation of opposite sign within this volume fraction.

Unblocked monopolar density can transform by either actively moving towards an opposite (unblocked or blocked) dislocation, or by passively having an opposite unblocked dislocation move

¹⁶ D. Hull and D.J. Bacon. *Introduction to Dislocations*. Butterworth-Heinemann, 2001

¹⁷ P. Eisenlohr. *On the role of dislocation dipoles in unidirectional deformation of crystals*. PhD thesis, Universität Erlangen-Nürnberg, 2004

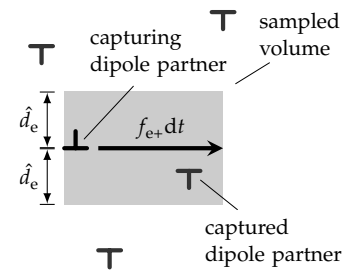


Figure 3.4: Example for the formation of dislocation dipoles: A flux of positive edge dislocations f_{e+} captures negative edge dislocation density q_{e-} that is in a strip of height $2\hat{d}_e$.

towards itself. These two configurations lead to a combined transformation loss rate of monopolar dislocations of

$$\text{mono} \rightarrow \text{di} \Phi_{c+u} = -2 \hat{d}_c (\varrho_{c-} f_{c+} + \varrho_{c+u} f_{c-}) \quad (3.30a)$$

$$\text{mono} \rightarrow \text{di} \Phi_{c-u} = -2 \hat{d}_c (\varrho_{c+} f_{c-} + \varrho_{c-u} f_{c+}). \quad (3.30b)$$

Blocked monopolar dislocations only serve as a passive partner in the creation of a dipole, therefore their rate is given by

$$\text{mono} \rightarrow \text{di} \Phi_{c+b} = -2 \hat{d}_c \varrho_{c+b} f_{c-} \quad (3.30c)$$

$$\text{mono} \rightarrow \text{di} \Phi_{c-b} = -2 \hat{d}_c \varrho_{c-b} f_{c+}. \quad (3.30d)$$

Since the total dislocation content is not changed by such transformations, the corresponding rate of change (production) of dipolar density follows as the negative sum of eqs. (3.30a) to (3.30d).

$$\text{mono} \rightarrow \text{di} \Phi_{c\pm} = 4 \hat{d}_c (\varrho_{c+} f_{c-} + \varrho_{c-} f_{c+}) \quad (3.30e)$$

Dipole dissociation Dipoles that were formed by gliding monopolar dislocations can dissociate again when the stress level increases. If we assume that the distribution of dipole heights is uniform within the stability range, then a reduction in the upper stability limit due to increasing resolved shear stress will lead to a symmetric dissociation of dipoles back into monopolar unblocked dislocation density.

If $\Delta \hat{d}_c < 0$:

$$\text{di} \rightarrow \text{mono} \Psi_{c\pm} = \varrho_{c\pm} \frac{\Delta \hat{d}_c}{\hat{d}_c - \check{d}_c} \quad (3.31a)$$

$$\text{di} \rightarrow \text{mono} \Psi_{c+u} = \text{di} \rightarrow \text{mono} \Psi_{c-u} = -\frac{1}{2} \text{di} \rightarrow \text{mono} \Psi_{c\pm} \quad (3.31b)$$

Elseif $\Delta \hat{d}_c \geq 0$:

$$\text{di} \rightarrow \text{mono} \Psi_{c+u} = \text{di} \rightarrow \text{mono} \Psi_{c-u} = \text{di} \rightarrow \text{mono} \Psi_{c\pm} = 0 \quad (3.31c)$$

3.2.6 Dislocation annihilation

A decrease in the overall dislocation density is considered a result of athermal as well as thermally activated annihilation of dipoles.

Thermal annihilation of edge dipoles Edge dislocation dipoles can annihilate by out-of-plane climb motion of their two constituents. This process requires production and diffusion of vacancies and is thermally activated.¹⁸ Consequently, annihilation by climb of edges is significant only at high temperatures or very high degrees of deformation¹⁹. Here, we introduce climb by means of the edge dipolar dislocation density and the average separation of the dipoles $\hat{d}_e - \check{d}_e$. If half the average dipole separation is overcome by

¹⁸ J.P. Hirth and J. Lothe. *Theory of dislocations*. John Wiley & Sons, New York, 1982

¹⁹ In case of very high deformation ($\varepsilon > 1$) large amounts of vacancies are produced. As shown by Zehetbauer and Seumer [1993], these deformation induced high concentrations of vacancies facilitate climb motion of edge dislocations, hence can lead to significant annihilation of edge dipoles by climb already at room temperature.

climb, all dipoles would be annihilated, so the annihilation rate by climb of edges reads

$$\text{climb } \Phi_{e\pm} = -\rho_{e\pm} \frac{2v_{\text{climb}}}{(\hat{d}_e - \check{d}_e)/2} = -4\rho_{e\pm} \frac{v_{\text{climb}}}{\hat{d}_e - \check{d}_e}. \quad (3.32)$$

Athermal annihilation by instantaneous recombination Annihilation of edge dipoles by climb does not readily occur at low temperatures. Yet, very close edge dipoles can nonetheless annihilate spontaneously and form either vacancy or interstitial point defects.²⁰ This athermal annihilation process is modeled by assuming that out of all edge dipoles newly formed by glide (eq. (3.30e)) those annihilate instantaneously that have a glide plane separation below \check{d}_e . In addition to these close encounters among monopolar dislocations, moving monopolar dislocations may knock out a compatible constituent from an already existing dipole. Combining both reactions leads to

$$\begin{aligned} \text{athAnn } \Phi_{e\pm} = & -4\check{d}_e (\rho_{e+} f_{e-} + \rho_{e-} f_{e+}) \\ & - 2\check{d}_e \rho_{e\pm} (f_{e-} + f_{e+}). \end{aligned} \quad (3.33)$$

Screw dipoles can annihilate by cross-slip, *i.e.*, by a change from the habit slip plane onto a collinear slip plane.²¹ While this process can be thermally activated, hence depend on temperature and mechanical assist, we assume it to take place instantaneously for all screw dipoles having a glide plane separation below \check{d}_s . Consequently, the cross-slip process of screw dipoles is treated in the same manner as the athermal disintegration of edge dipoles.

$$\begin{aligned} \text{cross-slip } \Phi_{s\pm} = & -4\check{d}_s (\rho_{s+} f_{s-} + \rho_{s-} f_{s+}) \\ & - 2\check{d}_s \rho_{s\pm} (f_{s-} + f_{s+}) \end{aligned} \quad (3.34)$$

However, the minimum glide plane separation that controls these mechanisms can differ significantly.²²

While the annihilation of edge dipoles produces vacancies or interstitials, screw dipoles that annihilate by cross-slip deposit two edge jogs on the collinear slip system (see fig. 3.5). Each annihilated screw dipole creates two edge jogs of the length equal to the mean dipole height

$$l_{\text{jog}} = \frac{1}{2} (\hat{d}_s + \check{d}_s). \quad (3.35)$$

The number of screw dipoles that annihilate by cross-slip can be determined from the cross-slip annihilation rate $\text{cross-slip } \Phi_{s\pm}$, if one assumes that the average segment length of a screw dipole is proportional to the forest spacing. Then, screw dipoles of the primary slip system ζ that annihilate by cross-slip generate an average density of both positive and negative unblocked edges on

²⁰ J. Friedel. *Dislocations*. Addison-Wesley, Reading, Massachusetts, 1964; and U. Essmann and H. Mughrabi. Annihilation of dislocations during tensile and cyclic deformation and limits of dislocation densities. *Philosophical Magazine A*, 40(6):731–756, 1979. DOI: 10.1080/01418617908234871

²¹ U. Essmann and H. Mughrabi. Annihilation of dislocations during tensile and cyclic deformation and limits of dislocation densities. *Philosophical Magazine A*, 40(6):731–756, 1979. DOI: 10.1080/01418617908234871

²² For copper Essmann and Mughrabi [1979] report a value of about $6b$ for the minimum stable dipole height of edges and of about $200b - 2000b$ for screw dipoles.

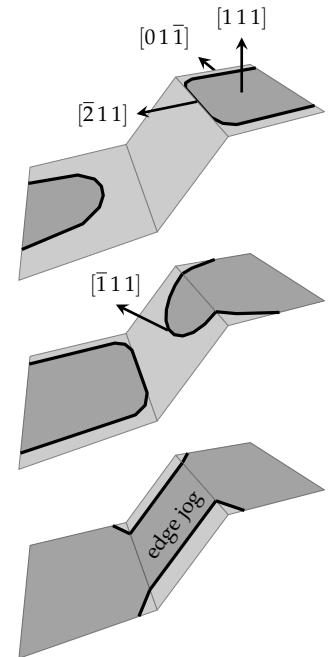


Figure 3.5: Cross-slip of a screw dipole leaving an edge jog on the collinear slip system behind.

the according collinear slip system ζ :

$$\begin{aligned} \text{jog} \Phi_{e+u}^{\zeta} &= \text{jog} \Phi_{e-u}^{\zeta} = -k_3 \frac{\text{cross-slip} \Phi_{s\pm}^{\zeta}}{2} \frac{l_{\text{jog}}}{\lambda_f} \\ &= -\frac{k_3}{4} \sqrt{\rho_f^{\zeta}} \left(\hat{d}_s^{\zeta} + \hat{d}_s^{\zeta} \right) \text{cross-slip} \Phi_{s\pm}^{\zeta}, \end{aligned} \quad (3.36)$$

where k_3 is a scalar factor between 0 and 1.

Summary of state evolution equations The equations derived above form a system of partial differential equations (PDE) with the local rate equations for generation, annihilation and state change as sink or source terms. Hence, for each slip system ζ we have the following set of PDEs:

$$\partial_t \rho_{e+u}^{\zeta} + \text{div} f_{e+}^{\zeta} = \text{interf} \Phi_{e+u}^{\zeta} + \text{mult} \Phi_{e+u}^{\zeta} + \text{mono} \rightarrow \text{di} \Phi_{e+u}^{\zeta} + \text{jog} \Phi_{e+u}^{\zeta} + \partial_t \left(\text{di} \rightarrow \text{mono} \Psi_{e+u}^{\zeta} + \text{remob} \Psi_{e+u}^{\zeta} \right) \quad (3.37a)$$

$$\partial_t \rho_{e-u}^{\zeta} + \text{div} f_{e-}^{\zeta} = \text{interf} \Phi_{e-u}^{\zeta} + \text{mult} \Phi_{e-u}^{\zeta} + \text{mono} \rightarrow \text{di} \Phi_{e-u}^{\zeta} + \text{jog} \Phi_{e-u}^{\zeta} + \partial_t \left(\text{di} \rightarrow \text{mono} \Psi_{e-u}^{\zeta} + \text{remob} \Psi_{e-u}^{\zeta} \right) \quad (3.37b)$$

$$\partial_t \rho_{s+u}^{\zeta} + \text{div} f_{s+}^{\zeta} = \text{interf} \Phi_{s+u}^{\zeta} + \text{mult} \Phi_{s+u}^{\zeta} + \text{mono} \rightarrow \text{di} \Phi_{s+u}^{\zeta} + \partial_t \left(\text{di} \rightarrow \text{mono} \Psi_{s+u}^{\zeta} + \text{remob} \Psi_{s+u}^{\zeta} \right) \quad (3.37c)$$

$$\partial_t \rho_{s-u}^{\zeta} + \text{div} f_{s-}^{\zeta} = \text{interf} \Phi_{s-u}^{\zeta} + \text{mult} \Phi_{s-u}^{\zeta} + \text{mono} \rightarrow \text{di} \Phi_{s-u}^{\zeta} + \partial_t \left(\text{di} \rightarrow \text{mono} \Psi_{s-u}^{\zeta} + \text{remob} \Psi_{s-u}^{\zeta} \right) \quad (3.37d)$$

$$\partial_t \rho_{e+b}^{\zeta} = \text{interf} \Phi_{e+b}^{\zeta} + \text{mono} \rightarrow \text{di} \Phi_{e+b}^{\zeta} + \partial_t \left(\text{remob} \Psi_{e+b}^{\zeta} \right) \quad (3.37e)$$

$$\partial_t \rho_{e-b}^{\zeta} = \text{interf} \Phi_{e-b}^{\zeta} + \text{mono} \rightarrow \text{di} \Phi_{e-b}^{\zeta} + \partial_t \left(\text{remob} \Psi_{e-b}^{\zeta} \right) \quad (3.37f)$$

$$\partial_t \rho_{s+b}^{\zeta} = \text{interf} \Phi_{s+b}^{\zeta} + \text{mono} \rightarrow \text{di} \Phi_{s+b}^{\zeta} + \partial_t \left(\text{remob} \Psi_{s+b}^{\zeta} \right) \quad (3.37g)$$

$$\partial_t \rho_{s-b}^{\zeta} = \text{interf} \Phi_{s-b}^{\zeta} + \text{mono} \rightarrow \text{di} \Phi_{s-b}^{\zeta} + \partial_t \left(\text{remob} \Psi_{s-b}^{\zeta} \right) \quad (3.37h)$$

$$\partial_t \rho_{e\pm}^{\zeta} = \text{mono} \rightarrow \text{di} \Phi_{e\pm}^{\zeta} + \text{climb} \Phi_{e\pm}^{\zeta} + \text{athAnn} \Phi_{e\pm}^{\zeta} + \partial_t \left(\text{di} \rightarrow \text{mono} \Psi_{e\pm}^{\zeta} \right) \quad (3.37i)$$

$$\partial_t \rho_{s\pm}^{\zeta} = \text{mono} \rightarrow \text{di} \Phi_{s\pm}^{\zeta} + \text{cross-slip} \Phi_{s\pm}^{\zeta} + \partial_t \left(\text{di} \rightarrow \text{mono} \Psi_{s\pm}^{\zeta} \right) \quad (3.37j)$$

Here, the rates $\text{interf} \Phi$ account for the blocking of dislocations at interfaces, which will be deduced in section 4.3.1. The derivatives of the jump functions Ψ will in practice not be calculated (as they are infinite by definition), but only the jump itself will be used for the state integration (also see section 4.3.2).

3.3 Dislocation kinetics

The kinetics of dislocations are controlled by the two types of dislocation motion, namely dislocation glide and dislocation climb. The former is associated with the in-plane motion of monopolar dislocations and leads to plastic deformation. The latter describes the out-of-plane motion of dipolar dislocations and leads to mutual annihilation of the two constituents of a dislocation dipole, hence, gives rise to recovery. The minor contributions to deformation from climb motion is neglected here.

3.3.1 Dislocation glide velocity

The driving force for the in-plane motion of dislocations is the second PIOLA-KIRCHHOFF stress resolved onto the slip system: the resolved shear stress τ as defined in eq. (2.8). The glide motion of dislocations is impeded by various obstacles, out of which some may be overcome by thermal activation, and some by mechanical stress alone (see table 3.2). The mutual interaction of dislocations is considered too strong as to allow for thermal activation. Hence, we describe the effect of dislocation obstacles in terms of a mechanical threshold stress, referred to as critical resolved shear stress τ_{cr} . For an applied resolved stress below this value no dislocation activity occurs. Above this threshold, an effective resolved shear stress τ_{eff} that is reduced by the critical resolved shear stress is acting as driving force for dislocation motion.²³

$$\tau_{eff} = \begin{cases} (|\tau| - \tau_{cr}) \text{sign } \tau & \text{if } |\tau| > \tau_{cr} \\ 0 & \text{if } |\tau| \leq \tau_{cr} \end{cases} \quad (3.38)$$

The flowstress τ_{cr} accounts for the different strength $a^{\xi\zeta}$ of the interacting dislocations on slip systems ξ and ζ .

$$\tau_{cr}^{\xi} = \mu b \sqrt{\sum_{\zeta} a^{\xi\zeta} \rho_{\zeta}}, \quad (3.39)$$

$\xi \backslash \zeta$	1	2	3	4	5	6	7	8	9	10	11	12
1	s	cp	cp	h	l	g	cl	g	g	h	g	l
2	cp	s	cp	l	h	g	g	h	l	g	cl	g
3	cp	cp	s	g	g	cl	g	l	h	l	g	h
4	h	l	g	s	cp	cp	h	g	l	cl	g	g
5	l	h	g	cp	s	cp	g	cl	g	g	h	l
6	g	g	cl	cp	cp	s	l	g	h	g	l	h
7	cl	g	g	h	g	l	s	cp	cp	h	l	g
8	g	h	l	g	cl	g	cp	s	cp	l	h	g
9	g	l	h	l	g	h	cp	cp	s	g	g	cl
10	h	g	l	cl	g	g	h	l	g	s	cp	cp
11	g	cl	g	g	h	l	l	h	g	cp	s	cp
12	l	g	h	g	l	h	g	g	cl	cp	cp	s

In the case of fcc crystals, six distinct reactions with characteristic strength can be identified (see table 3.3 for a correlation between slip systems and interaction types). Values for junction and lock forming are taken from Kubin et al.;²⁴ they are given in table 3.4.²⁵ Yet, in contrast to Kubin et al. [2008] we assume the coefficients for

obstacle	activation
phase boundaries	mechanical
grain boundaries	mechanical
dislocations	mechanical
solid-solution atoms	thermal
PEIERLS barrier	thermal

Table 3.2: Obstacles for dislocation motion that are taken into account in this work.

²³ A. Seeger. The Temperature Dependence of the Critical Shear Stress and of Work-hardening of Metal Crystals. *Philosophical Magazine Series 7*, 45(366):771-773, 1954. DOI: 10.1080/14786440708520489

Table 3.3: Interaction types between slip systems ζ and ξ in an fcc crystal structure; s: self interaction; cp: coplanar interaction; cl: collinear interaction; h: Hirth locks; g: glissile junctions; l: Lomer locks. Slip systems are defined in table 3.1.

²⁴ L. Kubin, B. Devincre, and T. Hoc. Modeling dislocation storage rates and mean free paths in face-centered cubic crystals. *Acta Mater.*, 56(20):6040-6049, 2008. DOI: 10.1016/j.actamat.2008.08.012

²⁵ According to Kubin et al. [2008] the three coefficients for junction forming mechanisms (Hirth, glissile and Lomer) slightly depend on the dislocation density because of line tension effects. This can be captured by a correction term

$$c = \left(0.2 + 0.8 \frac{\log(0.35b\sqrt{\rho_f})}{\log(0.35b\sqrt{\rho_{ref}})} \right)^2$$

with $\rho_{ref} = 1 \cdot 10^{12} \text{ m}^{-2}$.

interaction type	interaction coefficient
self	0
coplanar	0
collinear	0.625
Hirth	0.07
glissile	0.137
Lomer	0.122

Table 3.4: Interaction coefficients for fcc crystals. Values for the collinear interaction, Hirth locks, glissile junctions and Lomer locks are taken from Kubin et al. [2008].

the self and the coplanar interaction to be equal to zero. Instead, self hardening is implied by the sink term for the monopolar density due to formation of dipoles, which decreases the amount of available carrier density for dislocation slip (see eqs. (3.30a) and (3.30b)). A second source for self hardening stems from the deposition of edge jogs on the cross-slip plane due to the annihilation of screw dipoles as described in section 3.2.6. These edge jogs act back on the primary slip system via the strong collinear interaction and contribute to self hardening. While Kubin et al. [2008] included these effects implicitly by a non-zero hardening coefficient for self and coplanar hardening, the present work tries to make direct use of the information about the annihilation of screw dipoles. The rate of screw dipole annihilation entails a production rate of edge jogs on the collinear system as given in eq. (3.36). This production term on the collinear system then leads to significant hardening of the primary slip system, similar to a self hardening effect.

In addition to dislocation obstacles, the present work considers thermally activated obstacles against dislocation motion such as PEIERLS barriers and solid solution atoms. Thermal activation of this effect is treated according to Kocks et al.²⁶ The probability P to overcome an obstacle by thermal activation at temperature T is given by

$$P = \exp\left(-\frac{Q}{k_B T} \left(1 - \left(\frac{|\tau_{\text{eff}}|}{\hat{\tau}}\right)^p\right)^q\right), \quad (3.40)$$

where Q is the activation energy required to overcome the obstacle, $\hat{\tau}$ is the strength of the obstacle, and p and q are parameters describing the shape of the energy profile of the obstacle.²⁷ The activation energy is determined by the work that is done when a shear stress equal to the obstacle strength acts on the slip plane and causes a relative displacement of b over the slipped area A :

$$Q = \hat{\tau} A b = \hat{\tau} l s b, \quad (3.41)$$

where the slipped area A results from a jump of width s along the activation length l of the dislocation. Obstacles of differing strength and geometry can concurrently influence the effective dislocation velocity. *E.g.*, for solid solution particles, the geometry is determined by the atomic concentration of solid solution particles

²⁶ U.F. Kocks, A.S. Argon, and M.F. Ashby. Thermodynamics and Kinetics of Slip. *Progress in Materials Science*, 19: 1–291, 1975

²⁷ The probability for backward jumps, *i.e.* in direction opposed to the mechanical driving force, is considered negligible.

c_{at} and the particle size d_{obst} :

$$l_S = \frac{b}{\sqrt{c_{\text{at}}}}, \quad s_S = d_{\text{obst}}, \quad (3.42)$$

where subscript S stands for solid solution. Equivalently, for the PEIERLS mechanism as thermally activated obstacle one can define

$$l_P = w_k, \quad s_P = b, \quad (3.43)$$

with w_k denoting the double kink width and subscript P for the PEIERLS mechanism. By use of eq. (3.40) we can define the waiting time t in front of an obstacle as the inverse of the product of the attempt frequency ν_a and the success probability P :

$$t_P = \frac{1}{\nu_a} \exp \left(\frac{Q_P}{k_B T} \left(1 - \left(\frac{|\tau_{\text{eff}}|}{\tau_P} \right)^p \right)^q \right) \quad (3.44)$$

$$t_S = \frac{1}{\nu_a} \exp \left(\frac{Q_S}{k_B T} \left(1 - \left(\frac{|\tau_{\text{eff}}|}{\tau_S} \right)^p \right)^q \right), \quad (3.45)$$

where τ_P denotes the PEIERLS stress and τ_S the strength of the solid solution particles. After a successful event the dislocation will on average travel a distance that is equal to the mean space between obstacles λ , *e.g.*, in case of solid solution particles

$$\lambda_S = \frac{b}{\sqrt{c_{\text{at}}}} \quad (3.46)$$

or for a PEIERLS valley

$$\lambda_P = b. \quad (3.47)$$

The travel time for this distance depends on the travel velocity v_T , which is assumed to depend linearly on the applied stress:

$$v_T = \frac{b}{\eta} |\tau_{\text{eff}}|, \quad (3.48)$$

where η is a scalar constant inversely proportional to the mobility of the dislocations.

The effective velocity can then be determined from the waiting time at an obstacle and the travel velocity between the obstacles.

$$v = \frac{\lambda}{t + \frac{\lambda}{v_T}} = \left(\frac{t}{\lambda} + \frac{1}{v_T} \right)^{-1} \quad (3.49)$$

The ratio t/λ is an effective value in case that different obstacles can be thermally activated.

$$\frac{t}{\lambda} = \frac{t_P}{\lambda_P} + \frac{t_S}{\lambda_S} + \dots \quad (3.50)$$

If we consider PEIERLS barriers and solid solution particles to be the dominant obstacles, we obtain the dislocation velocity by

inserting eqs. (3.44), (3.45) and (3.48) into eq. (3.49).

$$v = \left[\frac{1}{\nu_a \lambda_P} \exp \left(\frac{Q_P}{k_B T} \left(1 - \left(\frac{|\tau_{\text{eff}}|}{\tau_P} \right)^p \right)^q \right) + \frac{1}{\nu_a \lambda_S} \exp \left(\frac{Q_S}{k_B T} \left(1 - \left(\frac{|\tau_{\text{eff}}|}{\tau_S} \right)^p \right)^q \right) + \frac{\eta}{b |\tau_{\text{eff}}|} \right]^{-1} \text{sign } \tau \quad (3.51)$$

The sign function at the end of eq. (3.51) ensures that positive resolved shear stress leads to an expansion of the slipped area, while a negative shear stress leads to loop shrinkage.

3.3.2 Dislocation climb velocity

Additionally to expansion and shrinkage of a dislocation loop within the glide plane, the edge components of a dislocation loop are able to move out of the glide plane by dislocation climb. An expression for this climb velocity can be found in *e.g.* Hirth and Lothe:²⁸

$$v_{\text{climb}} = \frac{D_{\text{SD}}}{b} \left[\exp \left(\frac{\Omega \sigma_c}{k_B T} \right) - 1 \right], \quad (3.52)$$

where Ω denotes the atomic volume, σ_c the stress driving the climb process and D_{SD} the self diffusivity of vacancies, which can be calculated from the activation enthalpy for self diffusion ΔH_{SD} as

$$D_{\text{SD}} = D_{\text{SD}}^0 \exp \left(-\frac{\Delta H_{\text{SD}}}{k_B T} \right). \quad (3.53)$$

The stress σ_c that leads to edge climb is the normal stress component parallel to the BURGERS vector that consists of the externally applied stress and the internal stress between the two dipole constituents. The contribution of the external stress is neglected and it is assumed that the mutual elastic interaction between dipole constituents is decisive for their out-of-glide-plane motion.²⁹

$$\sigma_c = \frac{\mu b}{2\pi(1-\nu)} \frac{2}{\hat{d}_e + \check{d}_e} \quad (3.54)$$

Provided that $\Omega \sigma_c \ll k_B T$ one can linearize the exponential term in eq. (3.52). Inserting eq. (3.54) into this linearized equation finally leads to the following expression for the climb velocity:

$$v_{\text{climb}} = \frac{1}{\pi(1-\nu)} \frac{D_{\text{SD}}}{\hat{d}_e + \check{d}_e} \frac{\mu \Omega}{k_B T}. \quad (3.55)$$

²⁸ J.P. Hirth and J. Lothe. *Theory of dislocations*. John Wiley & Sons, New York, 1982

²⁹ P. Eisenlohr. *On the role of dislocation dipoles in unidirectional deformation of crystals*. PhD thesis, Universität Erlangen-Nürnberg, 2004

4

Implementation

4.1 Solution of the mechanical boundary value problem

The simulation of the deformation of crystalline matter poses a mechanical boundary value problem (BVP). This can be solved by different numerical strategies. Here, two techniques will be applied: the (most commonly used) Finite Element Method (FEM) and a spectral method based on fast fourier transforms. Both rely on the formulation of a constitutive relation between stress and strain, *i.e.*, for a given deformation, the constitutive model has to return a corresponding stress (and a stiffness). The FEM or the spectral method, then iteratively ensures balance of linear and angular momentum.

In this work, the commercially available software MSC.MARC2010 was used for the FEM. The employed spectral solver is an integral part of DAMASK,¹ the “Düsseldorf Advanced Material Simulation Kit”, which also contains the constitutive model presented here. Implementation details concerning the spectral solver can be found in Eisenlohr et al. [2013]

¹ DAMASK. Düsseldorf Advanced Material Simulation Kit. URL <http://damask.mpie.de/>

In order to be able to use the important nonlocal dislocation transport of the constitutive model, two specialities in the use of the solvers have to be mentioned.

First, the solution of the dislocation flux relies on a complete knowledge of the neighborhood relations of all integration points (IPs) in the model. In the case of the FEM, this information is reconstructed from the connectivity of the elements that are defined by the FE solver and accessible via an ASCII text file. Although this procedure can be quite time consuming for large number of elements, this has to be done only once during initialization of the simulation. Another speciality of the nonlocal model is that the deformation state always has to be known for the neighborhood of an integration point, since the dislocation transport depends on the plastic slip activity—thus deformation—at the neighboring material points. As a consequence, all integration points have to be solved simultaneously, *i.e.*, the constitutive solution of the integration points cannot (as is usually done in standard FEM) be computed one after another. Instead, for the calculation of the constitutive response always the complete information of the entire

computational domain is required. Since the interface to the FEM only allows to pass the deformation gradient of a single integration point, a special numerical strategy is employed that consists of two stages. In the first stage, the material subroutine collects the requested deformation gradient of all integration points one after another. At the same time an “odd” stress and an extremely high stiffness is returned to the FE solver. This ensures that the solver does 1) not converge for this increment and 2) not change the requested deformation gradients for the next iteration. If the latter is fulfilled, then, in the next iteration, all the requested deformation gradients are already known when the first integration point is called. During this call, the material subroutine can then calculate the constitutive response for all integration points at once. In the subsequent calls of the other integration points, the already calculated results are returned one by one.

4.1.1 Material point grid and associated finite volumes

Having in mind the typically irregular grid of integration points in an FE discretization, finite volumes (cells) are defined that have the shape of arbitrarily distorted eight-node hexahedrons, each attached to one integration point (corresponding to a “material point”).² The cell volume is denoted by V . Each cell has exactly six nearest neighbors n that define its neighborhood. A shared interface with area A^n is situated between neighboring cell volumes and is characterized by its outward pointing unit normal \mathbf{a}^n (see fig. 4.1).

Each cell undergoes a deformation that is defined by the deformation gradient associated with its material point. This has to be taken into account for the unit normals \mathbf{a}^n and the interface area A^n . As these measures are always shared among two neighboring material points (see fig. 4.1), their values in the *deformed configuration* result, to a first-order approximation, from averaging the two deformation gradients, \mathbf{F} and \mathbf{F}^n , valid at the central and neighboring material point.

$$\bar{\mathbf{F}} = (\mathbf{F} + \mathbf{F}^n) / 2 \quad (4.1)$$

Using the average deformation gradient to define a common deformed configuration allows for pushing forward to that and pulling back into the lattice configuration.

$$\mathbf{a}^n = \frac{\mathbf{F}_e^T \bar{\mathbf{F}}^{-T} \mathbf{a}_R^n}{\left\| \mathbf{F}_e^T \bar{\mathbf{F}}^{-T} \mathbf{a}_R^n \right\|} \quad (4.2)$$

$$A^n = A_R^n \det \left(\mathbf{F}_e \bar{\mathbf{F}}^{-1} \right) \left\| \mathbf{F}_e^T \bar{\mathbf{F}}^{-T} \mathbf{a}_R^n \right\| \quad (4.3)$$

Subscripts “R”, “none”, and “D” refer to quantities defined in the reference, lattice, and common deformed configuration, respectively. Note that \mathbf{a}^n remains at unit length due to the normalizing denominator in eq. (4.2).

² In general, the volume center of such a cell does not have to coincide with corresponding integration point. Here, this difference will be neglected.

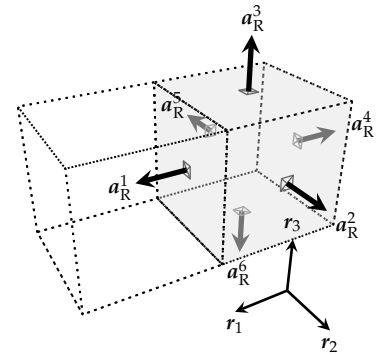


Figure 4.1: Exemplary orthogonal cell with basis triad $\mathbf{r}_1, \mathbf{r}_2, \mathbf{r}_3$ in reference configuration. Interfaces between neighboring material points are characterized by their outward pointing normals \mathbf{a}_R^n and have area A_R^n .

4.2 Coupling of elasticity and plasticity

In order to arrive at a solution for stress equilibrium and strain compatibility the solver of the mechanical boundary value problem needs to know the stress response of the integration points to a given deformation. More precisely, for each time increment Δt the BVP solver requests a stress that results from a change in the deformation gradient from $F(t_0)$ to $F(t_0 + \Delta t = t)$. Depending on the BVP solver the stress measure that is required is either a CAUCHY stress σ (FE solver) or a first PIOLA–KIRCHHOFF stress P (spectral solver). Both measures can, however, be calculated from any other stress measure by simple transformation rules (see appendix A.1). Here, the connection between strain and stress is based on the GREEN–LAGRANGE strain E and its work-conjugate, the second PIOLA–KIRCHHOFF stress S .

$$S = \mathbb{C} : E = \frac{1}{2} \mathbb{C} : (F_e^T F_e - I) \quad (4.4)$$

By applying the multiplicative decomposition of the deformation gradient (eq. (2.3)) one can equally express this in terms of the plastic deformation gradient F_p .

$$S = \frac{1}{2} \mathbb{C} : (F_p^{-T} F^T F F_p^{-1} - I) \quad (4.5)$$

In any case, the partitioning between elastic and plastic part of the deformation gradient determines the stress response. This partitioning has to be calculated for each increment in order to obtain the stress response. While the material initially deforms purely elastic, the proportion of the plastic deformation will increase once the yield point of the material is reached. The rate with which the plastic deformation gradient evolves is determined by the plastic velocity gradient L_p .

$$L_p = \dot{F}_p F_p^{-1} \quad (4.6)$$

$$\dot{F}_p = L_p F_p \quad (4.7)$$

The plastic velocity gradient in turn depends on the second PIOLA–KIRCHHOFF stress acting as a driving force for the plastic deformation, as well as on the underlying microstructure represented by some state variables ω . The exact relationship is part of the constitutive behavior of the material point and is described by the function h .³

$$L_p = h(S, \omega) \quad (4.8)$$

The microstructure at the material point evolves simultaneously with the kinematic quantities. So, additionally, there is a second constitutive equation called g that describes the evolution rate of the state variables.

$$\dot{\omega} = g(S, \omega) \quad (4.9)$$

³ Here, the plastic deformation is assumed to be mediated exclusively by dislocation glide, so the constitutive function h is given by eq. (2.6):

$$h(S, \omega) = \sum_{\xi} \gamma^{\xi} s^{\xi} \otimes n^{\xi} .$$

In some cases it might be necessary to express the change in the microstructure in terms of an instantaneous jump rather than by a rate of change. For this case, a third constitutive equation g_Δ that is not formulated as rate equation can equally be defined.

$$\Delta\omega = g_\Delta(\mathbf{S}, \omega) \quad (4.10)$$

The two differential eqs. (4.7) and (4.9) (plus eq. (4.10) for instantaneous jumps) describe the time evolution of the plastic deformation gradient and the microstructure and are coupled by eqs. (4.5) and (4.8), which in turn give the local material response to the prescribed total deformation in terms of the stress. Under the assumption that the microstructure, *i.e.*, the state variables, evolves slower than the stress, one can decouple eq. (4.9) from the others. Then, the set of equations can be solved in two levels (see fig. 4.2):

1. In an inner level, the stress \mathbf{S} is obtained by solving eqs. (2.3), (4.4), (4.7) and (4.8) at constant state ω .
2. In an outer level, the state ω is obtained by solving eq. (4.9) for a given stress \mathbf{S} .

4.2.1 Inner level of integration: the stress

In order to solve the set of eqs. (2.3), (4.4), (4.7) and (4.8) for the time integration of the stress, eq. (4.7) is expressed in an implicit manner:

$$\frac{\mathbf{F}_p(t) - \mathbf{F}_p(t_0)}{\Delta t} = \mathbf{L}_p(t)\mathbf{F}_p(t), \quad (4.11)$$

where t_0 is the time at the beginning of the increment and t the time at the end of the increment. Then, the plastic and elastic deformation gradient at the end of the time increment are given by

$$\mathbf{F}_p(t) = (\mathbf{I} - \Delta t \mathbf{L}_p(t))^{-1} \mathbf{F}_p(t_0) \quad (4.12)$$

$$\mathbf{F}_e(t) = \mathbf{F}(t)\mathbf{F}_p^{-1}(t_0) (\mathbf{I} - \Delta t \mathbf{L}_p(t)). \quad (4.13)$$

By this linearization procedure, one obtains a system of three nonlinear algebraic equations with three unknowns $\mathbf{S}(t)$, $\mathbf{F}_e(t)$, and $\mathbf{L}_p(t)$:

$$\mathbf{S}(t) = \frac{1}{2} \mathbb{C} : (\mathbf{F}_e^T(t)\mathbf{F}_e(t) - \mathbf{I}) \quad (4.14)$$

$$\mathbf{F}_e(t) = \mathbf{A} (\mathbf{I} - \Delta t \mathbf{L}_p(t)) \quad (4.15)$$

$$\mathbf{L}_p(t) = h(\mathbf{S}(t), \omega(t)), \quad (4.16)$$

where the known quantity $\mathbf{F}(t)\mathbf{F}_p^{-1}(t_0)$ is substituted by \mathbf{A} for brevity.

This system can be solved by a NEWTON-RAPHSON scheme by either minimizing the residuum in \mathbf{S} , \mathbf{F}_e , or \mathbf{L}_p . Choosing the norm of the residuum in \mathbf{S} as an objective function has the advantage that the inverse that is needed for the NEWTON-RAPHSON procedure is

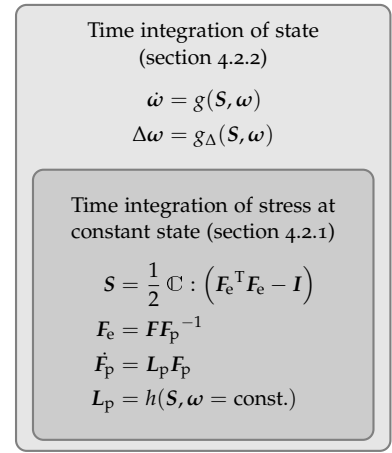


Figure 4.2: Equations used for the time integration of the stress and the microstructural state

Residuum	S	F_e	L_p
Jacobian	6x6	9x9	9x9
Sensitivity	high	high	low
Implementation	Kalidindi et al. [1992]		4.2.1

only 6×6 compared to 9×9 for L_p or F_e , since the stress tensor is symmetric, while L_p and F_e are not. However, it is much harder to guess for S than for L_p , since the latter can change by orders for a small deviation in S (see table 4.1). So in contrast to *e.g.* Kalidindi et al.,⁴ the NEWTON–RAPHSON scheme is chosen to be build around L_p . Hence, the residuum in L_p for the i th iteration is defined as

$$\mathbf{R}^i = \widetilde{\mathbf{L}}_p^i - h(S(F_e(\widetilde{\mathbf{L}}_p^i))) \quad (4.17)$$

and the objective function, which will be minimized, as the FROBENIUS norm of the residuum.

$$\min_{L_p} \|\mathbf{R}\|_2 \quad \text{with} \quad \|\mathbf{R}\|_2 = \sqrt{\mathbf{R} : \mathbf{R}} \quad (4.18)$$

$\widetilde{\mathbf{L}}_p^0 = L_p(t_0)$	
For $i = 0, 1, \dots, n$	
$\mathbf{R}^i = \widetilde{\mathbf{L}}_p^i - h(S(\widetilde{\mathbf{L}}_p^i))$	
Y	$\ \mathbf{R}^i\ _2 < \epsilon_{\text{tol}}$
N	
break	$\ \mathbf{R}^i\ _2 \leq \ \mathbf{R}^{i-1}\ _2$ or $i = 0$
Y	
N	
	$\alpha^i = 1$
	$\alpha^i = \beta \alpha^{i-1}$
	solve $\mathbf{R}^i + \mathbf{R}_{, \widetilde{\mathbf{L}}_p} \bullet \Delta \mathbf{L}_p^i = 0$
	$\widetilde{\mathbf{L}}_p^i = \widetilde{\mathbf{L}}_p^{i-1}$
	$\widetilde{\mathbf{L}}_p^{i+1} = \widetilde{\mathbf{L}}_p^i + \alpha^i \Delta \mathbf{L}_p^i$
$L_p(t) = \widetilde{\mathbf{L}}_p^i$	

The minimization procedure employs a modified NEWTON–RAPHSON scheme with variable step length α (see fig. 4.3). The correction of the i th guess for L_p is based on the derivative of the residuum and is obtained by solving the following linear equation for $\Delta \mathbf{L}_p^i$:

$$\mathbf{R}^i + \mathbf{R}_{, \widetilde{\mathbf{L}}_p} \bullet \Delta \mathbf{L}_p^i = 0. \quad (4.19)$$

The derivative of the residuum depends on the constitutive equation eq. (4.8) (see eq. (4.17)).

$$\mathbf{R}_{, \widetilde{\mathbf{L}}_p} = \mathbb{I} - h_{, S} \bullet S_{, F_e} \bullet F_{e, \widetilde{\mathbf{L}}_p} \quad (4.20)$$

In this equation the derivative $h_{, S}$ is known from the constitutive equation (see appendix A.4). The derivative of the second

Table 4.1: Properties of the NEWTON–RAPHSON scheme depending on the selected residuum

⁴S.R. Kalidindi, C.A. Bronkhorst, and L. Anand. Crystallographic texture evolution in bulk deformation processing of fcc metals. *J. Mech. Phys. Solids*, 40(3):537–569, 1992. DOI: 10.1016/0022-5096(92)80003-9

Figure 4.3: NEWTON–RAPHSON scheme for L_p . The constant β is usually chosen to be equal to 0.5.

PIOLA–KIRCHHOFF stress with respect to the elastic deformation gradient can be derived from eq. (4.14).

$$\begin{aligned}
\mathbf{S}_{,F_e} &= \frac{1}{2} \left(\mathbb{C} : \left(\mathbf{F}_e^T \mathbf{F}_e - \mathbf{I} \right) \right)_{,F_e} \\
&= \frac{1}{2} \mathbb{C} : \left(\mathbf{F}_e^T \mathbf{F}_e \right)_{,F_e} \\
&= \frac{1}{2} \mathbb{C} : \left(\mathbb{I}^R \mathbf{F}_e + \mathbf{F}_e^T \mathbb{I} \right) \\
&= \frac{1}{2} \mathbb{C} : \left(\mathbf{I} \boxtimes \mathbf{F}_e + \mathbf{F}_e^T \otimes \mathbf{I} \right)
\end{aligned} \tag{4.21}$$

Similarly, with eq. (4.15), one finds the derivative of the elastic deformation gradient with respect to the plastic velocity gradient.

$$\begin{aligned}
\mathbf{F}_{e, \widetilde{\mathbf{L}}_p} &= \left(\mathbf{A} \left(\mathbf{I} - \Delta t \widetilde{\mathbf{L}}_p \right) \right)_{, \widetilde{\mathbf{L}}_p} \\
&= -\Delta t \mathbf{A} \mathbb{I} \\
&= -\Delta t \mathbf{A} \otimes \mathbf{I}
\end{aligned} \tag{4.22}$$

Inserting this into eq. (4.20) one obtains the jacobian.

$$\begin{aligned}
\mathbf{R}_{, \widetilde{\mathbf{L}}_p} &= \mathbb{I} + \frac{\Delta t}{2} h_{,s} \bullet \bullet \mathbb{C} : \left(\mathbf{I} \boxtimes \mathbf{F}_e + \mathbf{F}_e^T \otimes \mathbf{I} \right) \bullet \bullet \mathbf{A} \otimes \mathbf{I} \\
&= \mathbb{I} + \frac{\Delta t}{2} h_{,s} \bullet \bullet \mathbb{C} : \left(\mathbf{I} \boxtimes \mathbf{A}^T \mathbf{F}_e + \mathbf{F}_e^T \mathbf{A} \otimes \mathbf{I} \right)
\end{aligned} \tag{4.23}$$

Now, eq. (4.19) can be solved by means of any method for linear equation systems. Here, a standard solver from the “Linear Algebra PACKage”⁵ is employed, which uses an LU decomposition with partial pivoting and row interchanges. The resulting correction $\Delta \mathbf{L}_p$ is used to update the guess for \mathbf{L}_p . The updated guess is only accepted if the residuum is decreased in the next step. Otherwise, subsequent guesses are based on the same (old) jacobian, but with a step that is cutbacked by a factor β (usually chosen equal to 0.5) until the solution has improved. This procedure ensures faster convergence both from the viewpoint of iterations and computational effort, because the costly solution of eq. (4.19) is not needed in every iteration.

⁵ <http://www.netlib.org/lapack>

The NEWTON–RAPHSON scheme is regarded converged when the residuum drops below a given tolerance ϵ . This tolerance can either be specified as relative (ϵ_r) or absolute value (ϵ_a).

$$\epsilon = \max \left\{ \epsilon_r \left\| \mathbf{L}_p \right\|_2 ; \epsilon_r \left\| \widetilde{\mathbf{L}}_p \right\|_2 ; \epsilon_a \right\} \tag{4.24}$$

4.2.2 Outer level of integration: the state

The outer level in the integration procedure sketched by fig. 4.2 consists of the integration of the microstructural state variables ω in time. Different schemes can be used to accomplish this integration. The following schemes are implemented and tested in order to compare their performance and choose the best suited for this task:

1. a fixed-point iteration scheme,
2. an explicit EULER integrator,

3. an adaptive EULER integrator,
4. a fourth-order explicit RUNGE–KUTTA integrator, and
5. a fifth-order adaptive RUNGE–KUTTA integrator.

All of the above listed are based on the constitutive rate equation for the state eq. (4.9).

Fixed-point iteration Kalidindi et al. [1992] originally used a simple fixed-point procedure to integrate the state. This scheme subsequently evaluates the state and the stress until a fixed-point for the state is found. This leads to a final solution with a consistent stress and state.

However, the error of the final solution cannot be controlled. Only the error of the fixed-point is known and used as convergence criterion. How close this fixed-point is to the exact solution is unknown. Kalidindi et al. [1992] use a second criterion to control the length of the step size. However, for a negative curvature of the state (*i.e.*, decreasing evolution rate with increasing state) the error will always be better than first-order independent of the step size. A schematic of the integration procedure is given in fig. 4.4.

Explicit Euler integrator The simplest integrator is the explicit EULER. It consists of a single explicit time step without any control of the error:

$$\omega(t) = \omega(t_0) + \dot{\omega}(t_0)\Delta t + \Delta\omega(t_0) \quad (4.25)$$

The last term in eq. (4.25) describes an instantaneous jump in the state variables that cannot be formulated as rate equation. The stress integration is executed *after* the state update, so that the calculated stress at the end of the increment is always consistent with the state. A schematic of the complete integration procedure is given in fig. 4.5.

Adaptive Euler integrator An enhancement of the explicit EULER integrator is the adaptive EULER integrator, which also performs a single explicit step, but uses a second evaluation of the state integration to estimate the error.

$$\epsilon = \frac{\Delta t}{2} (\dot{\omega}(t) - \dot{\omega}(t_0)) \quad (4.26)$$

This error estimate can then be compared to a given tolerance; in case that the tolerance is not achieved it can trigger a cutback of the time step. Since a cutback of the time step would have no influence on an instantaneous jump in the state, it is natural to not include the state jump in the error estimate. As for the explicit EULER integrator the stress integration is done after the state evolution. A schematic of the integration procedure is given in fig. 4.6.

Fourth-order explicit Runge–Kutta integrator Both the explicit EULER and the adaptive EULER integrator are first-order schemes, hence

$i = 0$
$S_0 = S(t_0)$
$\omega_0 = \omega(t_0) + g(S_0, \omega(t_0))\Delta t$
$i = i + 1$
integrate $S_i = S(\omega_{i-1})$
$\omega_i = \omega(t_0) + g_\Delta(S_i, \omega_{i-1})$
$\omega_i = \omega_i + g(S_i, \omega_i)\Delta t$
Until $ \omega_i _\infty - \omega_{i-1} _\infty < \epsilon_{\text{tol}}$
$\omega(t) = \omega_i ; S(t) = S_i$

Figure 4.4: Fixed point integration scheme for the state ω

$\omega = \omega(t_0) ; S = S(t_0)$
$\omega = \omega + g_\Delta(S, \omega)$
$\omega = \omega + g(S, \omega)\Delta t$
integrate $S(\omega)$
$\omega(t) = \omega ; S(t) = S$

Figure 4.5: Explicit EULER integration scheme for the state ω

$\omega = \omega(t_0) ; S = S(t_0)$
$\omega = \omega + g_\Delta(S, \omega)$
$\epsilon = -\frac{1}{2} g(S, \omega)\Delta t$
$\omega = \omega + g(S, \omega)\Delta t$
integrate $S(\omega)$
$\epsilon = \epsilon + \frac{1}{2} g(S, \omega)\Delta t$
$\epsilon < \epsilon_{\text{tol}}$
Y N
$\omega(t) = \omega ; S(t) = S$ cutback

Figure 4.6: Adaptive EULER integration scheme for the state ω

they produce an accumulated error of the order of Δt . One way to reduce the error is to go to higher order integration schemes. The fourth-order RUNGE–KUTTA integrator provides such a scheme with an accumulated error of the order of Δt^4 . In this scheme, the state at the end of the increment is calculated on the basis of a weighted average of four different slopes, namely

1. g_{RK}^1 at the beginning of the increment based on the state $\omega(t_0)$,
2. g_{RK}^2 in the middle of the increment based on the state $\omega(t_0) + \frac{1}{2}g_{\text{RK}}^1\Delta t$,
3. g_{RK}^3 in the middle of the increment based on the state $\omega(t_0) + \frac{1}{2}g_{\text{RK}}^2\Delta t$, and
4. g_{RK}^4 at the end of the increment based on the state $\omega(t_0) + g_{\text{RK}}^3\Delta t$.

Whenever the state is evaluated at intermediate time steps, also the stress integration has to use only half the time increment and only half the deformation increment for these integration steps. All in all, one needs four evaluations of the state evolution function g and four inner level stress integrations. This entails additional computational costs for each integration step, which, however, often pays off in nonlinear problems, since it allows much bigger time increments than first-order methods as *e.g.* the adaptive EULER method. A schematic of the integration procedure is given in fig. 4.7.

Fifth-order adaptive Runge–Kutta integrator This fifth-order adaptive RUNGE–KUTTA integrator⁶ combines the high-order solution of the fourth-order explicit RUNGE–KUTTA integrator with the possibility of the adaptive EULER integrator to control the error. By an additional evaluation of stress and state this integrator allows to estimate the error. The BUTCHER tableau (see table 4.2) is constructed in such a way that the additional evaluation can also be used for the final solution increasing its order to five. A schematic of the integration procedure is given in fig. 4.8.

0	0				c	A
$\frac{1}{5}$	$\frac{1}{5}$	0				b^T
$\frac{3}{10}$	$\frac{3}{40}$	$\frac{9}{40}$	0			d^T
$\frac{3}{5}$	$\frac{3}{10}$	$-\frac{9}{10}$	$\frac{6}{5}$	0		
1	$-\frac{11}{54}$	$\frac{5}{2}$	$-\frac{70}{27}$	$\frac{35}{27}$	0	
$\frac{7}{8}$	$\frac{1631}{55296}$	$\frac{175}{512}$	$\frac{575}{13824}$	$\frac{44275}{110592}$	$\frac{253}{4096}$	0
	$\frac{37}{378}$	0	$\frac{250}{621}$	$\frac{125}{594}$	0	$\frac{512}{1771}$
	$\frac{2825}{27648}$	0	$\frac{18575}{48384}$	$\frac{13525}{55296}$	$\frac{277}{14336}$	$\frac{1}{4}$

Benchmark of the state integrators With the exception of the fixed-point iteration scheme proposed by Kalidindi et al. [1992], all the integrators that were briefly introduced above are used for the

$\omega = \omega(t_0) ; S = S(t_0) ; g_{\text{RK}} = 0$
$a_1 = \frac{1}{2} ; a_2 = \frac{1}{2} ; a_3 = 1$
$b_1 = \frac{1}{6} ; b_2 = \frac{1}{3} ; b_3 = \frac{1}{3} ; b_4 = \frac{1}{6}$
For $i = 1, \dots, 3$
$\tilde{\Delta t} = a_i \Delta t, \tilde{F}(t) = F(t_0) + a_i \Delta F$
$g_{\text{RK}} = g_{\text{RK}} + b_i g(S, \omega)$
$\omega = \omega(t_0) + g(S, \omega) \tilde{\Delta t}$
$\omega = \omega + g_{\Delta}(S, \omega)$
integrate $S(\omega, F = \tilde{F}, \Delta t = \tilde{\Delta t})$
$g_{\text{RK}} = g_{\text{RK}} + b_4 g(S, \omega)$
$\omega = \omega(t_0) + g_{\text{RK}} \Delta t$
$\omega = \omega + g_{\Delta}(S, \omega)$
integrate $S(\omega)$
$\omega(t) = \omega ; S(t) = S$

Figure 4.7: Fourth-order RUNGE–KUTTA integration scheme for the state ω

⁶J.R. Cash and A.H. Karp. A variable order Runge–Kutta method for initial value problems with rapidly varying right-hand sides. *ACM Transactions on Mathematical Software*, 16(3):201–222, 1990. ISSN 0098-3500. DOI: 10.1145/79505.79507

Table 4.2: BUTCHER tableau for fifth-order RUNGE–KUTTA integrator. The notation is given in the upper right corner.

integration of ordinary differential equations (ODE). The present application of these integration schemes is special for two reasons. Firstly, the integrand, namely the state ω , depends on a second variable that also evolves with time, namely the stress. In order to solve for both variables, they were uncoupled as explained in section 4.2 (see also fig. 4.2). Secondly, the integrand does not necessary need to be smooth, since jumps in the state by means of the constitutive function g_{Δ} are allowed.

In order to evaluate the effects of these two specialities of the system, a benchmark test for the different integration schemes is carried out. As a benchmark problem may serve the compression of a fully periodic single crystal in [1 2 3] orientation. The mechanical BVP is solved by means of a spectral solver. The sample is compressed with a rate of deformation $\dot{F} = -1 \cdot 10^{-3} \text{ s}^{-1}$ in direction of the z-axis for a time of $t = 500 \text{ s}$ with varying step size $\Delta t = 0.05 - 50 \text{ s}$, which leads to a final strain of $\varepsilon_{zz} \approx -0.7$. The reference solution is calculated with the explicit EULER integrator at a step size of $\Delta t = 0.005 \text{ s}$, so ten times smaller than the smallest tested step size. Figure 4.9 shows the results of the benchmark test for a simple phenomenological constitutive model⁷ at two different state tolerances, and for the nonlocal model presented in this work. A couple of observations can be made for the simulations with the phenomenological model:

- None of the non-error controlling state integrators (explicit EULER, explicit RUNGE-KUTTA, fixed-point iteration) could reach step sizes larger than $\Delta t = 10 \text{ s}$, while the adaptive RUNGE-KUTTA could reach $\Delta t = 20 \text{ s}$ for low state tolerance, and the adaptive EULER went up to $\Delta t = 50 \text{ s}$ for both state tolerances.
- The relative error in the stress component in loading direction scales perfectly linearly with the time step for all integrator types up to a time step $\Delta t \lesssim 1 \text{ s}$. Above that, individual simulations deviated from this linear scaling behavior, while the general trend is preserved.
- In most of the simulations the error in stress is little influenced by the type of state integrator.
- Either the adaptive EULER, or the adaptive RUNGE-KUTTA are always best in terms of the relative error.
- The relative error in the stress is only slightly—if at all—improved by a decrease in the state tolerance from $1 \cdot 10^{-4}$ to $1 \cdot 10^{-6}$.
- At the same step size the computation time is always highest for the higher order methods (explicit and adaptive RUNGE-KUTTA).
- The computation time scales inversely linear with the time step for the explicit state integrators (explicit EULER, explicit

$\omega = \omega(t_0) ; S = S(t_0) ; g_{\text{RK}}^1 = 0$
For $i = 1, \dots, 5$
$\widetilde{\Delta t} = c_{i+1} \Delta t$
$\widetilde{F}(t) = F(t_0) + c_{i+1} \Delta F$
$g_{\text{RK}}^i = g(S, \omega)$
$\omega = \omega(t_0) + \sum_{j=2}^{i+1} a_{ji} g_{\text{RK}}^{j-1} \Delta t$
$\omega = \omega + g_{\Delta}(S, \omega)$
integrate $S(\omega, F = \widetilde{F}, \Delta t = \widetilde{\Delta t})$
$g_{\text{RK}}^6 = g(S, \omega)$
$\omega = \omega(t_0) + \sum_{i=1}^6 b_i g_{\text{RK}}^i \Delta t$
$\epsilon = \sum_{i=1}^6 d_i g_{\text{RK}}^i \Delta t$
$\omega = \omega + g_{\Delta}(S, \omega)$
integrate $S(\omega)$
$\omega(t) = \omega ; S(t) = S$

Figure 4.8: Fifth-order RUNGE-KUTTA CASH-KARP integration scheme for the state ω

⁷ J.R. Rice. Inelastic constitutive relations for solids: an internal variable theory and its application to metal plasticity. *J. Mech. Phys. Solids*, 19: 433-455, 1971; and J.W. Hutchinson. Bounds and Self-Consistent Estimates for Creep of Polycrystalline Materials. *Proceedings of the Royal Society A: Mathematical, Physical and Engineering Sciences*, 348:101-127, 1976

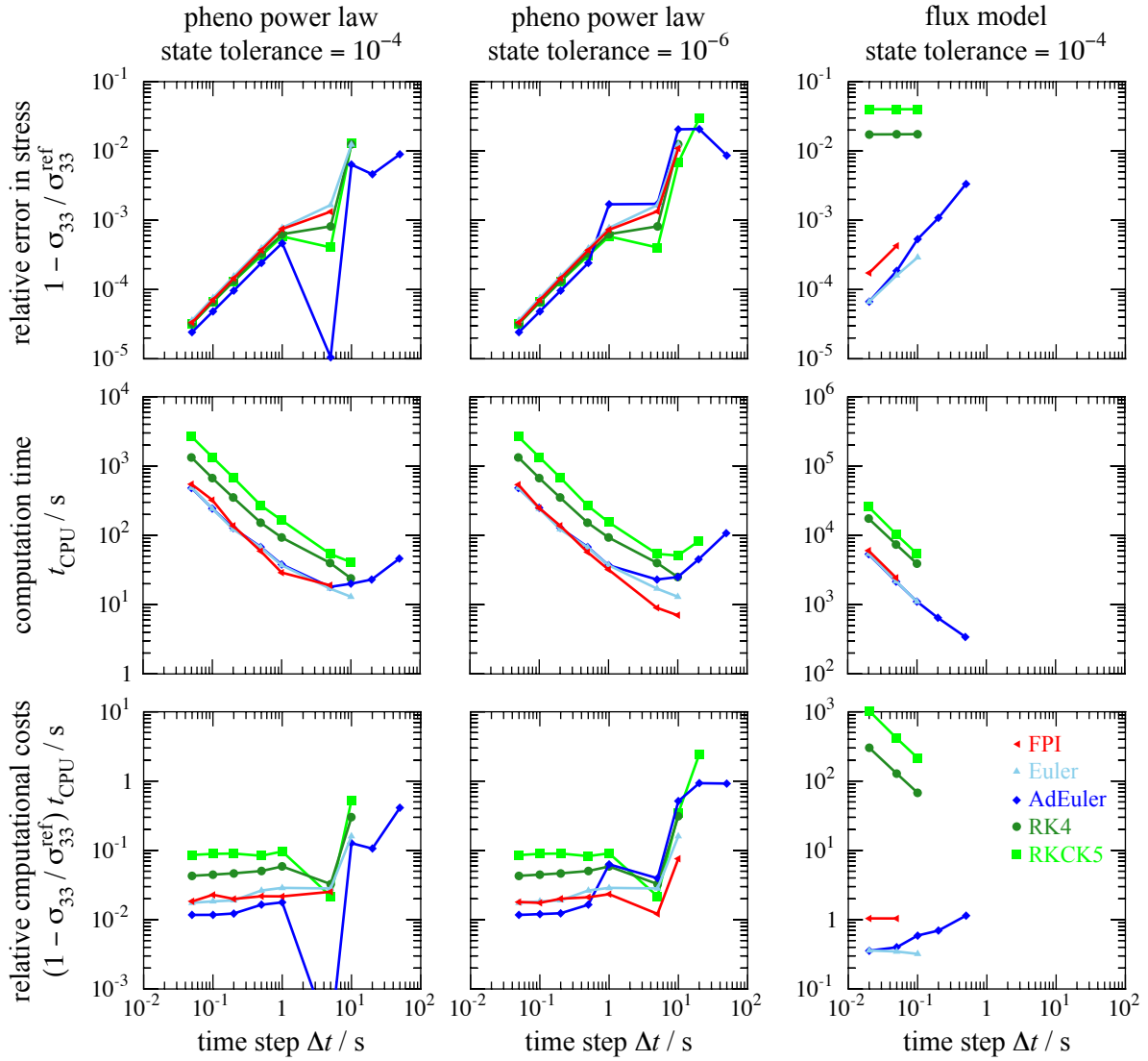


Figure 4.9: Effect of time step on the relative error in the stress for different state integrators (red triangle: fixed-point iteration; light blue triangle: explicit EULER; blue diamond: adaptive EULER; dark green: 4th order RUNGE-KUTTA; light green: 5th order adaptive RUNGE-KUTTA). Left two columns show the results for a simple phenomenological power-law for two different state tolerances: the right column show the results for the nonlocal model.

RUNGE–KUTTA), as well as for the adaptive and implicit integrators up to the point where no cutbacking or iteration is needed. Beyond this point, additional internal evaluations due to cutbacks (adaptive EULER, adaptive RUNGE–KUTTA) or iterations (fixed-point iteration) raise the computation time again.

- The adaptive EULER integrator at low state tolerance has the least computational cost per relative error for all step sizes.

For the flux model the following observations can be made:

- Again the adaptive EULER integrator could reach five times larger step sizes than all other state integrators. The fixed-point iteration procedure finished the loadcase only for very small step sizes ten times smaller than for the adaptive EULER.
- In contrast to the results obtained from the phenomenological model the relative error differs a lot between the state integrators for the nonlocal model. For the higher order methods (explicit and adaptive RUNGE–KUTTA) the error does not change at all with varying time step and is about two orders larger than for the other integrators. For the first order methods (explicit EULER, adaptive EULER, fixed-point iteration) the error is similar and again depends linearly on the time step.
- For all integrator types the computation time is inversely proportional to the step size and highest for the higher order methods.

In summary, one can say that for a local constitutive model the higher order RUNGE–KUTTA methods can slightly improve the accuracy of the solution, but at the expense of an increased computational effort. However, for the nonlocal model, the solution even deteriorates and becomes independent of the stepsize, so the order of convergence is several orders worse than expected. One possible reason for this can be the uncoupling of the stress and state integration. While this works for models where the state indeed evolves much slower than the stress (as usually in any phenomenological model), it seems to pose problems for the nonlocal flux model. Then, the state, namely the dislocation density, may well evolve as fast as (or even faster than) the stress. Additionally, the discontinuous jumps in the state evolution introduced by the g_{Δ} function may be a reason for the decrease in the convergence order. So, at least in the present benchmark the higher order methods do not pay off for the state integration. On the other hand, the fixed-point iteration procedure proposed by [Kalidindi et al., 1992] reveals an appealing combination of high accuracy and low computational costs. However, it does not converge for large step sizes, which led [Kalidindi et al., 1992] to the introduction of an additional criterion that controls the step size. The explicit EULER integrator is comparable to the fixed-point iteration, but allows for slightly larger step sizes. The best

performance both for the phenomenological and for the flux model was obtained for the adaptive EULER integrator, which revealed a comparable error to the other low order methods, but allowed for the largest step sizes at still very low computational costs (see also table 4.3).

method	formulation	error control	order	observed order	costs	stability
fixed-point iteration	implicit	no	?	1	low	low
explicit EULER	explicit	no	1	1	low	high
adaptive EULER	explicit	yes	1	1	low	very high
explicit RUNGE-KUTTA	explicit	no	4	≤ 1	high	high
adaptive RUNGE-KUTTA	explicit	yes	5	≤ 1	high	high

Table 4.3: Properties of different state integrators

4.3 Internal state variables

The internal state variables ω comprise all the dislocation densities as defined in section 3.1.2. They are stored in a one-dimensional array ordered by dislocation type and corresponding slip system.

$$\omega = \left[\begin{array}{l} \varrho_{e+u}^1, \varrho_{e-u}^1, \varrho_{s+u}^1, \varrho_{s-u}^1, \varrho_{e+b}^1, \varrho_{e-b}^1, \varrho_{s+b}^1, \varrho_{s-b}^1, \varrho_{e\pm}^1, \varrho_{s\pm}^1, \\ \varrho_{e+u}^2, \varrho_{e-u}^2, \varrho_{s+u}^2, \varrho_{s-u}^2, \varrho_{e+b}^2, \varrho_{e-b}^2, \varrho_{s+b}^2, \varrho_{s-b}^2, \varrho_{e\pm}^2, \varrho_{s\pm}^2, \\ \dots \\ \varrho_{e+u}^N, \varrho_{e-u}^N, \varrho_{s+u}^N, \varrho_{s-u}^N, \varrho_{e+b}^N, \varrho_{e-b}^N, \varrho_{s+b}^N, \varrho_{s-b}^N, \varrho_{e\pm}^N, \varrho_{s\pm}^N \end{array} \right] \quad (4.27)$$

For the time integration of the state variables the two constitutive functions g and g_Δ are needed, which describe the continuous evolution and possible jumps in the state respectively. Due to the transport of dislocations this state evolution cannot be described by an ordinary differential equation, but it also contains some spatial derivatives (see eq. (3.37)). In the following, it will first be described how this partial differential equation is solved numerically; then, a complete description of the constitutive functions that contain the state evolution can be given.

4.3.1 Finite volume upwind scheme for the dislocation transport

The incorporation of the transport of dislocations into the constitutive model renders the evolution equations for the dislocation density a system of partial differential equations (see eq. (3.37)). In order to be able to integrate these PDEs, a finite volume (FV) scheme will be employed. The differential equation is integrated over the WIGNER-SEITZ cell of volume V that surrounds each discrete material point. By means of the STOKES theorem, the volume integral of the flux divergence

$$\int_V \operatorname{div} \mathbf{f} \, dV = \oint_{\partial V} \mathbf{f} \cdot \mathbf{a} \, dA = \sum_n \tilde{\mathbf{f}}^n \cdot \mathbf{a}^n A^n \quad (4.28)$$

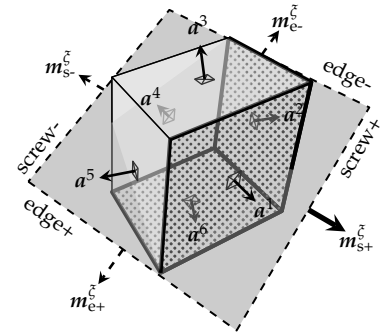


Figure 4.10: Deformed material point with exemplary slip plane $\tilde{\zeta}$ (inclined) in intermediate configuration. Interface normals correspond to those of fig. 4.1. Dashed vectors on slip plane periphery indicate directions $\tilde{\mathbf{m}}_p^z$ of dislocation motion for a positive shear increment (loop expansion). Positive screw dislocations traveling along $\tilde{\mathbf{m}}_{s+}^z$ (thick peripheral vector) leave the material point volume (and enter the neighboring volume, if existent) through the dotted interfaces on right, front, and bottom defining the set S_{s+}^z .

is replaced by summing the fluxes⁸ that pass through the volume surfaces A^n with outward unit normal \mathbf{a}^n (see fig. 4.10). The mean dislocation flux \tilde{f}^n at the interface n takes either the value f from the central point or f^n from a neighboring point n such that it fulfills the following upwind scheme:

$$\tilde{f}^n = \begin{cases} f & \text{if } f \cdot \mathbf{a}^n > 0 \\ f^n & \text{if } f \cdot \mathbf{a}^n \leq 0 \text{ and } f^n \cdot \mathbf{a}^n < 0 \\ 0 & \text{otherwise} \end{cases} \quad (4.29)$$

This scheme is only first-order accurate and can produce significant numerical diffusion, but it is unconditionally bounded and highly stable, and ensures that dislocation density is transferred only in direction of the actual dislocation motion.

A non-existent neighboring cell (corresponding to a free surface) or a neighboring cell centered on a material point of differing crystal orientation or phase (corresponding to a grain or phase boundary) requires special treatment of fluxes. At free surfaces the entering flux is simply set to zero and any leaving flux remains unaltered, since it is assumed to be not impeded by, *e.g.*, oxide layers.

Grain and phase boundaries are treated as interfaces with reduced transmissivity for dislocations. Therefore, the dislocation flux density at the interface is decreased by the factor χ . This factor could account for the lattice compatibility allowing interchange of dislocations between two neighboring material points. For a grain boundary, a transmissivity factor $0 \leq \chi < 1$ is defined so that just a fraction of the dislocation flux can enter the neighboring cell.

$$\operatorname{div} f = \frac{1}{V} \sum_n \chi^n \tilde{f}^n \cdot \mathbf{a}^n A^n \quad (4.30)$$

If the transmissivity is set equal to one in the case of material point neighbors that share the same orientation and phase, one can reformulate the divergence term of the flux density consistent to the rate equations given in section 3.2.

$$\operatorname{flux} \Phi_{pu}^{\xi} = -\frac{1}{V} \sum_n \chi^n \tilde{f}_p^{\xi,n} \cdot \mathbf{a}^n A^n \quad (4.31)$$

Any remainder of the dislocation flux that is not transmitted to the neighboring cell, *i.e.*, the equivalent of the flux multiplied by $(1 - \chi)$, gets stuck in front of the grain boundary and is left there as blocked dislocation density. This provides a sink term for the unblocked and a corresponding source term for the blocked dislocation density.

$$\operatorname{interf} \Phi_{pu}^{\xi} = -\frac{1}{V} \sum_{n \in S_p^{\xi}} (1 - \chi^n) \tilde{f}_p^{\xi,n} \cdot \mathbf{a}^n A^n \quad (4.32a)$$

$$\operatorname{interf} \Phi_{pb}^{\xi} = +\frac{1}{V} \sum_{n \in S_p^{\xi}} (1 - \chi^n) \tilde{f}_p^{\xi,n} \cdot \mathbf{a}^n A^n \operatorname{sign} v_p^{\xi} \quad (4.32b)$$

⁸ the dislocation type p and the slip system ξ are dropped for brevity

The sign operator in eq. (4.32b) defines the blocked direction of the immobile dislocation density. The set of interfaces with leaving fluxes is defined as (see fig. 4.10)

$$S_p^{\tilde{c}} = \left\{ n \mid \mathbf{f}_p^{\tilde{c}} \cdot \mathbf{a}^n > 0 \right\}. \quad (4.33)$$

A special treatment is needed in case that the resolved shear stress changes its sign between neighboring material points and the flux vectors of the neighboring cells point towards each other. Then, the dislocations should clearly stop moving somewhere close to the interface in between the two neighbors. In the present implementation, dislocations would, however, be able to move back and forth between the neighboring cells, and generate an ever growing plastic deformation in both cells. Hence, these dislocations are forced to stop at the interface by setting the transmissivity for this case equal to zero. Then, all dislocations change their state from unblocked to blocked and cannot generate any further plastic slip. However, if the sign of the resolved shear stress changes in one of the cells, then the respective dislocations on both sides are remobilized again and able to move in opposite direction. The discretization of the spatial domain into cells entails an upper bound for the propagation speed of dislocations. Within a time step Δt on average all dislocations that exceed a velocity \hat{v} will have crossed the entire cell volume.

$$\hat{v} = \frac{\sqrt[3]{V}}{\Delta t} \quad (4.34)$$

To ensure that no dislocation can move further than the next neighboring cell the dislocation velocity will be limited to \hat{v} . In practice though this will be guaranteed by choosing an appropriate time step.

4.3.2 State evolution functions

With the reformulation of the dislocation transport according to section 4.3.1 one is able to express the constitutive functions g and g_Δ in a consistent manner. For brevity, only the first entries of the functions are given, which correspond to the ten different dislocation types on the first slip system. All consecutive entries can be obtained by replacing the superscript for the first slip system by

the corresponding index.

$$\begin{aligned}
g(\mathcal{S}, \omega) = & \left[\text{flux} \Phi_{e+u}^1 + \text{interf} \Phi_{e+u}^1 + \text{mult} \Phi_{e+u}^1 + \text{mono} \rightarrow \text{di} \Phi_{e+u}^1 + \text{jog} \Phi_{e+u}^1, \right. \\
& \text{flux} \Phi_{e-u}^1 + \text{interf} \Phi_{e-u}^1 + \text{mult} \Phi_{e-u}^1 + \text{mono} \rightarrow \text{di} \Phi_{e-u}^1 + \text{jog} \Phi_{e-u}^1, \\
& \text{flux} \Phi_{s+u}^1 + \text{interf} \Phi_{s+u}^1 + \text{mult} \Phi_{s+u}^1 + \text{mono} \rightarrow \text{di} \Phi_{s+u}^1, \\
& \text{flux} \Phi_{s-u}^1 + \text{interf} \Phi_{s-u}^1 + \text{mult} \Phi_{s-u}^1 + \text{mono} \rightarrow \text{di} \Phi_{s-u}^1, \\
& \text{interf} \Phi_{e+b}^1 + \text{mono} \rightarrow \text{di} \Phi_{e+b}^1, \\
& \text{interf} \Phi_{e-b}^1 + \text{mono} \rightarrow \text{di} \Phi_{e-b}^1, \\
& \text{interf} \Phi_{s+b}^1 + \text{mono} \rightarrow \text{di} \Phi_{s+b}^1, \\
& \text{interf} \Phi_{s-b}^1 + \text{mono} \rightarrow \text{di} \Phi_{s-b}^1, \\
& \text{mono} \rightarrow \text{di} \Phi_{e\pm}^1 + \text{climb} \Phi_{e\pm}^1 + \text{athAnn} \Phi_{e\pm}^1, \\
& \left. \text{mono} \rightarrow \text{di} \Phi_{s\pm}^1 + \text{cross-slip} \Phi_{s\pm}^1, \dots \right]
\end{aligned} \tag{4.35}$$

$$\begin{aligned}
g_{\Delta}(\mathcal{S}, \omega) = & \left[\text{di} \rightarrow \text{mono} \Psi_{e+u}^1 + \text{remob} \Psi_{e+u}^1, \right. \\
& \text{di} \rightarrow \text{mono} \Psi_{e-u}^1 + \text{remob} \Psi_{e-u}^1, \\
& \text{di} \rightarrow \text{mono} \Psi_{s+u}^1 + \text{remob} \Psi_{s+u}^1, \\
& \text{di} \rightarrow \text{mono} \Psi_{s-u}^1 + \text{remob} \Psi_{s-u}^1, \\
& \text{remob} \Psi_{e+b}^1, \\
& \text{remob} \Psi_{e-b}^1, \\
& \text{remob} \Psi_{s+b}^1, \\
& \text{remob} \Psi_{s-b}^1, \\
& \text{di} \rightarrow \text{mono} \Psi_{e\pm}^1, \\
& \left. \text{di} \rightarrow \text{mono} \Psi_{s\pm}^1, \dots \right]
\end{aligned} \tag{4.36}$$

4.3.3 Efficient cutback procedure

As a consequence of eq. (4.34), the time step that is needed to integrate the state can be much smaller than the time step required by the mechanical boundary value solver at the end of the simulation chain. Thus, excessive cutbacking is often needed inside the material subroutine. Due to the non-locality of the constitutive model, the integration of neighboring material points is not independent of each other. Hence, also the time step has to be chosen such that neighboring material points do not diverge in time. One way of ensuring synchronized time steps in all neighbors is a fixed time step throughout the whole computational domain. This means that the one integration point that needs the smallest time step determines the time step for all. As a result, a lot of cutbacks would be done for integration points that do not need any cutback. Especially for localized deformation problems as, *e.g.*, in indentation simulations, this would lead to an inefficient time integration that hinders practical application. In order to circumvent this, an efficient cutback scheme is introduced that only

locally uses small time steps where needed. This cutback scheme, in principal, allows each integration point to have its own time step. Nonetheless, if an IP does not converge and has to do a cutback, then all neighbors have to do a cutback as well, so that non-converged IPs are always surrounded by a layer of already converged IPs, all doing the same time integration step. A detailed description of this synchronization procedure can be found in appendix A.8.

Validation and comparison to experiments

5

Validation of the dislocation transport equations

Any dislocation slip activity entails a motion of dislocation defects through the material. This motion is often negligible in a completely homogeneous material with much larger extent than the average dislocation spacing. Then, the motion of dislocations does not become apparent, although the consequence, namely the shearing of the material, does have macroscopical effect. On a small scale, the motion of dislocations can play an important role, since it may on the one hand lead to accumulation of dislocations of one sign, *i.e.*, GNDs, where the boundary conditions are not uniform; on the other hand, it may lead to starvation in areas where dislocation multiplication does not suffice to compensate the outflow of dislocations due to their motion, *i.e.*, where there are not enough active dislocation sources. For this reason, the transport of dislocations is incorporated as an essential part of the constitutive model.

In this chapter, the transport of dislocations is evaluated for a simple test case that allows to directly compare to an analytical solution, hence, that allows to validate the implementation of the constitutive equations.

5.1 Problem setup

The test case used here is the simplest scenario one can possibly think of, namely the cross-section of a single expanding dislocation loop in an fcc crystal under simple shear in direction of the BURGERS vector. The cross-section is taken normal to the BURGERS vector and the slip plane normal. The effect of curvature on the driving force will be neglected, so that the scenario can be described by two infinitely long edge dislocations of opposite sign (see fig. 5.1). The orientation is chosen such that the x -axis points in direction of the BURGERS vector, the y -axis in direction of the slip plane normal, and the z -axis in line direction of the positive edge dislocation. A dislocation source is assumed to be located at the origin of this coordinate system emitting exactly two dislocations of opposite sign. Under sufficiently high positive simple shear τ_{xy} , these two dislocations separate from each other, *i.e.*, the positive edge dislocation moves in positive x -direction and the negative

edge dislocation in negative x -direction. The separation of the two dislocations is restricted to a distance $L = 1 \mu\text{m}$ by two impenetrable boundaries at $x = \pm 0.5 \mu\text{m}$.

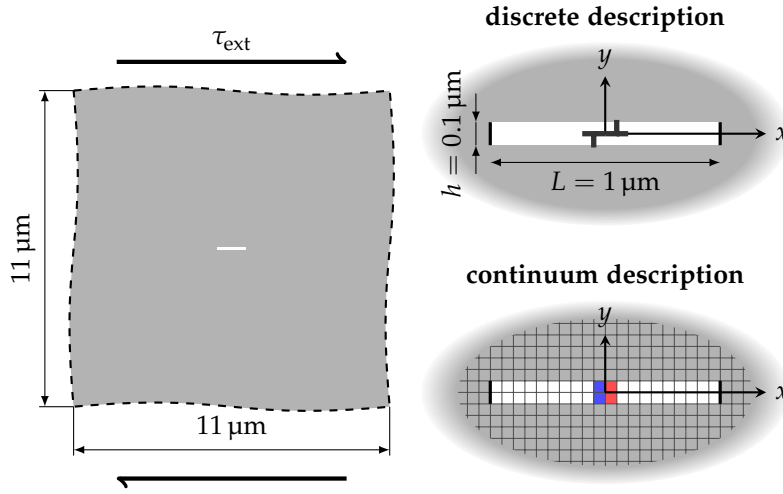


Figure 5.1: Periodic geometry of a narrow slit of plastically deforming material (white) in an elastic matrix (gray). The crystal orientation of the slit is chosen such that the slip system has its BURGERS vector aligned with the x -direction and its slip plane normal with the y -direction. The boundary between the plastic slit and the elastic matrix is set impenetrable for dislocations. The two edge dislocations in the discrete description are represented by dislocation densities of positive edge type (red) and negative edge type (blue) in the continuum description. In the continuum description the density that corresponds to one dislocation is divided on two stacked cells.

Figure 5.1 shows the geometrical setup that is used to simulate the previously described scenario. A thin, plastically deformable strip of length $L = 1 \mu\text{m}$ and height $h = 0.1 \mu\text{m}$ is embedded in an elastic medium of size $11 \times 11 \mu\text{m}^2$. Since a spectral method is used to solve the mechanical boundary value problem, the whole geometry is periodically repeated in all directions. A two-dimensional regular grid of 220×220 points is adopted in the spectral solution method to spatially discretize the periodic domain, which corresponds to 20×2 cells inside the plastic strip. The boundary conditions enforce a simple shear stress of $\tau_{xy} = \tau_{\text{ext}} = 100 \text{ MPa}$; the normal stress components are set equal to zero; the xy , xz , and yz components of the deformation gradient are also set to zero. Due to the employed spectral method, all boundary conditions are kept *on average*, but not necessarily at the boundary of the periodic domain. The final deformation of the material is sufficiently small so that lattice rotations do not play a significant role.

In the continuum description, the two dislocations that are supposed to originate from a source in the origin of the geometry are represented by dislocation densities of positive and negative edge type (ρ_{e+} and ρ_{e-}), which are initially located directly right and left of the origin, respectively. For reasons of numerical stability of the spectral method, one dislocation is conceptually distributed on two stacked cells. Hence, each of these two cells contains an initial dislocation density of

$$\rho_{e+/-}^0 = \frac{1}{2} \frac{1}{(h/2)^2} = \frac{2}{h^2} = 2 \cdot 10^{14} \text{ m}^{-2}. \quad (5.1)$$

For the moment, any microstructural evolution apart from the transport of dislocations is disregarded. This means that all rate terms in the state evolution eq. (3.37) are dropped except for the

flux and the interface blocking terms. Moreover, the state equations have to be formulated only for the first slip system. Thus, the 120 state evolution equations that the constitutive model usually requires for the simulation of fcc crystals reduce to only four.

$$\partial_t \varrho_{e+u} = \text{flux} \Phi_{e+u} + \text{interf} \Phi_{e+u} \quad (5.2a)$$

$$\partial_t \varrho_{e-u} = \text{flux} \Phi_{e-u} + \text{interf} \Phi_{e-u} \quad (5.2b)$$

$$\partial_t \varrho_{e+b} = \text{interf} \Phi_{e+b} \quad (5.2c)$$

$$\partial_t \varrho_{e-b} = \text{interf} \Phi_{e-b} \quad (5.2d)$$

For simplicity, the dislocation velocity is assumed to have a linear viscous velocity law with mobility B .¹

$$v = B\tau \quad (5.3)$$

Table 5.1 lists the values used for the material properties. For a straightforward analytical treatment, the elasticity tensor is assumed isotropic.

Property		Value	Unit
isotropic elasticity constants	C_{11}	100	GPa
	C_{12}	50	GPa
isotropic shear modulus	μ	25	GPa
Poisson ratio	ν	0.333	
length of BURGERS vector	b	0.3	nm
dislocation mobility	B	30	$\mu\text{m s}^{-1} \text{GPa}^{-1}$

The flux density vector f_p is defined as the product of the dislocation density ϱ_p and the velocity vector v_p , which points into the direction of motion of the respective dislocation type.

¹ Any velocity law could be used here to demonstrate the correct behavior of the dislocation transport.

Table 5.1: Material parameters used for the simulation of the cross-section of an expanding dislocation loop.

5.2 Results

Figure 5.3 shows the evolution of the excess dislocation density and the accumulated plastic shear deformation along the plastic strip. As also seen in fig. 5.2, the positive applied shear stress drives the two dislocation densities of different sign apart: the positive edge dislocation density ϱ_{e+} moves in positive x -direction and the negative density ϱ_{e-} in negative x -direction. While the dislocation density is initially concentrated in the cells directly left and right of the origin, the transport of the dislocation density also leads to a diffusive broadening of the density into a bell-shaped distribution along the direction of motion. The boundary at $x = \pm 0.5 \mu\text{m}$, then, enforces the density to pile up; and the entire density is again concentrated in a sharp peak. The total sum of the dislocation density is preserved throughout the entire process. The accumulated plastic slip evolves according to the transport of the dislocation density (see lower graph in fig. 5.3). First it grows mainly for the central cells that contain the initial dislocation density. Then the plastic slip expands to the left and right along with the expanding dislocation density. Finally, when all the dislocation density has gathered at the boundary, the accumulated plastic slip amounts to exactly $3 \cdot 10^{-3}$ throughout the plastic strip.

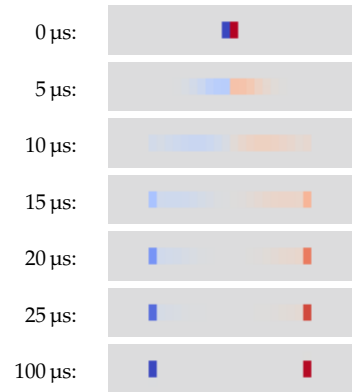


Figure 5.2: Distribution of excess dislocation density in the plastic strip at time $t = 0, 5, 10, 15, 20, 25,$ and $100 \mu\text{s}$.

This corresponds to a shear of b/h , the shear that results from a dislocation of **BURGERS** vector b crossing a volume of height h .

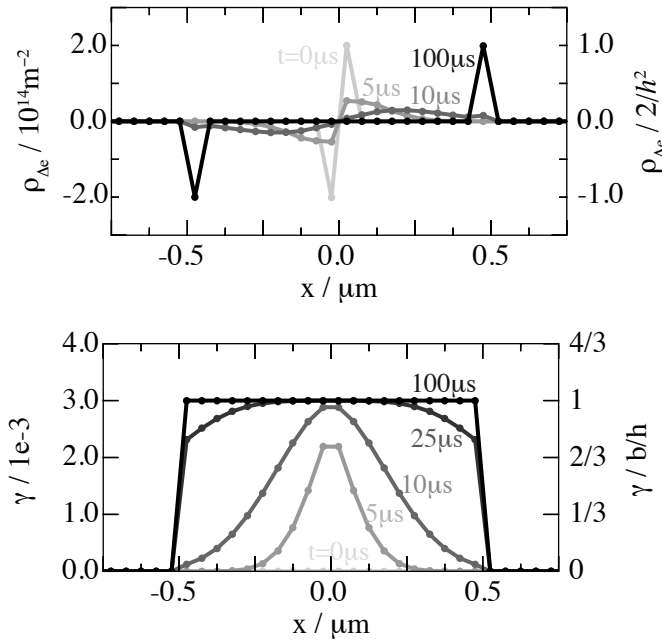


Figure 5.3: Evolution of the dislocation density (top) and the corresponding accumulated plastic slip (bottom) along the plastic strip for different times $t = 0, 5, 10, 25,$ and $100 \mu\text{s}$ (from light gray to black).

The plastic deformation inside the plastic strip results in elastic strains in the surrounding matrix that ensure the compatibility of the material. These strains entail a stress field in the material, which is shown in the left column of fig. 5.4.² The (homogeneous) externally applied shear stress is subtracted from the xy shear component in order to visualize only the internally induced stresses. Although the origin of the deformation in the strip does not play a role for the evolving stress field, here, it is precisely the motion of dislocations through the material. Hence, the elastic stress field can also be analytically derived by textbook formulas from the position of the two dislocations at the end of the simulation. Those stress fields are shown in the second column of fig. 5.4. They perfectly match the internal stress fields that are induced by the plastic deformation of the strip in the simulation. This is also demonstrated by the plots in the third column of fig. 5.4 that compare the simulated and the analytical results along the dashed lines shown on the maps. Only slight deviations are visible directly at the boundary, where the analytical solution predicts higher values. Indeed, exactly on the boundary, the analytical solution has a discontinuity with values tending towards positive and negative infinity on both sides.³

5.3 Discussion

The flux equations for the dislocation density lead to the expected redistribution of density in the material according to the applied driving forces. As an important condition, the dislocation content is

² Due to the isotropic elasticity, the components yz and xz are zero.

See appendix A.2 for the analytical expressions of the stress field around an edge dislocation of infinite length in an isotropic medium

³ The discontinuity in the analytical stress field stems from the fact that the equations are strictly spoken not valid inside the core region of a dislocation.

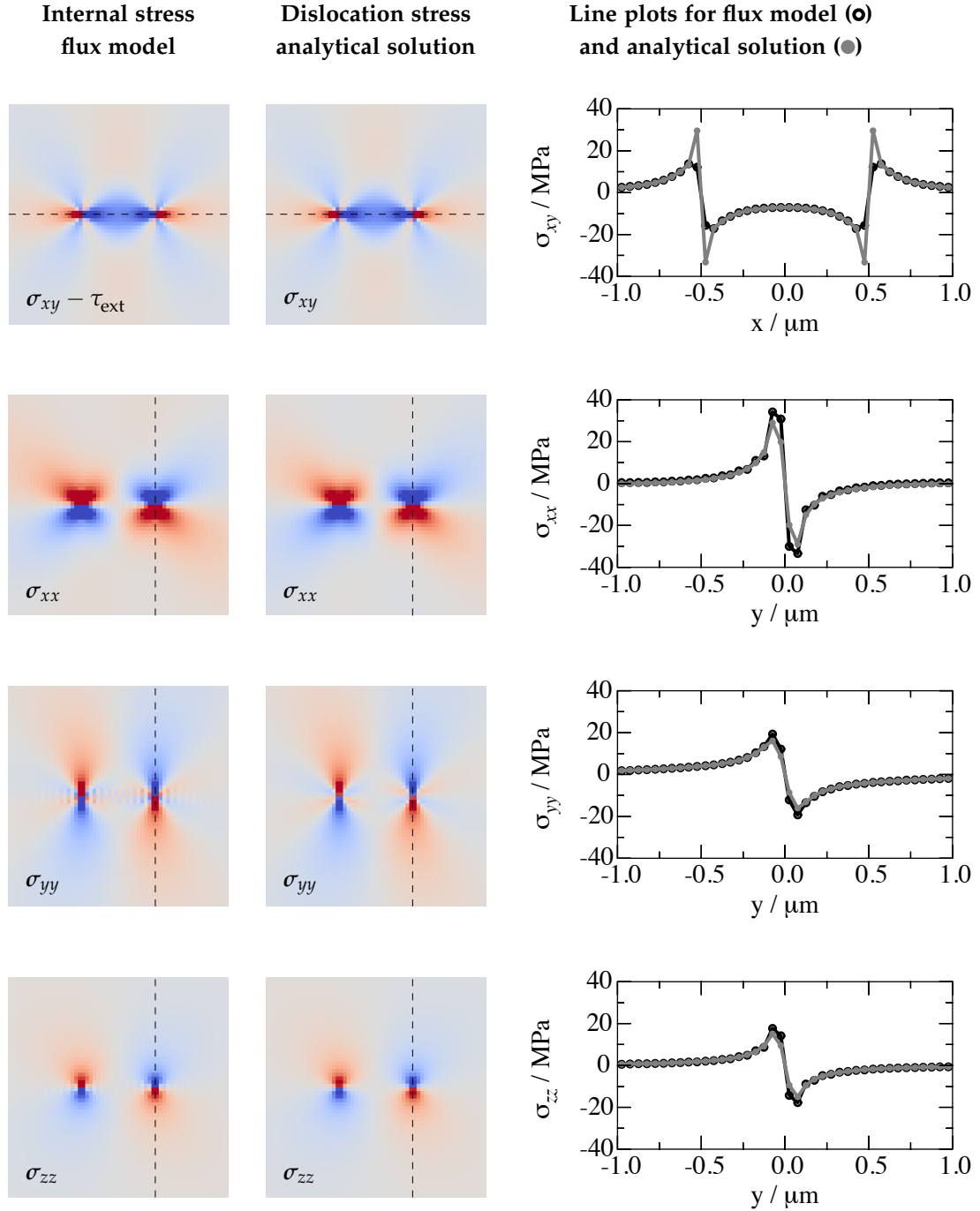


Figure 5.4: Non-zero components of the dislocation stress tensor as obtained in the flux model (first column) and the analytical solution (second column). For the flux model, the dislocation stress results from the overall stress field minus the externally applied stress. The third column shows plots along the lines as indicated in the maps to the left of both the continuum (black circles) and the analytical solution (gray dots).

maintained, so no dislocation sinks or sources are artificially introduced by the dislocation flux. It should be noted that, in general, dislocation motion entails the generation of new dislocation line length by virtue of the expansion of the dislocation loop's diameter. However, the present implementation of the dislocation flux does not aim at a precise description of this production term, but rather at a way to describe the redistribution of dislocation density on a scale larger than a single dislocation loop. Later on, the production of new dislocation density via (generation of dislocation sources and subsequent) loop expansion will be implicitly covered by a source term based on standard mean free path arguments (see section 3.2.4). A different approach is followed by Sedláček et al.⁴ and more recently by Hochrainer et al.⁵ and Sandfeld et al.⁶ They consider the dislocation curvature as an additional state variable, which allows to evolve the dislocation density due to a change in the dislocation curvature. However, also with these formulations, the key aspect of dislocation multiplication, namely the conditions under which new dislocation sources are formed, remains to be specified.

As one perceives in figs. 5.2 and 5.3, the implementation of the dislocation transport induces significant numerical diffusion that is manifested by the broadening of the dislocation density distribution. This diffusion is a property of the first-order upwind scheme that is applied for the integration of the partial differential equations of the dislocation density. Although higher-order integration schemes exist that are able to significantly decrease numerical diffusion (*e.g.*, the class of weighted essentially non-oscillatory schemes based on work by Liu et al.⁷), the additional computational costs would obstruct the application of the model in many cases. Moreover, most higher-order numerical schemes can lead to negative values for the dislocation density. On the other hand, Baskaran et al.⁸ demonstrated that a semi-discrete description of dislocations, with the BURGERS vector "smeared out" in the slip plane, matches discrete results for double-pileups of dislocations to a high extent.⁹ This is in agreement with the observation that, despite the numerical diffusion of the dislocation density, the accumulated plastic slip perfectly corresponds to the density distribution. In particular, at the end of the simulation, the accumulated plastic slip in the entire deformed strip corresponds to the deformation that would have been created by a dislocation loop that expanded exactly about this distance.

The eigenstrains induced by the plastic deformation in the central strip are shown to result in a stress field that matches the stress field calculated analytically from the positions of the dislocations.¹⁰ This observation is a direct consequence of the fact that the presence of dislocations entails a plastic incompatibility that is balanced with a corresponding elastic incompatibility, provided the crystal lattice maintains overall compatibility. The corresponding lattice strains result in stresses that have to fulfill the elastic

⁴ R. Sedláček, J. Kratochvíl, and E. Werner. The importance of being curved: bowing dislocations in a continuum description. *Philosophical Magazine*, 83(31):3735–3752, 2003. ISSN 1478-6435. DOI: 10.1080/14786430310001600213

⁵ T. Hochrainer, M. Zaiser, and P. Gumbsch. A three-dimensional continuum theory of dislocation systems: kinematics and mean-field formulation. *Philosophical Magazine*, 87(8-9):1261–1282, 2007. ISSN 1478-6435. DOI: 10.1080/14786430600930218

⁶ S. Sandfeld, T. Hochrainer, M. Zaiser, and P. Gumbsch. Continuum modeling of dislocation plasticity: Theory, numerical implementation, and validation by discrete dislocation simulations. *Journal of Materials Research*, 26(05):623–632, 2011. ISSN 0884-2914. DOI: 10.1557/jmr.2010.92

⁷ X.-D. Liu, S. Osher, and T. Chan. Weighted Essentially Non-oscillatory Schemes. *Journal of Computational Physics*, 115(1):200–212, 1994. ISSN 0021-9991. DOI: 10.1006/jcph.1994.1187

⁸ R. Baskaran, S. Akarapu, S.D. Mesarovic, and H.M. Zbib. Energies and distributions of dislocations in stacked pile-ups. *International Journal of Solids and Structures*, 47(9):1144–1153, 2010. ISSN 0020-7683. DOI: 10.1016/j.ijsolstr.2010.01.007

⁹ Baskaran et al. [2010] identify the ratio between the pileup length and the slip plane spacing as key parameter that determines how well semi-discrete and discrete simulations match. If this ratio was approximately larger than five, then, they state, the difference between the two descriptions would be negligible.

¹⁰ The high frequency oscillations in the normal stress components close to the plastic strip in the first column of fig. 5.4 can be attributed to numerical instabilities of the spectral solver.

equilibrium equations.¹¹ In essence, this means that at least the long-range stress field of dislocations is captured by solving strain-compatibility and stress equilibrium in conjunction with the transport of dislocations as also recently remarked by Liu et al.¹²

5.4 Conclusions

The transport of two infinitely long edge dislocations of opposite sign in an isotropic elastic medium was simulated and compared to analytical solutions in order to validate the implementation of dislocation transport in the constitutive model. The following conclusions can be drawn.

- The dislocation flux equations lead to transport of dislocations as expected: under a positive applied shear stress, the two edge dislocations of opposite sign separate from each other by moving in opposite directions.
- Along its path, the dislocation density produces plastic slip that exactly amounts to the expected values of one BURGERS step over the height of the considered volume.
- The total sum of dislocation density is preserved during the redistribution of dislocation density.
- The employed integration scheme for the partial differential equation of the dislocation flux induces significant numerical diffusion.
- Despite the numerical diffusion, the final state of dislocation density and plastic slip matches the analytical solution, when the entire density is accumulated at the impenetrable boundaries.
- Due to compatibility requirements, the plastic deformation of the central, plastic strip enforces elastic stresses in the surrounding matrix. This leads to a stress field that matches the stress field that is calculated from the position of the dislocations at the end of the simulation. This means that (at least the long-range) stress field of dislocations is captured by solving mechanical equilibrium in a compatible continuum in conjunction with the transport of dislocations.
- The partial differential equations of the constitutive model adequately reflect the consequences of dislocation motion, in particular with respect to generation of strain and stress.

¹¹ B.A. Bilby and E. Smith. Continuous Distributions of Dislocations. III. *Proc. Roy. Soc. London A*, 236(1207):481–505, 1956

¹² Z.L. Liu, X.M. Liu, Z. Zhuang, and X.C. You. A multi-scale computational model of crystal plasticity at submicron-to-nanometer scales. *International Journal of Plasticity*, 25(8): 1436–1455, 2009. ISSN 0749-6419. DOI: 10.1016/j.ijplas.2008.11.006

6

Comparison of discrete and continuum dislocation dynamics simulations

Discrete dislocation simulations can serve as a benchmark for a continuum theory of dislocation dynamics. Although computationally expensive, they are an important tool for the study of the behavior of dislocations, since they retain the discrete nature of dislocations, hence, naturally include much details as, *e.g.*, reactions between dislocations that have to be incorporated by additional formulations in a continuum model.

It might be possible to obtain equally detailed results with a simple continuum model, if the resolution is chosen sufficiently high such that individual dislocation segments can be resolved. However, this should not be the aim of a continuum model, which has its advantages when it is applied to larger structures. Nonetheless, an important question is what happens at the transition from a discrete to a continuum representation of dislocations. This can help to improve modeling of dislocation plasticity especially at small scales.

Hence, a continuum mechanical boundary value problem is sought that is simple (analytically tractable) and dominated by dislocation redistribution during plastic deformation such that size effects might be expected and studied. A suitable two-dimensional problem for this purpose is a plastic inclusion in an elastic and fully compatible matrix with both being infinitely long in one dimension. Broadly speaking, such a situation is reminiscent of the softest grain within a polycrystalline aggregate starting to deform.

6.1 Problem setup

6.1.1 Geometry

The periodic geometry considered here is shown in fig. 6.1. It extends infinitely along the out-of-plane z direction and consists of a periodic elastic medium (gray) with a translation period of $11L \times 11L$ into which a circular plastic inclusion (white) of diameter L is embedded. Inclusion sizes of $L = 1$ and $10 \mu\text{m}$ are selected. The overall domain is single-crystalline and oriented such that the one

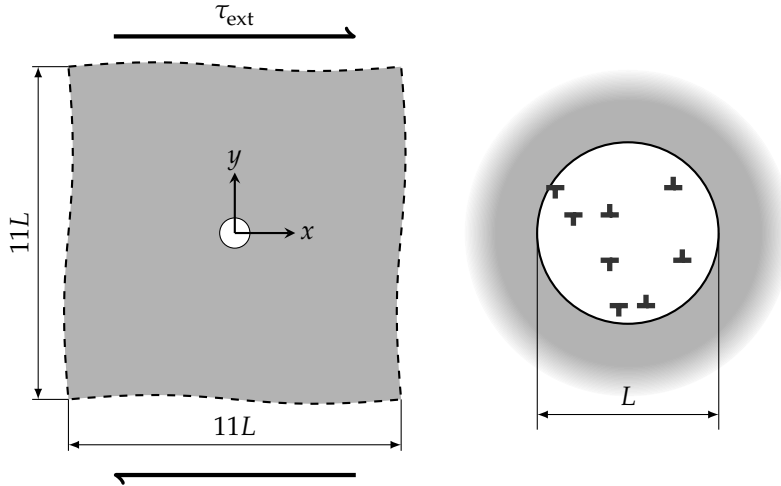


Figure 6.1: Periodic geometry of a circular inclusion of plastically deforming material (white) inside an elastic matrix (gray). The crystal orientation of the inclusion is chosen such that the slip system has its BURGERS vector aligned with the x direction and its slip plane normal with the y direction. The boundary between the plastic inclusion and the elastic matrix is set impenetrable for dislocations.

slip system considered here has its slip plane normal along y and its slip direction along x .¹ A regular grid of $550 \times 550 \times 1$ points is adopted in the (two-dimensional) spectral solution method to spatially discretize the periodic domain resulting in close to $2 \cdot 10^3$ cells of size $l = L/50$.

6.1.2 Inclusion analysis

The static equilibrium of the circular inclusion under imposed shear stress might be derived from ESHELBY'S solution of an ellipsoid experiencing an eigenstrain and embedded in an infinite isotropic medium, both having μ and ν as shear modulus and Poisson ratio, respectively. When viewing the circular inclusion as an ellipsoid with axes $a_x = a_y = L$ and $a_z = \infty$ the (constant) shear stress within such an ellipsoid is related to the (pure and also constant) shear eigenstrain by²

$$\sigma_{xy}^{\text{incl}} / \varepsilon_{xy}^{\text{E}} = -\frac{2\mu}{1-\nu} \frac{LL}{(L+L)^2} = -\frac{1}{4} \frac{2\mu}{1-\nu}. \quad (6.1)$$

Thus, a (simple) shear eigenstrain of

$$\gamma_{\text{E}} := 4(1-\nu) \frac{\tau_{\text{ext}}}{\mu} \quad (6.2)$$

leads to equilibrium between internal and externally applied shear stress, i.e., $\tau_{\text{ext}} + \sigma_{xy}^{\text{incl}} = 0$ within the inclusion.³

For a limited dislocation content inside the inclusion (as is assumed here—see next section) this stress-free eigenstrain γ_{E} may, however, not be attainable by plastic shearing. The maximum plastic (simple) shear of a horizontal strip at coordinate y in the inclusion for a homogenous distribution of initial dislocation density ϱ_{e}^0 is given by

$$\gamma_{\text{max}}(y) = \varrho_{\text{e}}^0 b L / 2 \sqrt{1 - (y/0.5L)} \quad (6.3)$$

Hence, an external stress of

$$\tau_{\text{ext}}^* = \mu \frac{\varrho_{\text{e}}^0 b L}{8(1-\nu)} \quad (6.4)$$

¹ For an fcc lattice this corresponds to EULER angles equal to $\varphi_1 = 230.769^\circ$, $\phi = 114.095^\circ$, $\varphi_2 = 116.565^\circ$ in Bunge [1982] notation.

² T. Mura. *Micromechanics of Defects in Solids*. Martinus Nijhoff Publishers, Dordrecht, 2nd edition, 1987

³ Since, ESHELBY'S analytical solution holds for an infinite medium, eq. (6.2) is only an approximation to the present application. As tests with an ideally plastic inclusion showed, the surrounding elastic medium is, however, sufficiently large, so that deviations from the analytical solution in terms of the total strain of less than 2% are expected.

will just suffice to exhaust the “plastic capacity” of a circular inclusion, *i.e.*, reaches the condition $\gamma_E = \gamma_{\max}$ for given size and dislocation content at all coordinates y .

6.1.3 Initial and boundary conditions

An equal amount of positive and negative edge dislocations is homogeneously distributed within the inclusion (white area in fig. 6.1), *i.e.*, no net BURGERS vector content remains. In the DDD case, equal numbers of positive and negative edge dislocations are put at random inside the area that makes up the inclusion. In the CDD cases, this is carried out in a homogenized fashion by starting with constant and equal densities $\rho_{e+}^0 = \rho_{e-}^0 = \rho_e^0/2$ for positive and negative edge dislocations on all material points falling within the inclusion.

The matrix (gray area in fig. 6.1) is free of dislocations and can, thus, only deform elastically. The boundary between elastic matrix and plastic inclusion is impenetrable for dislocations; the flux at this interface is set to zero. All dislocations that arrive at the interface are immobilized, relabeled internally as “blocked” dislocations, and do not contribute to plastic slip anymore. Combined with the fact that dislocation multiplication has been disregarded for the moment, this leads to a constant overall dislocation density within the plastic inclusion.

Periodic displacements are enforced in the CDD simulations with a period of $11L \times 11L$ in x and y directions.

The sample is subjected to simple shear by means of a constant applied shear stress of $\tau_{\text{ext}} = 25, 100, \text{ and } 400 \text{ MPa}$. According to eq. (6.2) this corresponds to a shear strain of at most 0.043, hence lattice rotations are expected to be relatively small and can be neglected in the DDD simulations. The applied stress is hold until an equilibrated state is reached. In the DDD simulations this is defined by the rate of plastic slip dropping below $3 \cdot 10^{-7} \text{ s}^{-1}$. As it is not easily possible to directly check for the sliprate in the CDD simulations, a fixed simulation time is used; the simulation time is chosen such that the final plastic velocity gradient L_p attains similar or lower values than in the DDD case.

In order to obtain results comparable to the CDD, the DDD simulations were repeated up to 500 times and averaged.

6.1.4 Material parameters

Table 6.1 lists the values used for the material properties. Matrix and inclusion share the same isotropic elasticity tensor. The particular value of dislocation mobility is not crucial for the results, since the simulations are followed in time until an equilibrated situation (negligible shear rate) is reached.

Property		Value	Unit
isotropic elasticity constants	C_{11}	100	GPa
	C_{12}	50	GPa
isotropic shear modulus	μ	25	GPa
Poisson ratio	ν	0.333	
length of BURGERS vector	b	0.3	nm
dislocation mobility	B	3	$\mu\text{m s}^{-1} \text{GPa}^{-1}$

Table 6.1: Material parameters used for the simulation of the plastic inclusion pictured in fig. 6.1.

6.1.5 CDD simulations

A reduced form of the constitutive equations of the CDD model is used here in order to achieve comparable results to the DDD simulations. Only dislocation transport, blockage, and dipole formation and dissociation are incorporated into the state evolution equations. With one active slip system and only edge type dislocation density present the evolution equations reduce to

$$\begin{aligned}
\partial_t \rho_{e+u} &= \text{flux} \Phi_{e+u} + \text{interf} \Phi_{e+u} + \text{mono} \rightarrow \text{di} \Phi_{e+u} + \text{di} \rightarrow \text{mono} \Psi_{e+u} / \Delta t \\
\partial_t \rho_{e-u} &= \text{flux} \Phi_{e-u} + \text{interf} \Phi_{e-u} + \text{mono} \rightarrow \text{di} \Phi_{e-u} + \text{di} \rightarrow \text{mono} \Psi_{e-u} / \Delta t \\
\partial_t \rho_{e+b} &= \text{interf} \Phi_{e+b} + \text{mono} \rightarrow \text{di} \Phi_{e+b} \\
\partial_t \rho_{e-b} &= \text{interf} \Phi_{e-b} + \text{mono} \rightarrow \text{di} \Phi_{e-b} \\
\partial_t \rho_{e\pm} &= \text{mono} \rightarrow \text{di} \Phi_{e\pm} + \text{di} \rightarrow \text{mono} \Psi_{e\pm} / \Delta t
\end{aligned} \tag{6.5}$$

The dislocation velocity is assumed to have a linear viscous velocity law with mobility B .

$$v = B\tau \tag{6.6}$$

6.1.6 DDD simulations

The discrete dislocation dynamics model calculates the shear stress induced by each of the $i = 1, \dots, N$ dislocations located at positions \mathbf{r}^i by means of the standard textbook equation for a straight edge dislocation of infinite length (see appendix A.2). The superposition of all those dislocation stress fields plus the applied external shear stress then acts as the local driving force for dislocation motion.

$$v^i = B \left(\tau_{\text{ext}} + \sum_{j=1, j \neq i}^N \sigma_{xy}(\mathbf{r}^i - \mathbf{r}^j) \right) \tag{6.7}$$

An exception to this are dislocations that form a very close dipole with a distance of below one BURGERS vector length; the velocity of these dislocations are explicitly set to zero.

A simple two-dimensional discrete dislocation dynamics code is used, which is implemented in the commercially available software MatlabR2011a by MathWorks with an external Fortran routine for the computationally intensive parts of the calculation. The time integration of the dislocation velocities uses a first order adaptive

EULER scheme that allows to control the numerical error of the dislocation positions.

6.1.7 Evaluation methods

Since there are no dislocation sources considered, the (positive) strain at position (x, y) can be derived from the positive/negative dislocation content that passed the dividing plane at that position from the left/right. In case of CDD simulations, this leads to

$$\gamma(x, y) = b \int_{-\frac{l}{2}}^x \varrho_{e+}^0 - \left(\varrho_{e+} + \frac{1}{2} \varrho_{e\pm} \right) d\tilde{x} + b \int_x^{\frac{l}{2}} \varrho_{e-}^0 - \left(\varrho_{e-} + \frac{1}{2} \varrho_{e\pm} \right) d\tilde{x}. \quad (6.8)$$

For the DDD simulations the change from initial, r_i^0 , to final, r_i , positions of all individual dislocations is evaluated on a grid corresponding to the CDD simulations. Then the plastic shear at the cell center (x, y) of a cell of size l follows as

$$\begin{aligned} \gamma(x, y) &= \frac{b}{l} \sum_{i \in P} \text{sign} \left(\mathbf{m}_i \cdot \left(\mathbf{r}_i - \mathbf{r}_i^0 \right) \right) \\ \text{with } P &= \left\{ i : \left| \left(\mathbf{r}_i - (x, y, 0) \right) \cdot (0, 1, 0) \right| < \frac{l}{2} \right\} \\ &\cap \left\{ i : \left(\mathbf{r}_i^0 - (x, y, 0) \right) \cdot \left(\mathbf{r}_i - (x, y, 0) \right) < 0 \right\} \end{aligned} \quad (6.9)$$

where the first set comprises all dislocations traveling in the horizontal strip of the cell and the second set comprises all dislocations that have passed through the cell.

6.2 Comparison of DDD and CDD simulation results for a plastic inclusion under different external stresses

First, the DDD and CDD results are compared for one specific inclusion size and dislocation density, before systematically varying those quantities.

6.2.1 Results

Figure 6.2 shows maps of the plastic shear γ , the total dislocation density ϱ_e , and the excess dislocation density $\varrho_{\Delta e}$ for a plastic inclusion of size $L = 1 \mu\text{m}$ and with a dislocation content of $\varrho_e^0 = 2 \cdot 10^{14} \text{ m}^{-2}$. DDD and CDD simulation results are directly put on top of each other for better comparison.

The plastic shear of the circular inclusion systematically increases from a load of 25 to 400 MPa. For the CDD, it is always very uniform along the horizontal direction and, except for 400 MPa, also along the vertical direction, which is characteristic for an ESHELBY type inclusion. At 400 MPa the plastic capacity is exhausted in the

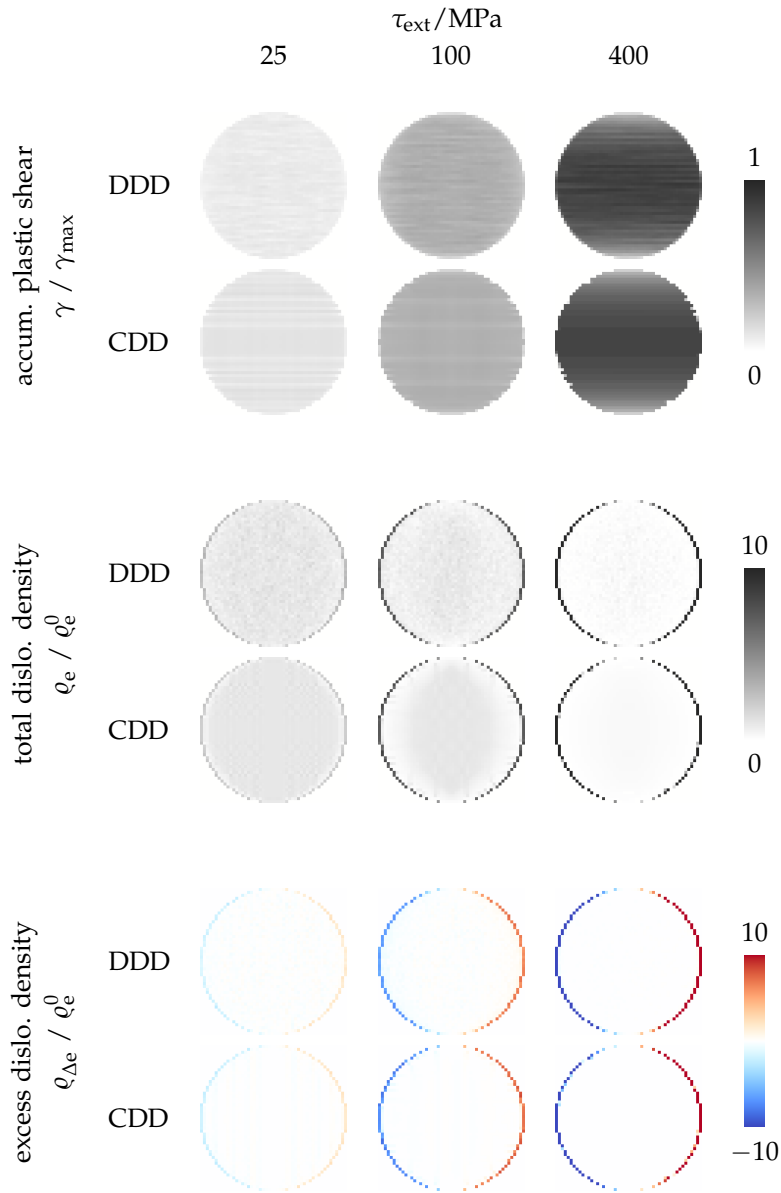


Figure 6.2: Comparison of CDD and DDD simulation results of plastic shear γ , total dislocation density ρ_e , and excess dislocation density $\rho_{\Delta e}$ for a plastic inclusion of size $L = 1 \mu\text{m}$ inside an elastic matrix. The homogeneous initial dislocation density for the CDD is $\rho_e^0 = 2 \cdot 10^{14} \text{m}^{-2}$, which corresponds to 158 dislocations in the DDD. A shear stress of $\tau_{\text{ext}} = 25, 100, 400 \text{MPa}$ was applied.

entire inclusion. The variation of plastic shear observed along the vertical direction at this stress is due to the corresponding change of inclusion width, *i.e.*, maximum distance each dislocation can glide, which according to eq. (6.3) restricts the plastic capacity from 0.03 (black) in the middle to zero (white) at the top. The plastic shear in the DDD results reaches the same absolute level. However, the distribution along the horizontal axes is somewhat different in that the inclusion deforms slightly more in the center, but forms a small, yet recognizable boundary layer of reduced strain at the walls.

In the selected crystal orientation and load case, positive (edge) dislocations are pushed along the positive x -direction and negative ones move in the opposite direction. They stop when the local internal stress field equilibrates the externally applied stress, or when they reach the hard interface between plastic inclusion and the elastic matrix. When turning to the profiles of total and excess dislocation density in fig. 6.2, the increasing redistribution of dislocations towards the inclusion walls with increasing stress is obvious. Starting from close to the walls the zone of depleted total dislocation density gradually grows towards the inclusion center at increasing loads. In consequence, the polarity of dislocations is building up at the walls.

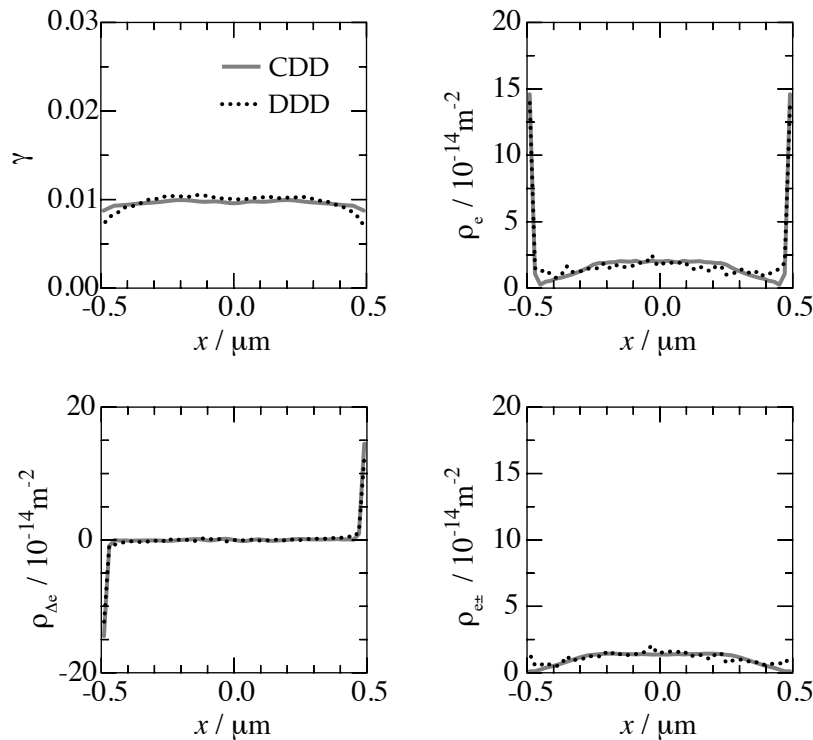


Figure 6.3: Comparison of CDD and DDD simulation results of plastic shear γ , total dislocation density ρ_e , excess dislocation density $\rho_{\Delta e}$, and dipole dislocation density $\rho_{e\pm}$ along the “equator” of a plastic inclusion of size $L = 1 \mu\text{m}$ inside an elastic matrix. The homogeneous initial dislocation density for the CDD is $\rho_e^0 = 2 \cdot 10^{14} \text{ m}^{-2}$, which corresponds to 158 dislocations in the DDD. A shear stress of $\tau_{\text{ext}} = 100 \text{ MPa}$ was applied.

Figure 6.3 shows line plots of the plastic shear and the total, excess, and dipolar dislocation density along the “equator” of the inclusion at the intermediate stress level. Again, the monopolar character of the dislocation density at the wall becomes apparent. In contrast,

the majority of dislocations in the center of the inclusion forms dipoles.⁴ Due to a lack of potential partners of opposite sign, dipoles do not easily form close to the walls. Nonetheless, in the DDD simulations, dipoles can move if they are pushed by a third dislocation. This leads to a slight diffusion of dipolar dislocation density towards the walls, thus the non-vanishing dipolar dislocation density at the walls for the DDD results.⁵ A similar effect is not observed in the CDD results, since dipoles are considered immobile here. This also explains why the depletion zone of the total dislocation density in fig. 6.2 is less pronounced for the DDD than for the CDD results.

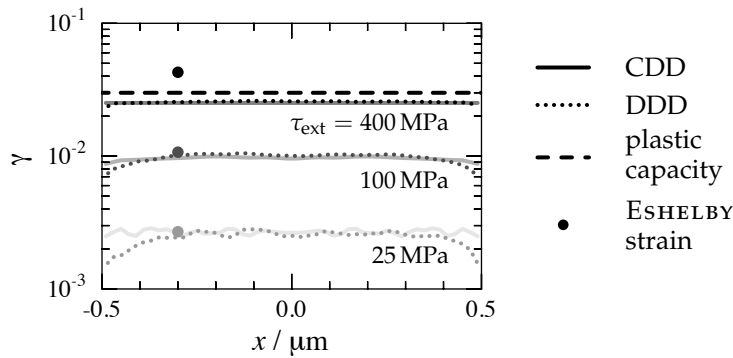
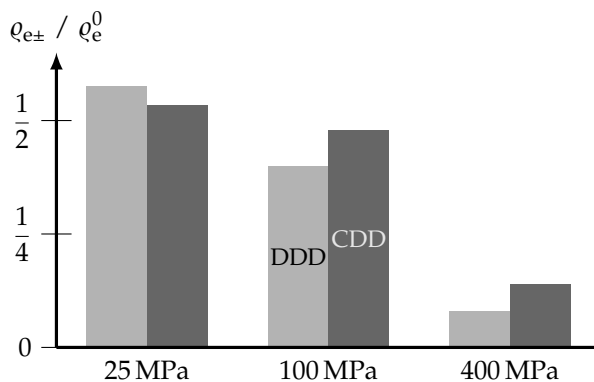


Figure 6.4 shows the plastic shear along the “equator” of the inclusion at increasing stresses of $\tau_{\text{ext}} = 25, 100,$ and 400 MPa. The level of plastic shear strain naturally increases with increasing stress. However, while at the lower stress levels of 25 and 100 MPa the plastic capacity suffices to accomplish the requested strain that is given by the ESHELBY strain γ_E , at the high stress of 400 MPa the plastic capacity is exhausted and the ESHELBY strain cannot be reached. The reason why the plastic capacity is not fully exploited at 400 MPa is the small fraction of dislocations that is bound in very close dipoles (see fig. 6.5).



⁴ Dipoles in the discrete simulations where identified by an algorithm searching for dislocations that mutually have the same nearest neighbor of opposite sign located at an angle between 10° and 80° .

⁵ Motion of a dislocation dipole does, however, *not* generate any plastic strain.

Figure 6.4: Plastic shear along the equator of a circular inclusion of size $L = 1 \mu\text{m}$ inside an elastic medium at an applied stress of $\tau_{\text{ext}} = 25, 100,$ and 400 MPa. The dislocation density inside the plastic inclusion amounts to $2 \cdot 10^{14} \text{m}^{-2}$. Solid lines show the results of the CDD simulations, dotted lines those of the DDD simulations; the dashed line corresponds to the maximum plastic shear that can be generated; the bullet symbol corresponds to the shear strain of an ideal ESHELBY inclusion.

Figure 6.5: Dipole dislocation density $\rho_{e\pm}$ in a plastic inclusion of size $L = 1 \mu\text{m}$ with dislocation content $\rho_e^0 = 2 \cdot 10^{14} \text{m}^{-2}$ as obtained by DDD and CDD simulations at different levels of applied stress $\tau_{\text{ext}} = 25, 100,$ and 400 MPa.

6.2.2 Discussion

Although on average, the plastic shear in CDD and DDD match very well, the shear profiles along the slip direction are qualitatively different, since the DDD clearly reveals a boundary layer at the wall where the CDD does not. The reason for this lies in the quantization of dislocation slip in the DDD, which by design is not part of the CDD model. A detailed analysis of this effect follows later in section 6.4 and section 6.5.

The formation of dislocation dipoles plays an important role in the mechanical behavior of the system, since it affects the amount of available mobile carrier density. While in the DDD simulations, dipoles naturally form by two dislocations of opposite sign passing in close distance to each other, the formation in the CDD simulations is modeled by a rate equation that is based on the stable dipole distance. As shown in fig. 6.5, the dipole dislocation densities of CDD and DDD simulations match indeed very well, which indicates that the CDD model for the dipole formation and dissociation works well. Reasons for the still present differences between CDD and DDD might stem for instance from the inhomogeneous distribution of dipole heights⁶ or additional reactions between dipoles and a third dislocation or two dipoles.⁷ In contrast to the current treatment, the effect of dislocation dipoles on the mechanical behavior is often described by a local flowstress (see for instance Groma et al.⁸ and Sandfeld et al.⁹). An athermal flowstress is usually attributed to precipitate hardening or—in case of multiple slip—to interactions with forest dislocations from inclined slip systems; both obstacles cannot be thermally activated and, hence, constitute a fix barrier for dislocation motion. Yet, for the case of a single slip system and without any precipitates a local flowstress is also often attributed to a “jamming” of dislocations due to the formation of stable dipoles. Similar to the description of a flowstress in multiple slip, it is related to the square root of the dislocation density:

$$\tau_{\text{cr}} = \alpha \mu b \sqrt{\rho} \quad (6.10)$$

with α usually chosen close to 0.3. The dislocation velocity law in the present case then reads

$$v = \begin{cases} B(\tau - \tau_{\text{cr}}) & \text{if } \tau_{\text{cr}} < \tau \\ 0 & \text{if } \tau_{\text{cr}} \geq \tau \geq -\tau_{\text{cr}} \\ B(\tau + \tau_{\text{cr}}) & \text{if } \tau < -\tau_{\text{cr}} \end{cases} \quad (6.11)$$

Although a local flowstress might often be adequate to model the effect of dislocation dipoles, it can not be used here in the context of a nonlocal dislocation based constitutive model. As shown in fig. 6.6, the distribution of total dislocation density after plastic straining exhibits a high-frequency oscillation between regions of high and low values (typically vertically aligned) that is not observed in the corresponding DDD results. The reason for its

⁶ P. Eisenlohr. *On the role of dislocation dipoles in unidirectional deformation of crystals*. PhD thesis, Universität Erlangen-Nürnberg, 2004

⁷ P.D. Neumann. The interactions between dislocations and dislocation dipoles. *Acta Metall.*, 19(11):1233–1241, 1971. DOI: 10.1016/0001-6160(71)90057-5

⁸ I. Groma, F.F. Csikor, and M. Zaiser. Spatial correlations and higher-order gradient terms in a continuum description of dislocation dynamics. *Acta Materialia*, 51(5):1271–1281, 2003. ISSN 1359-6454. DOI: 10.1016/S1359-6454(02)00517-7

⁹ S. Sandfeld, T. Hochrainer, M. Zaiser, and P. Gumbsch. Continuum modeling of dislocation plasticity: Theory, numerical implementation, and validation by discrete dislocation simulations. *Journal of Materials Research*, 26(05):623–632, 2011. ISSN 0884-2914. DOI: 10.1557/jmr.2010.92

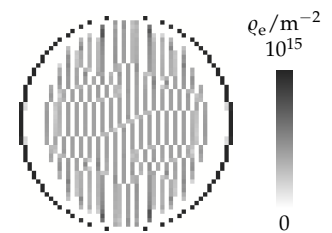


Figure 6.6: Spurious high frequency spatial oscillation of the total dislocation density that occurs when a local flow stress due to dislocations on the same slip system is introduced in the constitutive law of the CDD model.

occurrence lies in an inherent instability of the system of partial differential equations for the state evolution when using a kinetic equation such as eq. (6.11).

For a more straightforward stability analysis of the state evolution equations, the terms for the dislocation blockage are dropped in eq. (6.5), since they do not play an essential role in the stability properties of the PDE. The evolution terms regarding the formation and dissociation of dipoles are dropped anyways, since their effect should be covered by the flowstress term in the velocity eq. (6.11). The resulting system of two PDEs reads

$$\partial_t \varrho_{e+} + \partial_x (\varrho_{e+} v) = 0 \quad (6.12a)$$

$$\partial_t \varrho_{e-} - \partial_x (\varrho_{e-} v) = 0 \quad (6.12b)$$

It is useful to express the evolution in terms of the total ϱ and excess dislocation density κ by a subtraction and summation of the latter two equations.¹⁰

$$\partial_t \varrho - \partial_x (\kappa v) = 0 \quad (6.13a)$$

$$\partial_t \kappa + \partial_x (\varrho v) = 0 \quad (6.13b)$$

¹⁰ In order to avoid confusion with the nabla operator the excess dislocation density is here denoted by the symbol κ and not by ϱ_Δ .

In combination with the velocity law eq. (6.10) and eq. (6.11) one obtains a system of nonlinear PDEs.

$$\partial_t \varrho - \partial_x ((B\tau - \alpha\mu bB\sqrt{\varrho}) \kappa) = 0 \quad (6.14a)$$

$$\partial_t \kappa + \partial_x ((B\tau - \alpha\mu bB\sqrt{\varrho}) \varrho) = 0 \quad (6.14b)$$

Inside the inclusion, the resolved shear stress τ is homogeneous in space and slowly varying with time. Hence, τ will be treated as constant. With the introduction of the two constants $a = B\tau$ and $c = \alpha\mu bB$ one obtains:

$$\partial_t \varrho - \partial_x ((a - c\sqrt{\varrho}) \kappa) = 0 \quad (6.15a)$$

$$\partial_t \kappa + \partial_x ((a - c\sqrt{\varrho}) \varrho) = 0 \quad (6.15b)$$

For $c = 0$ the flowstress term disappears and the system has elliptic character and a stable and smooth solution. For non-vanishing flowstress, *i.e.*, when $c > 0$, the system has mixed, nonlinear character and cannot easily be solved. However, the linearized version of eq. (6.15) turns into a hyperbolic PDE (see appendix A.5). This indicates that small perturbations in the solution of the linearized PDE are retained. The nonlinear character of the original PDE apparently leads to an amplification of these perturbations and to instability.

Let us assume homogeneous initial conditions for eq. (6.15) with $\varrho(0, x) = \varrho_0$ and $\kappa(0, x) = 0$, which corresponds to the initial conditions of the current plastic inclusion problem. Now, a small positive perturbation in the total density is introduced. Having in mind the numerical integration on a linear grid, the perturbed grid point exhibits a slightly higher flowstress than the surrounding integration points. In case that the resolved shear stress is much

larger than the flowstress, the velocity is not very sensitive to a change in the flowstress; so the decrease in the velocity will be smaller than the increase in the dislocation density. Hence, the dislocation flux will be slightly increased and tend to level out the perturbation by moving more dislocation content to the neighbors than is entering from the neighbors.

However, if the resolved shear stress is close to the flowstress, the behavior changes. Then a small change in the dislocation density can lead to a large relative change in the velocity. For a resolved shear stress just above the flowstress, a small positive perturbation of the total dislocation density then results in a reduced dislocation flux to the neighbors and a net gain of dislocation density, while the neighboring integration points will encounter a net loss of dislocation density (see fig. 6.7). As a consequence, the flowstress of the central integration point increases and the flowstress of the neighbors decreases. This effect is self-amplifying and can lead to a complete depletion of every other integration point and a corresponding accumulation of dislocation density in between. The frequency of this oscillation is mesh dependent and does not correspond to any physical length.

For a nonlocal model that incorporates transport of dislocation density, a flowstress can lead to spurious oscillations in the solution, if the flowstress contains self-interaction of dislocations. Yet, the effect might be less pronounced if the flowstress is dominated by the interaction with other slip systems or if the applied stresses are considerably higher than the local flow stress caused by dislocation density. On the other hand, if the dislocation velocity is not modeled by a linear viscous law, but by a power-law or an exponential function, the dislocation velocity is much more sensitive to changes in the flowstress; and the occurrence of instabilities in the solution becomes more probable.

6.3 Geometric invariance

Another important question is how the mechanical behavior of the system changes with varying size: which effects occur in the DDD simulations and to which extent are they reflected by the CDD simulations?

At least four concurring characteristic lengths of the system can be identified, which influence the behavior:

1. the inclusion/grain size L ,
2. the average dislocation spacing $\lambda = \frac{1}{\sqrt{\rho}}$,
3. the average slip plane spacing h ,
4. and the BURGERS vector length b ,

where the latter is a property of the crystal lattice and is fixed.

One variation of the system occurs when the inclusion size L is changed while the number of dislocations N is kept constant. This linearly scales all positions of the dislocations such that the geometrical arrangement is maintained. In the following, this will

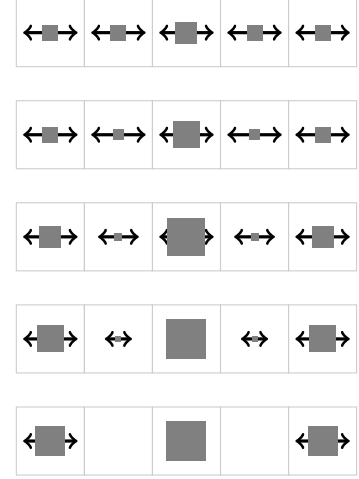


Figure 6.7: Schematic diagram explaining how oscillations in the total dislocation density can occur when the resolved shear stress is just above the flowstress. The size of the gray squares indicates the amount of dislocation density and accordingly also the height of the flowstress. The length of the arrows indicate the dislocation flux to the neighbors. A slightly increased dislocation density and flowstress at the central point leads to a lower velocity. If the relative decrease in the velocity is larger than the increase in the dislocation density, this results in a lower dislocation flux. Then, the central integration point effectively gains dislocation density while the neighbors lose dislocation density. This leads to a self-amplification and eventually to complete depletion of dislocation density at every other integration point.

be called a geometrically invariant change of the system with respect to the total number of dislocations N .¹¹

$$N = \frac{\pi}{4} \rho L^2 \quad (6.16)$$

¹¹ Since N is required to be a multiple of 2, eq. (6.16) is in general not exact.

6.3.1 Results

Figure 6.8 shows DDD simulation results of the plastic shear γ , the total dislocation density ρ_e , and the excess dislocation density $\rho_{\Delta e}$ for three different combinations of inclusion size L and dislocation content ρ_e^0 . For the simulations shown in the first two rows of fig. 6.8, L and ρ_e^0 are chosen such that the number of dislocations is the same, *i.e.*, both setups are geometrically invariant. Clearly, one can see that the plastic response of the two systems is not the same. The larger inclusion has generated much less strain than the smaller one. Also the redistribution of the dislocations differs: while in the larger, but loosely populated inclusion (top row in fig. 6.8) almost all dislocations are pushed to the walls, the smaller and denser populated inclusion (mid row in fig. 6.8) exhibits a significant amount of dislocation density remaining in the entire inclusion.

6.3.2 Discussion

As already seen, a change of the inclusion size L at constant number of dislocations N results in a different dislocation density ρ . This means that a simple scaling of the geometry entails an equivalent relative change in two of the other identified characteristic lengths of the system, namely the dislocation spacing λ and the slip plane spacing h . According to eq. (6.3), this also entails an inverse change of the plastic capacity γ_{\max} , since an increased size L leads to a quadratic reduction of the dislocation density ρ : the larger the plastic inclusion, the smaller the plastic capacity. As long as the plastic capacity suffices to accomplish the required deformation given by the ESHELBY strain γ_E , the mechanical behavior does not change. Only when the plastic capacity is exhausted, because all dislocations got either stuck at the wall or are bound in dislocation dipoles, the plastic strain is limited and declines with increasing geometry size. This is the reason for the much lower strain for the larger of the two geometrically invariant inclusions in fig. 6.8. The plastic capacity of $\gamma_{\max} = 0.003$ is much smaller than the ESHELBY shear strain $\gamma_E = 0.011$. In case that dislocation multiplication was incorporated in the simulations, there would be no defined plastic capacity and the larger inclusion would also generate a strain equal to the corresponding ESHELBY strain as long as enough mobile dislocations can be produced by dislocation sources. However, the main goal of the present study is not necessarily a one to one correlation to a real physical system, but rather the analysis of single effects on the mechanical behavior especially with regards to any size dependency. In this respect, a simple linear scaling of the

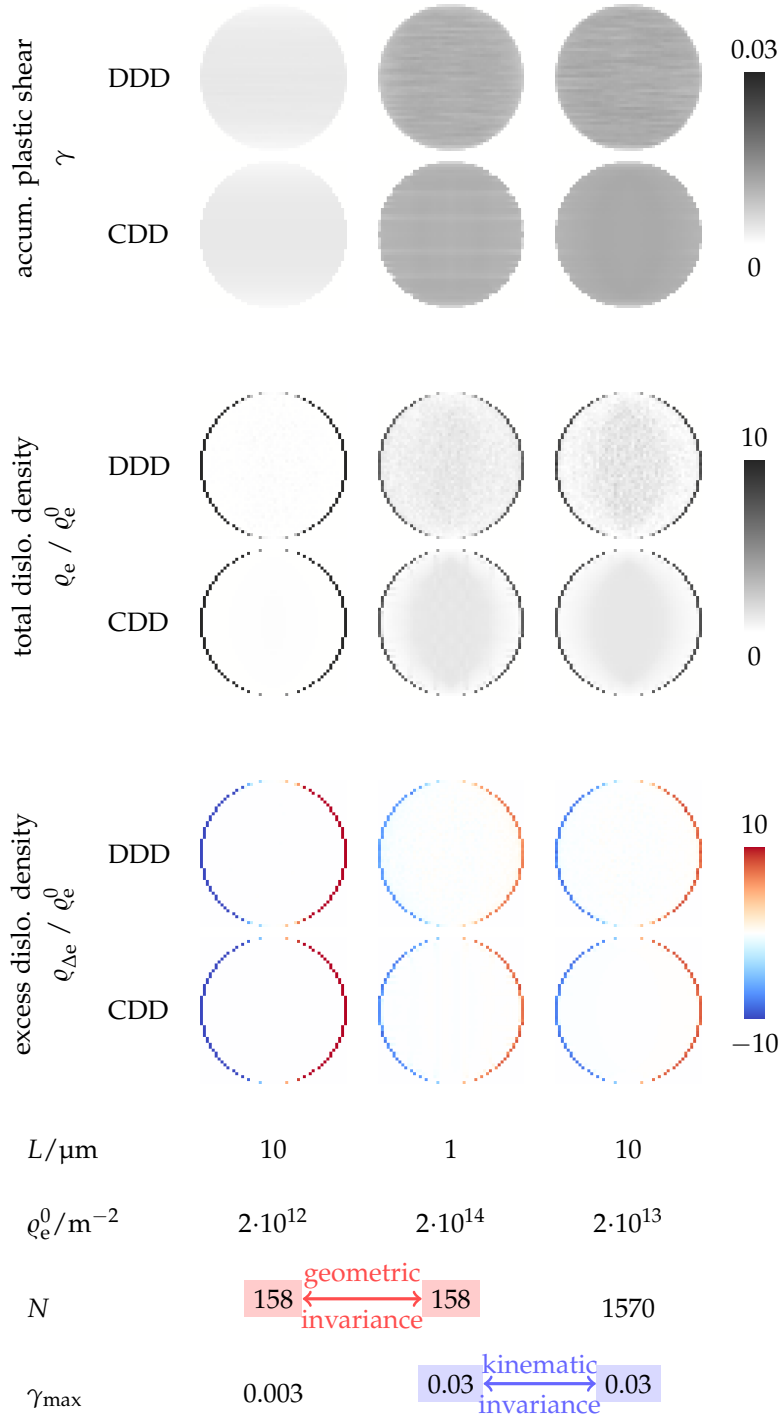


Figure 6.8: Comparison of CDD and DDD simulation results for three plastic inclusions with sizes $L = 1$ and $10 \mu\text{m}$ and dislocation densities $\rho_e^0 = 2 \cdot 10^{12}$, $2 \cdot 10^{14}$, and $2 \cdot 10^{13} \text{m}^{-2}$. The externally applied shear stress τ_{ext} is 100MPa for all three cases. The first and the second parameter setup result in the same overall number of dislocations inside the plastic inclusion, *i.e.*, *geometric invariance*; the first and the third parameter setup result in the same plastic capacity of the inclusion, *i.e.*, *kinematic invariance*. Since the number of dislocations N has to be a multiple of 2, the number of dislocations for the inclusions in the last two rows does not exactly scale by a factor of 10.

geometry at constant number of dislocations is not appropriate to study a possibly present size effect, since the change of the plastic capacity leads to different kinematic prerequisites.

6.4 Kinematic invariance

As shown in the last section, a simple scaling of the geometry, although maintaining the number of dislocations, changes the plastic capacity of the system. A consequent next step is to keep the plastic capacity of the inclusion constant while changing the system size. This so-called kinematic invariance is maintained when the dislocation density (instead of the dislocation spacing) is inversely proportional to the inclusion size (see fig. 6.9).

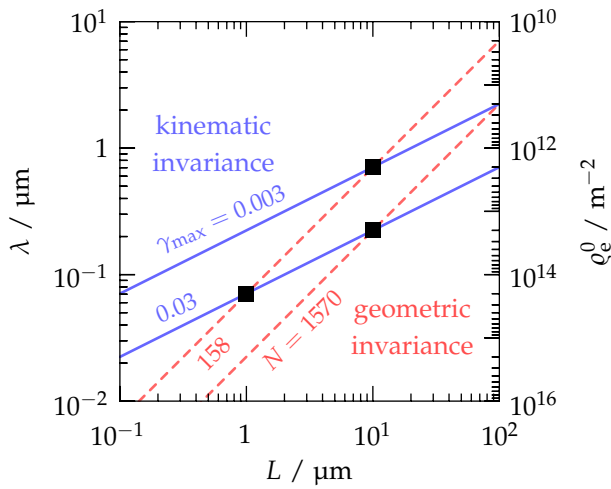


Figure 6.9: Selected combinations of size L and (constant) dislocation density ρ_e^0 in the plastic inclusion. Blue solid lines indicate coincidence of the maximum attainable plastic shear γ_{\max} (kinematic invariance), red dashed lines coincidence of the number of dislocations N (geometric invariance).

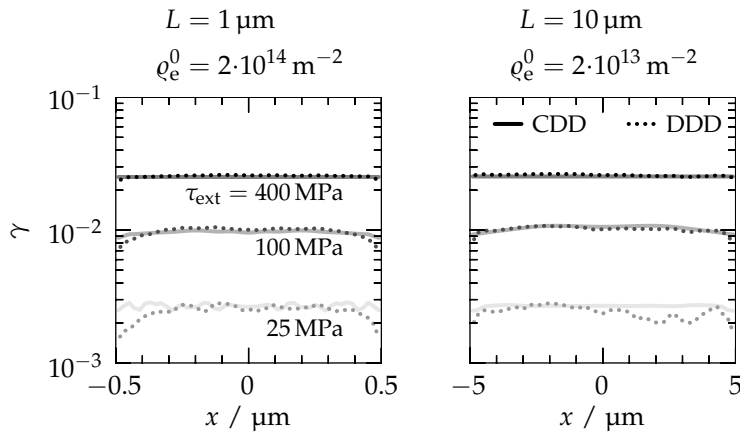


Figure 6.10: Plastic shear along the equator of the two kinematically equivalent circular inclusions of size $L = 1$ and $10 \mu\text{m}$ at an applied stress of $\tau_{\text{ext}} = 25, 100$, and 400 MPa . Solid lines show the results of the CDD simulations, dotted lines those of the DDD simulations.

6.4.1 Results

Figure 6.10 shows the plastic shear stress along the equator of the two kinematically equivalent inclusions of size $L = 1$ and $10 \mu\text{m}$ at three different levels of applied stress. The predicted plastic response of CDD and DDD matches to a high degree. Due to the

kinematic invariance, there is also almost no difference between the plastic response of the two different inclusions at same stress. Only directly at the walls, the smaller inclusion tends to form a slight boundary layer of relatively lower strain, while such a boundary layer is almost not noticeable for the larger inclusion. A corresponding pileup of excess dislocations is, however, relatively weak as shown in fig. 6.11 for the intermediate stress level.

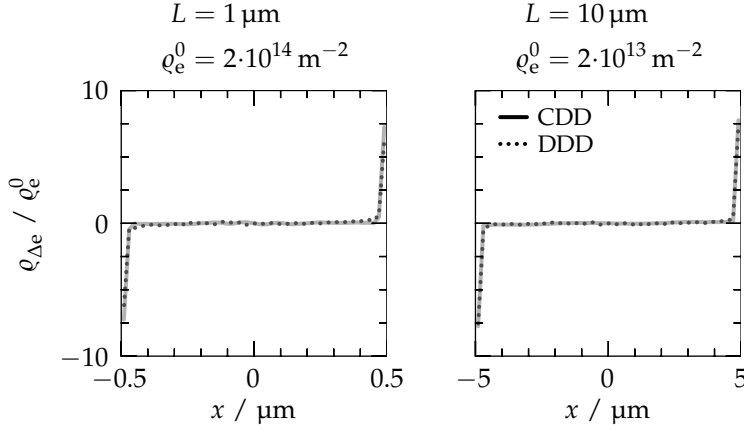


Figure 6.11: Excess dislocation density along the equator of the two kinematically equivalent circular inclusions of size $L = 1$ and $10 \mu\text{m}$ at an applied stress of $\tau_{\text{ext}} = 100 \text{ MPa}$. Solid lines show the results of the CDD simulations, dotted lines those of the DDD simulations.

6.4.2 Discussion

Two systems (with a random population of dislocations) behave identically if both geometric and kinematic invariance are fulfilled. Then, the two systems not only contain the same number of dislocations N and have the same plastic capacity γ_{max} , but as a consequence, also the ratio of BURGERS vector length to inclusion size L has to be equal for both systems. Yet, if both the BURGERS vector and the positions of the dislocations are equally scaled, then the stress field is identical.¹²

$$\sigma_{xy}^i = \sum_{j=1, j \neq i}^N \frac{\mu_L^b}{2\pi(1-\nu)} \frac{\left(\frac{x^i}{L} - \frac{x^j}{L}\right) \left(\left(\frac{x^i}{L} - \frac{x^j}{L}\right)^2 - \left(\frac{y^i}{L} - \frac{y^j}{L}\right)^2 \right)}{\left(\left(\frac{x^i}{L} - \frac{x^j}{L}\right)^2 + \left(\frac{y^i}{L} - \frac{y^j}{L}\right)^2 \right)^2} \quad (6.17)$$

However, since the BURGERS vector is a material constant, either geometric or kinematic invariance but not both can be achieved for the same material parameters.

So, the two kinematically equivalent inclusions of 1 and $10 \mu\text{m}$ look overall very similar, but not exactly the same in the DDD (see second and third columns in fig. 6.8). The smaller inclusion reveals a weak, yet recognizable, boundary layer while none is visible for the larger inclusion. The fact that in the CDD there is no boundary layer for both inclusion sizes indicates that the effect is related to the discreteness of the dislocations.

Figure 6.12 explains the effect for a wall of edge dislocations, which is very similar to what one finds in the circular inclusion except for the curvature of the wall. In the first row of fig. 6.12 the stress field

¹² For simplicity, the equation for the shear stress field given here only considers positive edge dislocations. The same holds for dislocations of screw or negative edge type.

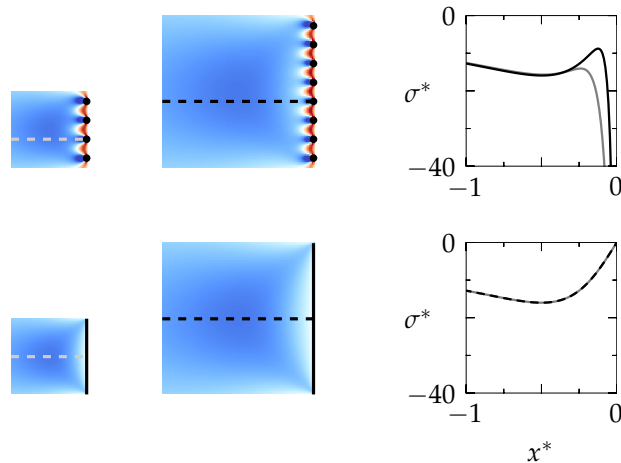


Figure 6.12: Stress field of two edge dislocation walls of different height l but same dislocation spacing h . The upper row shows the stress field of discrete dislocations, the lower row the continuum stress field. The graphs in the third column plot the stress along the dashed lines of the maps (gray: small wall, black: large wall); both stress and space coordinate are used in dimensionless form, so $\sigma^* = \sigma h / (\mu b) / (2\pi(1 - \nu))$ and $x^* = x/l$.

in front of two walls of different height l , but with same spacing of the dislocations h is shown. This corresponds to two kinematically equivalent inclusions of different size. Three observations are important here:

1. The stress field in front of the wall can be subdivided into a short-range stress field close to the wall, which reflects the frequency of the dislocation spacing h , and a long-range stress field further away that is very uniform.
2. The long-range stress field of the wall scales with the wall height l , *i.e.*, it is equivalent with respect to relative space coordinates $(x^*, y^*) = (x/l, y/l)$.
3. The short-range stress field close to the wall does not scale relative to the wall height, but has a constant thickness of about one dislocation spacing h , which reflects the equal spacing of the dislocations in the two walls.

As a consequence of the latter two observations, the short-range stress field has a larger *relative* size for the smaller setup. This is visualized in the graph in the third column of fig. 6.12, which plots the stress along the dashed lines in the maps.¹³

In a continuum description, a dislocation wall is represented by a wall of continuously distributed density. Compared to the stress field of the discrete dislocations, a corresponding stress field of a wall of continuously distributed density does not reveal an equivalent short-range stress.¹⁴ Hence, the stress field of the two linearly scaled pileups is identical with respect to relative coordinates (see second row of fig. 6.12). Compared to the discrete wall, the stress field smoothly decays to zero when advancing the wall.

Turning again to the circular inclusions, this means that in the continuum description the dislocation density can easily propagate up to the wall independent of the size of the inclusion. In the discrete description, however, dislocations “feel” an additional stress when getting close to the walls. This stress is repelling if the advancing dislocation moves on (nearly) the same slip plane (see

¹³ The relative y positions of the dashed lines in the maps is not exactly equal. The positions were chosen such that they correspond to a position of a dislocation in the wall. The difference in the position leads to slight mismatch of the long-range stress, which is, however, almost not recognizable.

¹⁴ A. Roy, R.H.J. Peerlings, M.G.D. Geers, and Y. Kasyanyuk. Continuum modeling of dislocation interactions: Why discreteness matters? *Materials Science and Engineering: A*, 486(1-2): 653–661, 2008. ISSN 0921-5093. DOI: 10.1016/j.msea.2007.09.074

graph in the first row and third column of fig. 6.12), so that those dislocations will tend to reach their equilibrium position in some short distance from the wall. Since the short-range stress field depends on the slip plane spacing, it does not change for kinematically equivalent inclusions of randomly distributed dislocations with the same average slip plane spacing h defined as

$$h = \frac{L}{N} = \frac{4}{\pi \rho_e^0 L}. \quad (6.18)$$

As a consequence, in the DDD, the influence of the short-range stress field grows for decreasing size of kinematically equivalent inclusions and leads to the small boundary layer seen in the left graph of fig. 6.10. In other words, for a small inclusion, the discrete spacing between dislocations on the wall becomes apparent while for larger inclusions the wall appears more and more smooth and resembles the continuum solution. However, the effect is comparably small here, since the start configurations of the dislocations in the DDD simulation are given by a random distribution of positions inside the plastic inclusion. For such a random distribution the probability of dislocations to have exactly the same slip plane is relatively low. Hence, also the probability of forming pileup configurations that would lead to larger boundary layers is low. This is also in agreement with work of Groma et al. [2003], who showed that, if one relaxes a system of randomly distributed dislocations, the pair-correlation functions for dislocations decay within only a few dislocation spacings, *i.e.*, dislocations do not form strong pileups. Under an applied shear stress this effect will become even stronger, since dislocations can more easily pass each other.

In a sense, a random distribution of dislocations is the closest configuration to a continuous (and homogeneous) dislocation density. In fact, one can think of a homogeneous dislocation density as a random distribution of infinitesimal small BURGERS vectors. Thus, the CDD model is a limiting case of the random distribution of dislocations that was used for the DDD.

Although the assumption of a random distribution of dislocations is useful to compare with continuum results, it might be far from the situation in a real crystal, where dislocations are emitted in pairs from dislocation sources. Hence, the next section will focus on the effect of correlated dislocation positions in the start configuration of the DDD simulation.

6.5 Influence of dislocation correlation

In order to study the effect of correlated dislocation positions, an increasing degree of order is introduced in the start configurations of the DDD simulations. This means that the dislocation positions are not anymore completely random. Instead, dislocations are inserted pairwise, *i.e.*, one positive and one negative dislocation, at

a (still random) position in the inclusion that can be thought of as a dislocation source. The number of dislocation pairs that are emitted by such a single dislocation source is denoted multiplicity m . The multiplicity of the dislocation sources is controlled, since it determines the degree of correlation or order in the system.¹⁵ The number of dislocations that are on average emitted by a dislocation source does not change the dislocation content of the system, since the total dislocation density is kept constant. Only the distribution of the dislocation positions is changed.

The number of dislocation sources N_{source} is determined by

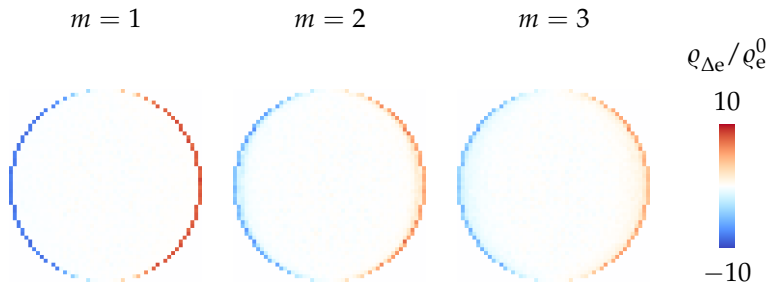
$$N_{\text{source}} = \frac{N}{2m} = \frac{\pi q_e^0 L^2}{8m}. \quad (6.19)$$

Then, a change in the number of dislocation sources does not influence any of the identified characteristic length scales of the system except for the average slip plane spacing h , which can be defined (in contrast to eq. (6.18)) as

$$h = \frac{L}{N_{\text{source}}} = \frac{8m}{\pi q_e^0 L}. \quad (6.20)$$

6.5.1 DDD Results

The most apparent change of the inclusion's plastic response in the DDD simulations is the formation of a significant boundary layer. As shown in fig. 6.13, this boundary layer is not yet visible for a multiplicity of the dislocation sources of $m = 1$. For this setup, the behavior is very similar to a random configuration of dislocations: more or less the entire monopolar dislocation density is pushed to the walls. Already for a multiplicity of $m = 2$, the excess dislocation density directly at the wall has decreased significantly. Instead, a boundary layer is formed with a smooth increase in excess density towards the wall. This boundary layer extends further for multiplicity $m = 3$, while the height of the dislocation pileup at the wall shrinks.



¹⁵ The number of dislocation pairs that is emitted by a dislocation source is controlled only in an average manner. To a certain extent, dislocation sources are allowed to deviate from the multiplicity m as long as the average value for m per simulation is maintained.

Figure 6.13: Excess dislocation density distribution in a circular inclusions of size $L = 1 \mu\text{m}$ with a dislocation density of $q_e^0 = 2 \cdot 10^{14} \text{m}^{-2}$ and at an applied stress of $\tau_{\text{ext}} = 100 \text{MPa}$. From left to right the degree of order in the start configuration of the DDD increases from one to three pairs of dislocations per source.

6.5.2 Phenomenological backstress in CDD

While the degree of correlation or order can be directly controlled in the DDD simulations, this is not easily possible for the CDD simulations, if one does not want to resolve the initial heterogeneity

of the dislocation structure. Thus, a backstress term is introduced in order to phenomenologically capture the effect of the dislocation pileup seen in the DDD results (fig. 6.13). The chosen formulation for the backstress is based on similar expressions as proposed by Groma et al.¹⁶ and Evers.¹⁷ Groma et al. [2003] derive their expression of a backstress directly from statistical averaging of the equations of motions of the discrete dislocations. During this averaging procedure a characteristic length scale has to be introduced, which is chosen as the mean dislocation spacing $1/\sqrt{\bar{\rho}}$. This results in an expression for the backstress that scales with the spatial gradient of the excess dislocation density and with the inverse of the total dislocation density.

$$\tau_b^{\text{Groma}} = -\frac{D\mu b}{2\pi(1-\nu)} \frac{\text{grad}_s \varrho_{\Delta e}}{\varrho_e} \quad (6.21)$$

where D is a scalar constant. Although based on somewhat different arguments, the backstress term in Evers [2003] looks very similar.

$$\tau_b^{\text{Bayley}} = -\frac{\mu b R^2}{8(1-\nu)} \text{grad}_s \varrho_{\Delta e} \quad (6.22)$$

They derive this expression by integration of a linear gradient in the excess dislocation density over a circular area with radius R , where R is treated as a fitting parameter.

Here, the formulation of Groma et al. [2003] is adopted, however, with a different characteristic length scale than the mean dislocation spacing, which would clearly fail to predict the different results as shown in fig. 6.13, since the mean dislocation spacing is actually independent of the correlation and in particular the same for all three simulation results in fig. 6.13. Instead, the average slip plane spacing is assumed to be the decisive characteristic length. Thus, the backstress term is formulated as

$$\tau_b = \frac{\mu b \tilde{h}^2}{2\pi(1-\nu)} \text{grad}_s \varrho_{\Delta e} \quad (6.23)$$

with \tilde{h} as an effective slip plane spacing, which linearly relates to the average slip plane spacing h by a phenomenological fitting parameter chosen here to be equal to $1/2$.

$$\tilde{h} = \frac{1}{2}h \quad (6.24)$$

Figure 6.14 compares results obtained by the modified CDD model with a nonlocal backstress and the DDD results for the three values of the multiplicity m . While the excess dislocation density matches almost perfectly for all three cases, the plastic shear is slightly too low for the CDD model compared to the DDD results. Nonetheless, the growing boundary layer in the shear distribution is still well predicted.

¹⁶ I. Groma, F.F. Csikor, and M. Zaiser. Spatial correlations and higher-order gradient terms in a continuum description of dislocation dynamics. *Acta Materialia*, 51(5):1271–1281, 2003. ISSN 1359-6454. DOI: 10.1016/S1359-6454(02)00517-7

¹⁷ L.P. Evers. *Strain Gradient Crystal Plasticity based on Dislocation Densities*. PhD thesis, Technische Universiteit Eindhoven, 2003

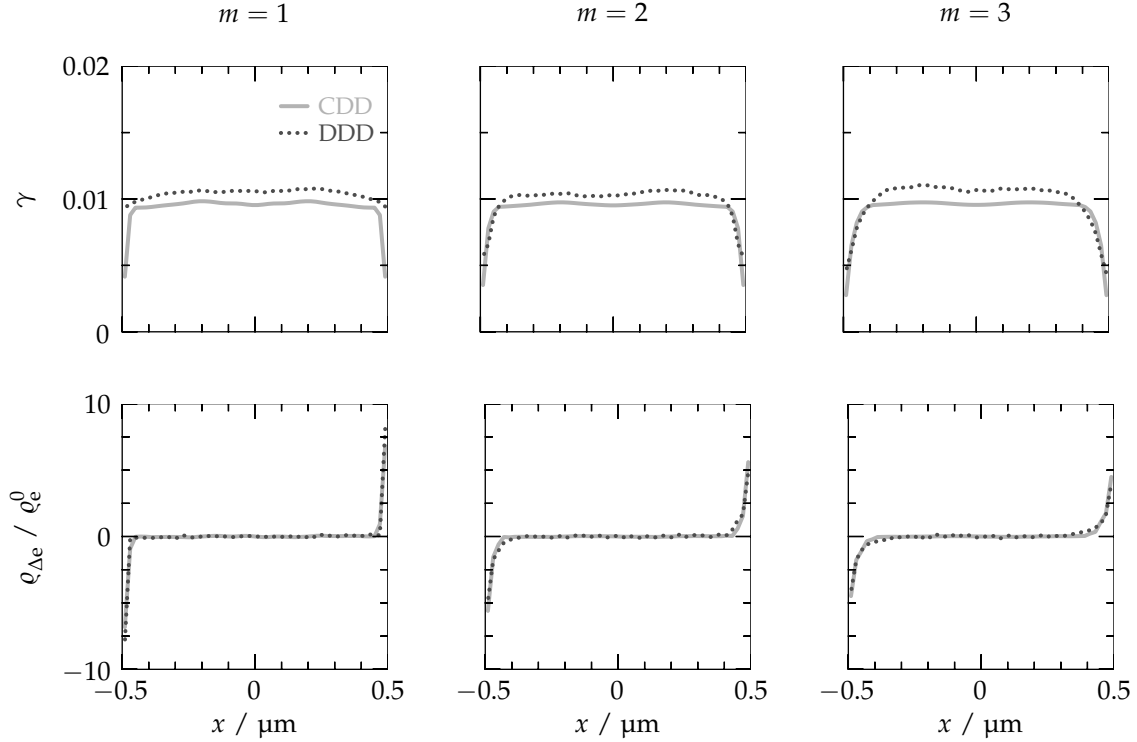


Figure 6.14: Plastic shear and excess dislocation density along the equator of a circular inclusion of size $L = 1 \mu\text{m}$ with a dislocation density of $\rho_e^0 = 2 \cdot 10^{14} \text{m}^{-2}$ and at an applied stress of $\tau_{\text{ext}} = 100 \text{MPa}$. Solid lines show the results of the CDD simulations, dotted lines those of the DDD simulations. From left to right the degree of order in the start configuration of the DDD increases from one to three pairs of dislocations per source; the corresponding CDD simulations include a backstress that depends on the average slip plane spacing h .

6.5.3 Discussion

A distinct boundary layer evolves in the DDD simulations with increasing slip plane spacing, which can be modeled in the CDD by a backstress term that is scaled by the slip plane spacing. Yet, the average plastic shear of the inclusion is only very little influenced by the evolving boundary layer. Figure 6.15 shows the average plastic shear in the inclusion for random start configuration and for one, two, and three pairs of dislocations per dislocation source. From a random configuration to a multiplicity of $m = 1$ the average plastic shear increases slightly by approximately 5%. For higher multiplicities $m = 2$ and 3 the plastic shear decreases again approximately by 2% each. This rather weak influence of the boundary layer on the global mechanical response can be explained as follows.

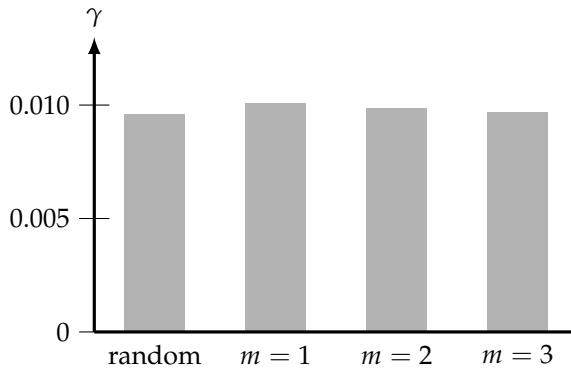


Figure 6.15: Average plastic shear γ of a circular inclusion of size $L = 1 \mu\text{m}$ with dislocation content $\rho_e^0 = 2 \cdot 10^{14} \text{m}^{-2}$ and at an applied stress of $\tau_{\text{ext}} = 100 \text{MPa}$ as obtained from DDD simulations. From left to right the degree of order in the start configuration of the DDD increases from completely random to one, two, and three pairs of dislocations per dislocation source.

The increased slip plane spacing does not only lead to a stronger

backstress, hence a larger pileup. It also influences the formation of dislocation dipoles. As shown in fig. 6.16, from a random distribution of dislocations to a correlation of $m = 3$ the dipolar dislocation density $\rho_{e\pm}$ in the DDD simulations shrinks from a random configuration to multiplicity $m = 3$ by almost 40%. The larger spacing between the slip planes obviously leads to a lower probability for two dislocations of opposite sign passing each other at sufficiently close distance. A lower formation rate of dislocation dipoles entails a higher density of mobile dislocations. Thus, the impeded dislocation slip near the boundary is almost compensated by an increased strain in the center of the inclusion (compare first row of fig. 6.14). Since this effect is not captured in the CDD model, the dipolar dislocation density here remains almost constant; and the plastic shear is consequently lower compared to the DDD.

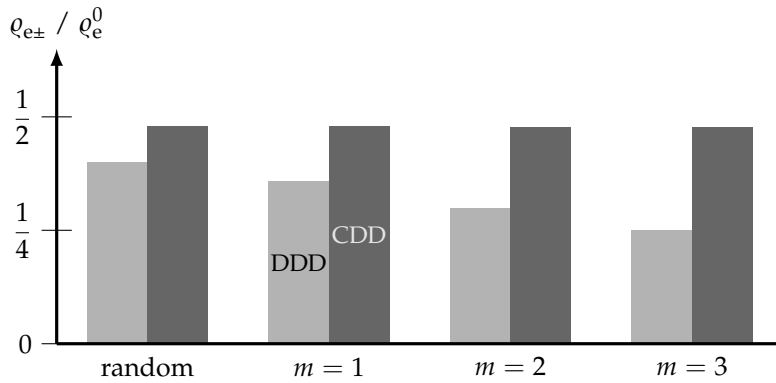


Figure 6.16: Dipole dislocation density $\rho_{e\pm}$ of a plastic inclusion of size $L = 1 \mu\text{m}$ with dislocation content $\rho_e^0 = 2 \cdot 10^{14} \text{m}^{-2}$ and at an applied stress of $\tau_{\text{ext}} = 100 \text{MPa}$ as obtained from DDD and CDD simulations. From left to right the degree of order in the start configuration of the DDD increases from completely random to three pairs of dislocations per source; the corresponding CDD simulations include either no backstress (random) or a backstress that depends on the average slip plane spacing h (for $m \geq 1$).

One could argue that the effect of the backstress increases nonlinearly with the slip plane spacing and will be decisive for larger numbers of dislocations per source. However, for the present inclusion, an average number of three dislocation pairs per slip plane was the maximum which still resulted in a stable configuration.¹⁸ Although a *single* linear pileup would be able to contain up to seven dislocation pairs, multiple simultaneously operating dislocation sources emit less dislocations, since the (back)stress mutually exerted from the other pileups leads to an earlier shut down. In a real crystal, this can partly be compensated by activation of additional dislocation sources in between the ones that have already shut down. In this respect, the fixed number of dislocation sources in the present simulations rather lead to an amplification of the boundary layer effect.

Moreover, despite the fact that the influence of correlated dislocation positions generated significant boundary layers, it did not alter the overall plastic response to a large extent as is usually implied by the presence of dislocation pileups. Hence, for the following simulations, the influence of the discrete slip plane spacing will not be taken into account. Eventually, the only important size effect that could unmistakably be observed, is the trivial exhaustion of mobile carrier density for plastic slip by either locking or accumulation at the boundary.

¹⁸ Simulations for larger inclusions of size $L = 10 \mu\text{m}$ showed to be able to contain up to 20 dislocation pairs per slip plane. The relative size of the boundary layer with respect to the inclusion is, however, even smaller.

6.6 Conclusions

A comparative study between DDD simulations of the present nonlocal CDD model was carried out for a two-dimensional representation of an ESHELBY type inclusion inside an elastic medium. The inclusion deformed by single-slip of dislocations of pure edge character. Dislocation multiplication and annihilation was disregarded here. The following conclusions can be drawn from this comparison.

- The continuum model is able to match the discrete dislocation dynamics results to a large extent. A careful treatment of the dislocation transport is a natural prerequisite for this good agreement. Clearly, any local approach would fail to predict the redistribution of dislocation density and accumulation at the walls.
- Despite the multiple reactions involved in the formation and dissociation of dislocation dipoles, a straightforward model of dipole formation in the CDD is able to reproduce most of the effects seen in the DDD simulations. Especially the densities of dipolar dislocations in the CDD and DDD simulations match.
- A local flowstress based on the dislocation density of the own slip system leads to oscillations in the solution when used in combination with the transport of dislocations. These (mesh-dependent) oscillations are not seen in the DDD simulation results. They develop due to an instability in the governing partial differential equations that is introduced by the flowstress term.
- A geometrically invariant change of the system is obtained when both the inclusion size and all dislocation positions are equally scaled at a fixed number of dislocations. Then, the mechanical response remains unchanged as long as the maximum attainable shear is not reached. Beyond this limit the provided plastic deformation depends on the product of dislocation density and inclusion size.
- A kinematically invariant change of the system is obtained when the inclusion size scales inversely proportional to the dislocation density. Then, the maximum plastic shear, hence the plastic response of the system as the product of density and size, remains unchanged.
- No significant boundary layer is visible in the DDD simulations if the dislocations are randomly distributed in the plastic inclusion. This corresponds to the implicitly made assumption of a homogeneous dislocation density in the CDD.
- If the dislocations are pairwise distributed in the DDD simulations, a significant boundary layer can arise. This is

attributed to the concentration of slip on specific slip planes and the resulting formation of pileups. The boundary layer grows in extent if the number of active slip planes is reduced at constant overall dislocation content.

- The boundary layer effect can be reproduced by the CDD model if a nonlocal backstress term is introduced that depends on the spacing of the slip planes.
- An increased slip plane spacing also leads to a reduction in dipolar dislocation density. This leads to an increased strain in the center of the inclusion, which partly compensates the reduced strain at the walls due to the boundary layer.
- As a consequence, the overall plastic response of the inclusion does not change much if the slip plane spacing is increased.
- For the following simulations, the backstress term is considered insignificant and therefore neglected.

Simple shear of an Aluminum bi-crystal with a small angle tilt grain boundary

The deformation of poly-crystals fundamentally differs from that of single-crystal material. The reason for that stems from the inherent anisotropy of plastic deformation caused by the discrete nature of available modes of lattice deformation. In fcc metals, *e.g.*, the conservative motion of dislocations that leads to slip is bound to the $\{111\}$ lattice planes. In a poly-crystal, the lattice orientation changes from grain to grain. Thus, at the interface between two grains, *i.e.*, the grain boundary, the lattice planes for dislocation glide usually do not match—the grain boundary impedes dislocation motion across it.^{1,2}

Here, the focus is set on the effect of a small-angle grain boundary. Small-angle boundaries are of special interest, because the relatively low orientation difference of the adjacent grains results in minor differences in the single-crystal behavior of the grains. Thus, the effect of the grain boundary is not superimposed by a large difference in the Schmid factors of the grains and becomes visible more clearly.

An existing shear experiment of an aluminum bi-crystal is chosen in order to study the effect of the nonlocal dislocation flux with respect to a grain boundary.³ The available experimental data comprises surface strain maps obtained by means of digital image correlation (DIC) and force measurements by means of a load cell. The chosen experimental reference has already been simulated in an earlier work by Ma,⁴ who employed a nonlocal model that is not based on the redistribution of dislocation density but on additional kinematical constraints at the grain boundary. The results of the two different approaches will be compared.

7.1 Problem setup

The sample used in the experiments is a $3.1 \times 17.0 \times 2.0 \text{ mm}^3$ aluminum bi-crystal of 99.999 wt% purity with a planar grain boundary normal to the y direction as shown in fig. 7.1.

Orientations of the upper and lower grain are $\varphi_1 = 264.7^\circ$, $\phi = 32.2^\circ$, $\varphi_2 = 44.3^\circ$ and $\varphi_1 = 277.0^\circ$, $\phi = 32.2^\circ$, $\varphi_2 = 37.4^\circ$

¹ M.D. Sangid, T. Ezaz, H. Sehitoglu, and I.M. Robertson. Energy of slip transmission and nucleation at grain boundaries. *Acta Materialia*, 59(1): 283–296, 2011. ISSN 1359-6454. DOI: 10.1016/j.actamat.2010.09.032

² B. Liu, D. Raabe, P. Eisenlohr, F. Roters, A. Arsenlis, and G. Hommes. Dislocation interactions and low-angle grain boundary strengthening. *Acta Materialia*, 59(19):7125–7134, 2011. ISSN 1359-6454. DOI: 10.1016/j.actamat.2011.07.067

³ J.C. Kuo. *Mikrostrukturmechanik von Bikristallen mit Kippkorngrenzen*. PhD thesis, RWTH Aachen, 2004

⁴ A. Ma. *Modeling the constitutive behavior of polycrystalline metals based on dislocation mechanisms*. PhD thesis, RWTH Aachen, 2006

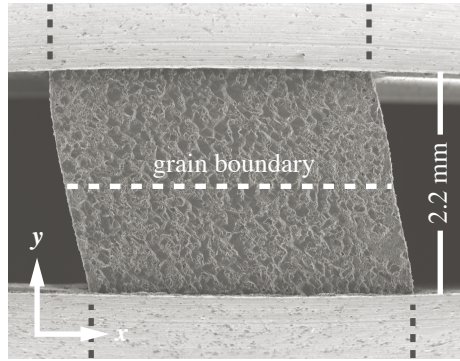


Figure 7.1: Aluminum bi-crystal in simple shear.

expressed in Bunge⁵ notation. This orientation relationship induces a 7.4° symmetric tilt boundary with rotation axis in $[112]$ crystal direction, which is perpendicular to the x - y image plane of fig. 7.1. The tall bi-crystal is clamped normal to the z direction and sheared parallel to the grain boundary with a constant shear rate of $\dot{\gamma} = \dot{\gamma}_{xy} = -4.5 \cdot 10^{-4} \text{ s}^{-1}$ up to a final (technical) shear of almost $-\gamma_{xy}^{\text{tec}} = 0.6$ (see [Kuo, 2004] for details). Local deformation of the sample surface was captured in the area of $3.1 \times 2.2 \text{ mm}^2$ visible in fig. 7.1 after shear increments of $4.5 \cdot 10^{-2}$ using DIC.

⁵ H.J. Bunge. *Texture Analysis in Materials Science*. Butterworths, London, 1982

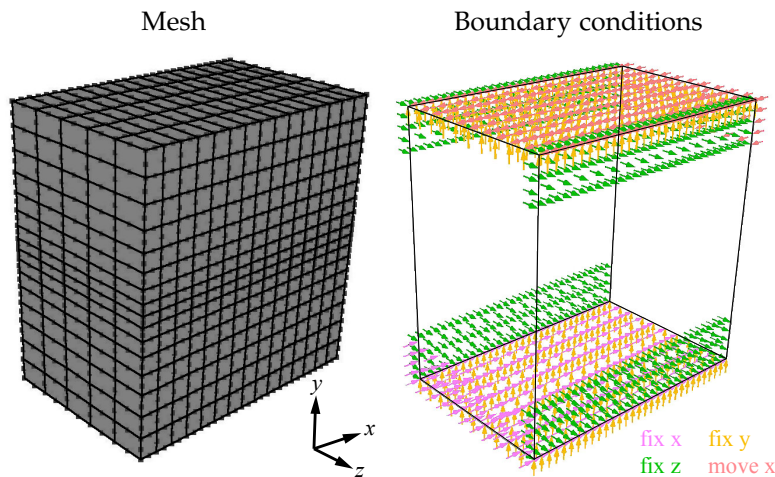
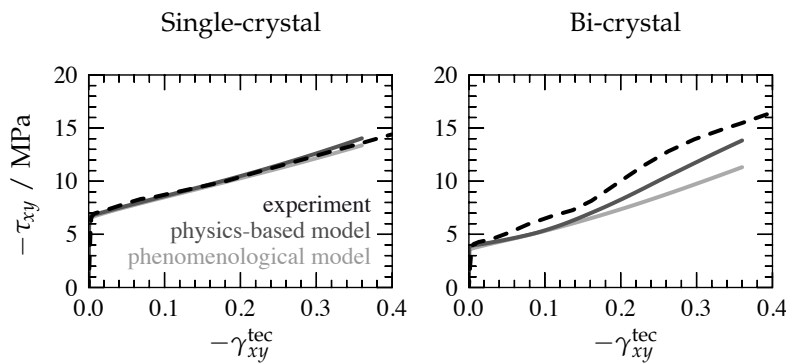


Figure 7.2: Mesh and boundary conditions of the model used for the finite element simulations.

For the simulations the sample geometry is meshed by $16 \times 15 \times 5$ quadratic finite elements of reduced integration capacity with decreasing element size towards the grain boundary (see fig. 7.2). The uppermost and lowest two levels of elements mainly serve as support in order to achieve realistic boundary conditions. The fixation of the nodes in z direction mimics the clamping of the sample. Owing to the fact that this clamping does not hold perfectly and that the sample is slightly pulled out of the clamp in the experiment, only part of these nodes are fixed in x and y direction. The model is deformed in simple shear by means of a linearly increasing displacement in x direction that is applied to the top surface nodes and the nodes that touch the clamp on the right side of the sample in fig. 7.1.

The bi-crystal deformation is simulated by means of four different

models: a standard phenomenological model following Rice⁶ and Hutchinson,⁷ and three different variants of the constitutive model that is presented in this work. The first variant does not consider any flux of dislocations, which renders the model purely local, although it is still based on dislocation mechanics. The second variant includes dislocation flux with a transmissivity set to $\chi = 1.0$ to reflect the assumption of perfect slip transfer at the low-angle grain boundary. Finally, the third variant also includes flux, but sets the transmissivity to $\chi = 0.0$ at the grain boundary, so that no dislocation can cross the boundary between the two crystals.



⁶J.R. Rice. Inelastic constitutive relations for solids: an internal variable theory and its application to metal plasticity. *J. Mech. Phys. Solids*, 19: 433–455, 1971

⁷J.W. Hutchinson. Bounds and Self-Consistent Estimates for Creep of Polycrystalline Materials. *Proceedings of the Royal Society A: Mathematical, Physical and Engineering Sciences*, 348: 101–127, 1976

Figure 7.3: Stress strain curve of an aluminum single-crystal (left) and bi-crystal (right) under simple shear. The single-crystal curve is used for fitting of the material parameters, the bi-crystal curve for validation. Experimental data (dashed lines) is taken from Kuo [2004].

A stress–strain curve of a single-crystal simple shear experiment of the same material as the bi-crystal is used to fit the material parameters (table 7.1 and fig. 7.3).⁸

7.2 Results

In addition to the single-crystal results used for parameter fitting, fig. 7.3 also shows the stress-strain response of the bi-crystal. All four simulations predict a lower stress response than measured in the experiment (dashed line). Yet, there is a difference between the phenomenological and the dislocation-based model. While the phenomenological model predicts an almost constant hardening, the dislocation-based model shows a clearly increasing hardening after a shear of about 0.15, which is also visible in the experimental data. In general, the stress response of the physics-based model is closer to the experiment than the phenomenological model. There is virtually no difference in the stress-strain curve of the three variants of the physics-based model.

Figure 7.4 compares the von Mises strain distribution at different levels of deformation between experiment and simulation. The strain deformation pattern obtained in the experiment unambiguously reflects the bi-crystal character of the sample: high deformation in the interior of the grains and a zone with noticeably less shear around the horizontal grain boundary. This partitioning of strain between the upper and lower grain is well captured by the physics-based model, as well as the main locations and directions of

⁸F. Roters, Y.W. Wang, J.C. Kuo, and D. Raabe. Comparison of single crystal simple shear deformation experiments with crystal plasticity finite element simulations. *Adv. Eng. Mater.*, 6(8):653–656, 2004. DOI: 10.1002/adem.200400079

Property		Value	Unit
cubic elasticity constants	C_{11}	106.75	GPa
	C_{12}	60.41	GPa
	C_{44}	28.34	GPa
isotropic shear modulus	μ	26.27	GPa
Poisson ratio	ν	0.345	
length of Burgers vector	b	0.286	nm
atomic volume	Ω	0.017	nm ³
minimum edge dipole separation	\check{d}_e	1.6	nm
minimum screw dipole separation	\check{d}_s	10	nm
dislocation multiplication constant	λ_0	60	
edge contribution to multiplication	k_1	0.1	
initial overall dislocation density	ρ_0	$6 \cdot 10^{10}$	m ⁻²
self-diffusivity (at $T = 300$ K)	D_{SD}	$7 \cdot 10^{-29}$	m ² s ⁻¹
solid-solution activation energy	Q_S	1.25	eV
solid-solution concentration	c_{at}	$1.5 \cdot 10^{-6}$	
solid-solution size	d_{obst}	0.572	nm
Peierls stress	τ_P	0.1	MPa
double kink width	w_k	2.86	nm
energy barrier profile constants	p	1	
	q	1	
attack frequency	ν_a	50	GHz
dislocation viscosity	η	0.01	Pa s
edge jog formation factor	k_3	1	

Table 7.1: Material parameters used to simulate simple shear of the aluminum bi-crystal

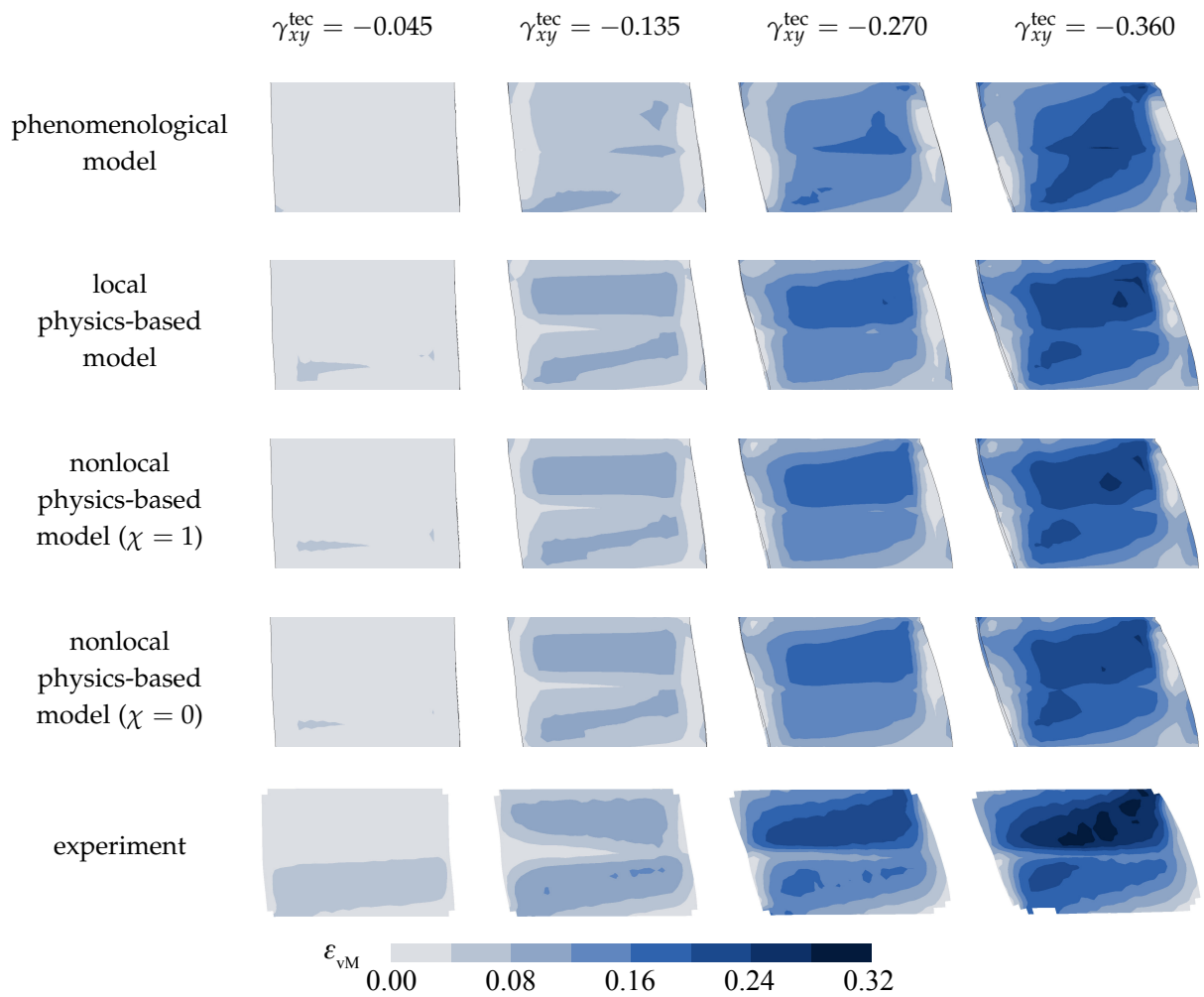


Figure 7.4: Surface maps of von Mises logarithmic strain for an aluminum bi-crystal with small-angle grain boundary at different levels of simple shear. Experimental data taken from Kuo [2004].

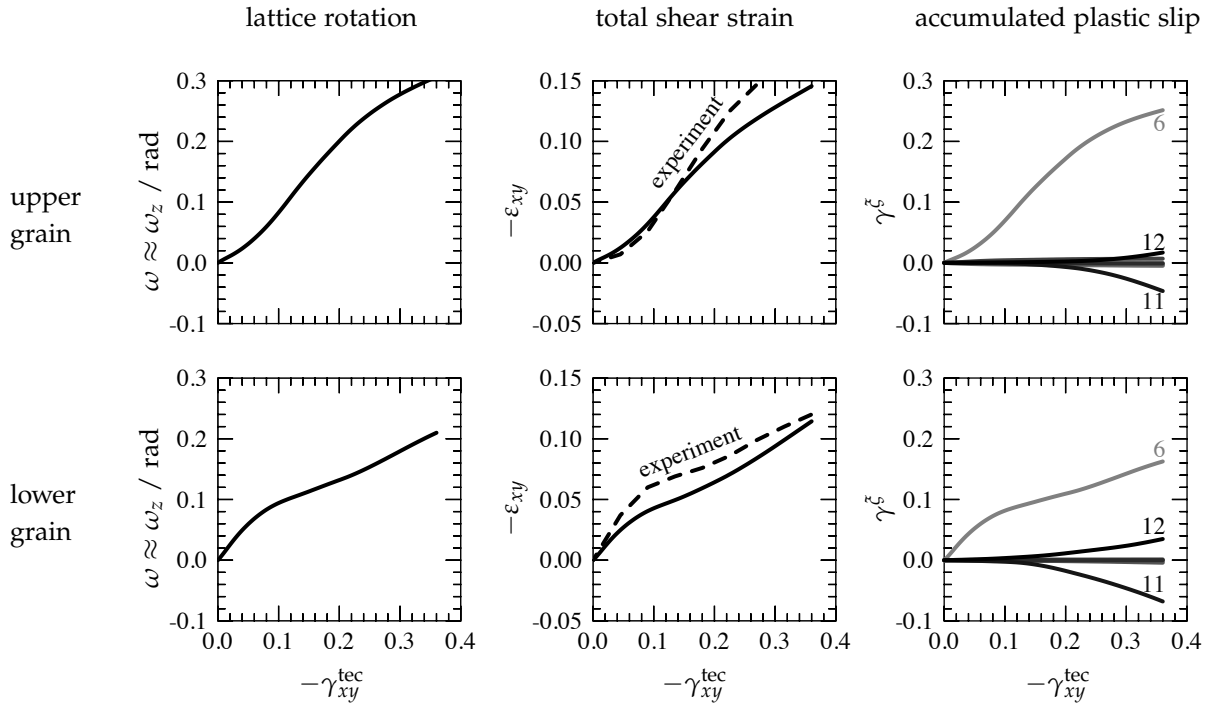


Figure 7.5: Evolution of the mean shear stress ϵ_{xy} , the mean crystal rotation ω , and the mean accumulated plastic shear γ per slip slip system for the upper and the lower grain in the bi-crystal for the physics-based model with flux and zero transmissivity at the grain boundary. Slip systems are indicated by numbers next two the graph.

the shear gradients, although the contrast between grain interior and grain boundary is not as high in the simulations as in the experiment. The three variants of the physics-based model reveal only slight differences in the strain distribution. The phenomenological model is not able to reproduce the partitioning of strains with the zone of reduced strain around the grain boundary.

A more quantitative evaluation of the deformation evolution is given in fig. 7.5 for the nonlocal model with zero transmissivity at the boundary. The figure shows the evolution of the lattice rotation, the total shear strain (with experimental data as dashed line), and the accumulated plastic slip as a function of the applied shear and separated for the upper and lower grain. In both experiment and simulation the lower grain initially carries virtually all the deformation until plastic slip in the upper grain is activated and eventually takes over the deformation. The evolution of the accumulated plastic slip in the rightmost column of fig. 7.5 shows that both grains initially exhibit single glide on the same slip system 6. This slip system is (initially) oriented such that the slip plane normal points into negative x direction and the BURGERS vector into y direction (see fig. 7.6), thus the slip plane lies orthogonal to the grain boundary. Due to the symmetry of the stress state, this slip system reveals a high theoretical Schmid factor although the resulting dislocation slip does not correspond to the externally applied displacement and leads to a shear deformation perpendicular to it. As a consequence, a lattice rotation around the z axis of nearly the same amount is needed to compensate for the

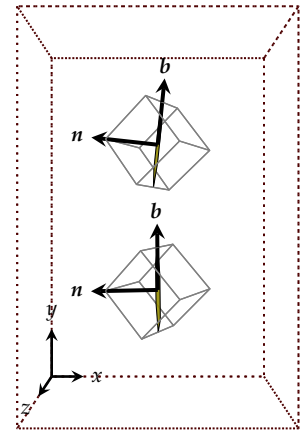


Figure 7.6: Initial lattice orientation in upper and lower grain of the bi-crystal with slip direction b and slip plane normal n of slip system 6.

given boundary conditions (see first column in fig. 7.5). At about $\gamma_{xy}^{\text{tec}} = -0.2$ secondary slip systems start to contribute while the primary (number 6) stays predominant.

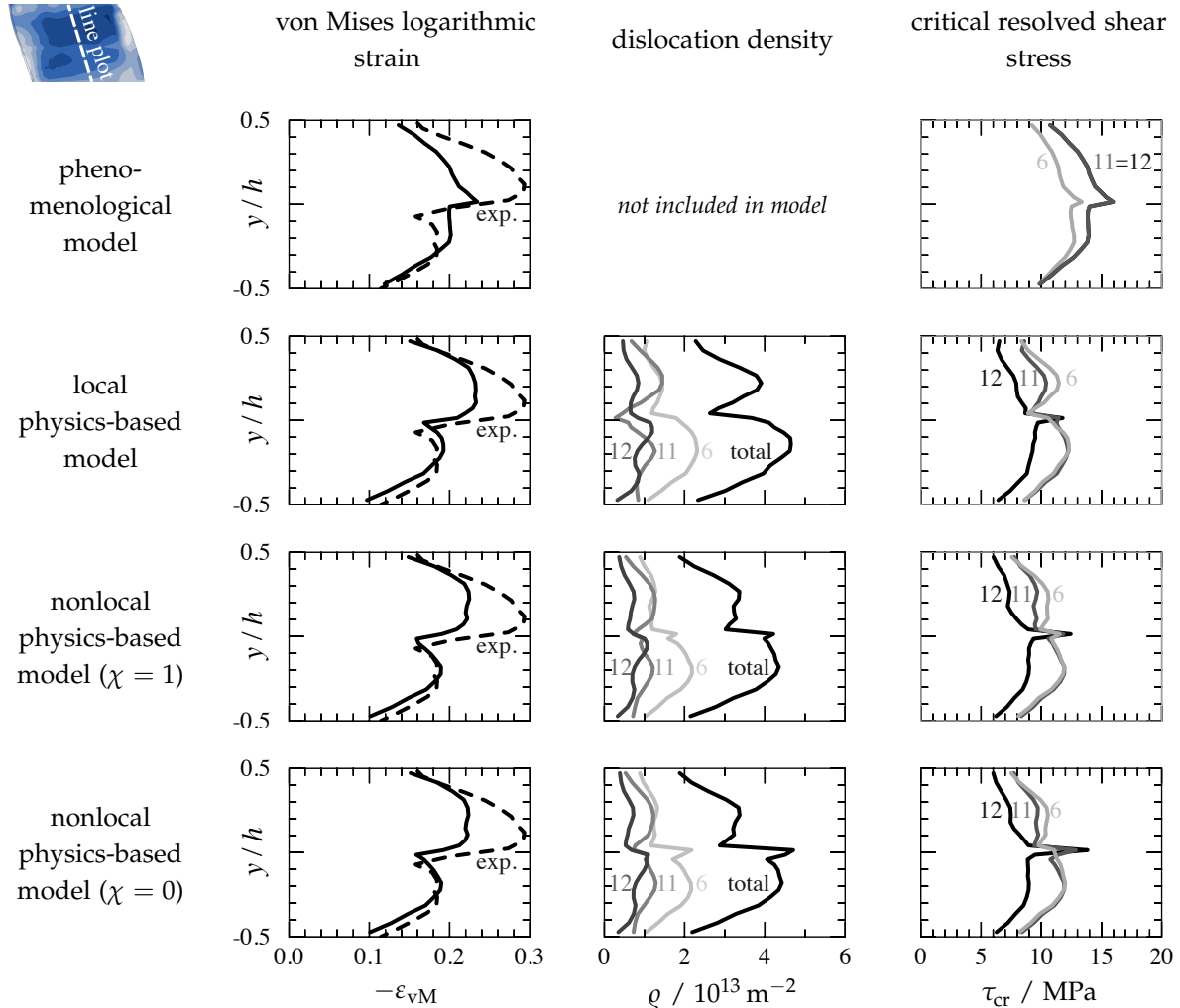


Figure 7.7 shows line plots of the strain profile along the y direction across the grain boundary. The experimentally observed zone of reduced deformation (last row of strain maps in fig. 7.4) appears as a sharp minimum in the strain profile (dashed line). This cusp is also present in the physics-based simulation results but not for the phenomenological model where, in contrast, the strain has a maximum at the grain boundary. For the two nonlocal models with fluxes of dislocations one observes a slightly stronger dip in the strain at the grain boundary than for the local model variant. The second column of fig. 7.7 shows line plots of the total dislocation density and the density on the mainly active slip systems 6, 11, and 12.⁹ For all three variants of the physics-based model one finds local maxima of the dislocation density in the grain interior that correspond to the maxima of the strain profiles in the first column. The local variant of the model reveals a sharp minimum of dislocation density directly above the grain boundary

Figure 7.7: Profiles of the von Mises logarithmic strain ε_{eq} , the total dislocation density ρ and the critical resolved shear stress τ_{cr} on the mainly active slip systems 6, 11 and 12. The line profiles are taken orthogonal to the grain boundary in y -direction at a shear deformation of $\gamma_{xy}^{\text{tec}} = -0.36$. Dashed lines in the total shear strain profiles show experimental data taken from Kuo [2004].

⁹ Since the phenomenological model does not have the dislocation density as an internal state variable, there are no results shown for this model.

in the upper grain, while for the two nonlocal variants this minimum is not as pronounced. As a result of the dislocation redistribution in the nonlocal model variants, dislocation density accumulates in front of the boundary, especially on slip system 6. This dislocation pileup is more pronounced for the nonlocal model with no transmission at the boundary than for the fully transmissive boundary.

The third column of fig. 7.7 shows line plots of the critical resolved shear stress τ_{cr} on slip systems 6, 11 and 12. The phenomenological model reveals a strong link between the critical resolved shear stress and the von Mises strain: both profiles follow the same trend with a slight maximum at the boundary. For the physics-based model the critical stress is significantly smaller due to the completely different kinematics.¹⁰ The three model variants have a very similar critical stress in the grain interior, but differ at the grain boundary: the nonlocal variant with no dislocation transmission at the boundary reveals a strong increase of the critical resolved shear stress for slip systems 11 and 12 at the boundary, while the increase is less pronounced for the other two variants; the mainly active slip system 6 faces the highest resistance to dislocation glide in the nonlocal simulation with complete transmission at the boundary.

¹⁰ In fact, the meaning of the critical resolved shear stress differs in both models: in the present physics-based model this stress constitutes the mechanical limit below which no dislocation motion is possible. In the phenomenological model this stress rather plays the role of an effective parameter that controls plastic deformation; so plastic slip is also possible below the critical stress in the phenomenological model.

7.3 Discussion

The specific orientation of the bi-crystal with respect to the applied deformation gives rise to a deformation mode that is rather unexpected for a simple shear experiment: the main dislocation activity entails motion of dislocations perpendicular to the applied shear deformation—and perpendicular to the grain boundary. This particularity leads to a pileup of dislocations towards the grain boundary in the simulations for the nonlocal model with transmissivity equal to zero (see second column of fig. 7.7), while the pileup is less pronounced in the simulation with transmissive boundary, and not visible in the local model without any dislocation flux. However, this does not lead to a noticeable difference in the global stress response (see fig. 7.3) and does not significantly alter the distribution of strains in the bi-crystal (see rows two to four in fig. 7.4). Only in the strain line plots across the grain boundary (first column of fig. 7.7) one can observe that both nonlocal models are slightly less compliant directly at the grain boundary than the local model; however, the effect amounts only to about five percent compared to the local model.

The reason for the strain at the grain boundary not being affected much can be understood from the specific mode of deformation of the bi-crystal. As shown in fig. 7.5, the deformation of the two crystals is dominated by single-glide on slip system 6 up to a total shear of ten to fifteen percent (depending on the specific grain) until two secondary slip systems 11 and 12 start to produce plastic

strain. This is also reflected by the stress strain curve of the bi-crystal in fig. 7.3, which for both (physics-based) simulation and experiment shows an increasing hardening at about fifteen percent when the predominant slip system 6 becomes less favorable for plastic glide due to strong lattice rotation and the secondary slip systems 11 and 12 become active in both crystals (see fig. 7.5). Consequently, at that point the interaction of the now three slip systems leads to a faster growing critical resolved shear stress (CRSS).

More interesting than the global behavior of the individual slip systems is the local behavior, especially at the grain boundary, where one does not observe a strong influence of the dislocation transport and transmissivity on the strain. Looking at the line plot across the CRSS on the three mainly active slip systems (third column of fig. 7.7) is helpful in this respect. While both nonlocal models reveal higher values for the CRSS on slip systems 11 and 12 than for the local model, the difference for slip system 6 is not very pronounced, although exactly this system is decisive for the total deformation and creates strong pileups at the grain boundary. The reason that slip system 6 does not significantly increase its slip resistance is related to the way the CRSS is designed: there is no direct self-interaction of the dislocation density with the same slip system (see table 3.4). In the present model a slip system can only self-harden indirectly by creation of edge-jogs via annihilation of screw dipoles (see section 3.2.6). Much more effectively, any dislocation activity on different slip planes increases the slip resistance. This is the case for slip systems 11 and 12, which do not share the slip plane with system 6, hence feel the strong dislocation pileup on 6 in terms of additional Lomer and Hirth locks, respectively. In contrast, slip system 6 does not face any significant hardening due to pileups on other slip systems. *E.g.*, slip systems 11 and 12 do not form pileups at the boundary, since their orientation is such that the slip plane lies almost parallel to the grain boundary. So the transport and pileup of dislocations towards/at the boundary does not remarkably alter the strain response.

Ma [2006] also reports an increased hardening of the grain boundary, although he does not quantify the effect. It can be presumed that the effect will be larger for two reasons. Firstly, the CRSS in Ma [2006] considers also self-hardening. This can in particular lead to an increased hardening of the mainly active slip system 6 due to the strong pileup at the boundary. The second more obvious reason is the explicit additional hardening that Ma [2006] introduces at the grain boundary by an increase in the activation energy of plastic slip. He argues that dislocations can only cross the grain boundary—and produce slip—if misfit dislocations at the boundary balance out the orientation change of the lattice of the two adjacent grains; the formation of these misfit dislocations required an additional amount of energy, hence the

increased activation energy for slip. However, the increased hardening is reasoned by an implied pileup of GNDs at the boundary. The results of the present model indicate that this effect is actually rather weak, or at least confined to a very small region that does not influence the overall strain behavior significantly. In the experiment, one can clearly perceive a zone of reduced deformation around the grain boundary (see fig. 7.4). This zone can be reproduced by all three variants of the physics-based model, yet not for the phenomenological model. The fact that already the local variant of the physics-based model captures the effect of the grain boundary gives further evidence that—in this example—the accumulation of dislocation density at the grain boundary is not decisive for the plastic response. Instead, the intricate dependency of dislocation slip on the lattice orientation and the boundary conditions seems to be more important here. Given that the kinematics of dislocation slip for the individual grains is properly described, the solution of mechanical equilibrium in a compatible continuum already suffices to correctly predict the influence of the grain boundary.¹¹ The less sophisticated phenomenological model does obviously not provide a sufficient description of the kinematics and, hence, fails to predict the influence of the grain boundary.

¹¹ This might, however, change for smaller grain sizes when dislocation slip is more confined and dislocation pileups gain influence.

7.4 Conclusions

The simple shear deformation of an Aluminum bi-crystal with small angle tilt grain boundary has been simulated and compared to an experimental reference. The following conclusions can be drawn:

- The plastic deformation of the bi-crystal is almost exclusively generated by dislocation glide on a slip system that initially is oriented with BURGERS vector perpendicular to the direction of the prescribed shear displacement; so dislocation slip is almost perpendicular to the shape change of the sample. This entails large lattice rotations in order to accomplish the prescribed simple shear deformation.
- In agreement with experiments, the physics-based model predicts an increase in the hardening behavior at about 20 % strain. This correlates with the change from single-glide to multiple-glide in the simulation, hence is attributed to stronger cross-hardening. The phenomenological model does not predict this change in the hardening behavior.
- Due to the fact the mainly active slip system generates slip (initially) almost perpendicular to the grain boundary, dislocation density accumulates at the grain boundary in the nonlocal model variants that include dislocation transport. Although this leads to a slightly increased hardening at the

boundary, it does not significantly alter the strain response compared to the local (non-flux) model variant.

- A distinct reduction in strain around the grain boundary, which is observed in the experiment, is predicted by both the local and nonlocal physics-based models, however, not for the phenomenological model. While the failure of the phenomenological model is in agreement with Ma [2006], the behavior of the physics-based model is reasoned differently here. Ma [2006] relates the proper behavior of his physics-based model to its nonlocal hardening properties. In contrast, the present results indicate that indeed a correct description of the kinematic hardening suffices.
- The influence of the redistribution of dislocation density by transport of dislocations did not influence the plastic response significantly. The change of the grain boundary transmissivity from transmissive to blocking resulted in a different distribution of dislocation density, but did not significantly affect the strain response.
- For large grain sizes as in this example and given a sufficient number of dislocation sources, the effect of the dislocation flux on the constitutive response can presumably be neglected.

Indentation of single-crystalline nickel with a wedge indenter

The indentation of metals is widely used for material characterization and the derivation of mechanical properties. Although the deformation process follows in principle a simple setup, the boundary conditions and kinematics involved are highly complex. Hence, a thorough understanding of the underlying physics especially with respect to the plastic deformation is of high importance.

One reason for the complexity of the deformation state is its strong variation both in space and time. Since the load of the indenter is locally applied, high gradients in the stress, strain and rotation field naturally arise. As *e.g.* demonstrated by Zaafarani¹ for a sphero-conical indenter, the loading of the material under the indenter ever changes with increasing indentation depth and induces a rapid change of the activated slip systems with space and time.

Variations in the plastic deformation also lead to a heterogeneous distribution of the dislocation content: regions of high plastic slip activity naturally contain more dislocation content than low deformation regions. This relation between slip—hence slipped area—and statistically stored dislocation density (SSD density) can well be described by a local dislocation-based constitutive model by means of the OROWAN equation. If all dislocation loops are statistically equally distributed within and between the slip systems, then on average the signed character of the single dislocation segments counterbalance and the ensemble of dislocations appears neutral. A gradient in plastic slip activity, however, gives rise to an imbalance of dislocation segments of positive and negative character, thus an excess of signed dislocation density, also called geometrically necessary dislocation density (GND density).^{2,3} It is these GNDs that are needed to explain the presence of gradients in the rotation field. However, they cannot directly be predicted by any local constitutive law, since their origin is inherently nonlocal.

For that reason, the present nonlocal constitutive model will be employed to an existing reference of an indentation experiment,

¹ N. Zaafarani. *Experimental and theoretical investigation of nanoindentation in a Cu-single crystal*. PhD thesis, RWTH Aachen, 2008

² E. Kröner. *Kontinuumstheorie der Versetzungen und Eigenspannungen*, volume 5 of *Ergebnisse der angewandten Mathematik*. Springer, Berlin, 1958

³ M.F. Ashby. The deformation of plastically non-homogeneous materials. *Philosophical Magazine*, 21(170):399–424, 1970. DOI: 10.1080/14786437008238426

which allows to directly compare model predictions with the experimental findings.

8.1 Problem setup

An elegant wedge indentation study published by Kysar et al.⁴ (see also Kysar et al. [2007] for earlier studies on copper and aluminum) is used as a suited reference example for comparing simulations with experiment. In this experimental work, pure single-crystalline face-centered cubic Nickel was indented by a 90° wedge indenter to an indentation depth of about 200 μm. The indent was placed into a (001) oriented surface; the indenter axis was aligned parallel to the [110] lattice direction (see fig. 8.1). On the basis of work by Rice,⁵ Kysar et al. [2010] suggest that these specific loading conditions lead to a plane strain deformation state accomplished by the collective activation of certain slip systems. After indentation, the sample was cut in half normal to the wedge indent and the exposed surface was analyzed by electron backscatter diffraction (EBSD).

⁴J.W. Kysar, Y. Saito, M.S. Oztop, D. Lee, and W.T. Huh. Experimental lower bounds on geometrically necessary dislocation density. *International Journal of Plasticity*, 26(8): 1097–1123, 2010. ISSN 0749-6419. DOI: 10.1016/j.ijplas.2010.03.009

⁵J.R. Rice. Tensile Crack Tip Fields in Elastic-Ideally Plastic Crystals. *Mechanics of Materials*, 6:317–335, 1987

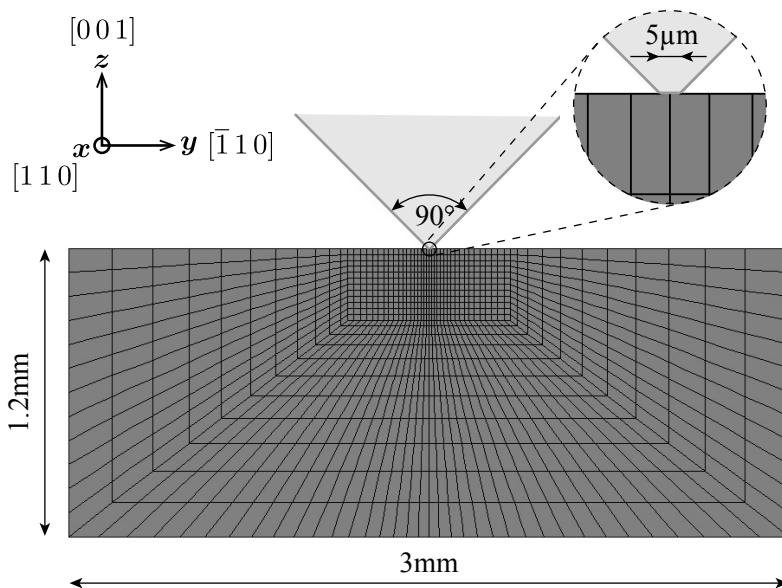


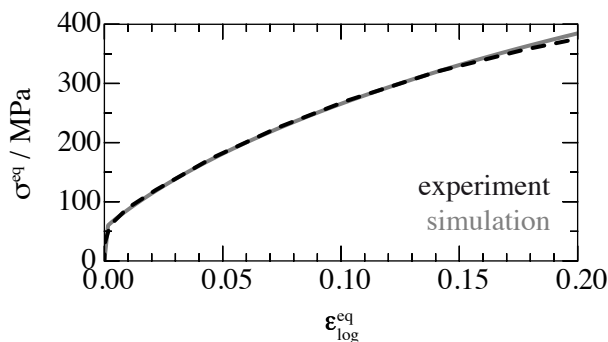
Figure 8.1: FE mesh used for the simulation of wedge indentation. The indenter is modeled by two flat surfaces that have an inclination angle of 90° and a flat tip of 5 μm width.

The experiment is modeled by a finite element simulation with a planar mesh of 1092 hexahedral elements with quadratic interpolation functions and reduced integration capacity as shown in fig. 8.1. Except for the indented surface, all nodes on outer surfaces of the model were constrained to in-plane motion, *i.e.*, no displacement normal to the respective surface was allowed. In particular, displacement in direction of the wedge indent was constrained to be zero on the front and back surface in fig. 8.1 in order to mimic plane-strain conditions. Due to the plane-strain conditions only one mesh element is used in depth. The lateral extent of the FE mesh does not cover the complete sample domain (which was approximately $1 \times 1 \times 1 \text{ cm}^3$), but is chosen sufficiently

large for the boundaries to not influence the predictions. The wedge indenter was modeled by two rigid surfaces that draw an angle of 90° and a flat tip surface of $5\ \mu\text{m}$ width (see blow-up in fig. 8.1). The exact shape of the indenter tip does, however, not play an important role as long as the tip geometry is smaller than the minimum distance between nodes, since in the simulation contact is evaluated only at and not in between nodes. Contact conditions between the indenter and material surface were modeled by Coulomb friction with a friction coefficient of 0.3.⁶

The sample coordinate system is chosen such that the indentation proceeds in negative z direction and the indenter axis is parallel to the x direction. This implies an orientation of the single-crystal of $\varphi_1 = 315^\circ$, $\phi = 0^\circ$, $\varphi_2 = 0^\circ$ expressed in Bunge⁷ notation, such that in the reference configuration the $[1\ 1\ 0]$ direction corresponds to the x axis, $[\bar{1}\ 1\ 0]$ direction to the y axis and the $[001]$ direction to the z axis, respectively.

Elastic constants of Nickel are taken from Hirth and Lothe.⁸ An experimentally obtained value for the minimum dipole separation distance \check{d}_e is taken from Tippelt et al. [1997].⁹ The self diffusivity of Nickel at room temperature was calculated on the basis of material parameters from Gottstein;¹⁰ yet, the self diffusivity at room temperature is small enough so that dislocation climb can be neglected. All other material parameters have to be fitted to experimental data, but have clear physical bounds. Apart from a force-displacement measurement of the actual indentation experiment, Kysar et al. [2010] do not provide further material characteristics of the sample. Therefore, data from uniaxial tensile tests of highly pure poly-crystalline Nickel taken from Keller et al.¹¹ were used to fit the material parameters of the model. The stress-strain curves of both experiment and fitting simulation can be seen in fig. 8.2. A list of all material parameters is given in table 8.1.



⁶ The friction conditions in the experiment are not known to the author. However, the influence of the friction coefficient on the simulation results was found to be rather small.

⁷ H.J. Bunge. *Texture Analysis in Materials Science*. Butterworths, London, 1982

⁸ J.P. Hirth and J. Lothe. *Theory of dislocations*. John Wiley & Sons, New York, 1982

⁹ B. Tippelt, J. Breitschneider, and P. Hähner. The Dislocation Microstructure of Cyclically Deformed Nickel Single Crystals at Different Temperatures. *physica status solidi (a)*, 163(1):11–26, 1997. ISSN 0031-8965. DOI: 10.1002/1521-396X(199709)163:1<11::AID-PSSA11>3.0.CO;2-X

¹⁰ G. Gottstein. *Physikalische Grundlagen der Materialkunde*. Springer, Berlin, 2007

¹¹ C. Keller, E. Hug, and D. Chateigner. On the origin of the stress decrease for nickel polycrystals with few grains across the thickness. *Materials Science and Engineering: A*, 500(1-2):207–215, 2009. ISSN 0921-5093. DOI: 10.1016/j.msea.2008.09.054

Figure 8.2: Stress-strain curve of a tensile test of a poly-crystalline sample. Experimental data was taken from Keller et al. [2009] and used for fitting of the material parameters.

8.2 Results

8.2.1 Lattice rotation

Figure 8.3 juxtaposes the lattice rotation in the yz plane experimentally measured by EBSD (see Kysar et al. [2010] for

Property		Value	Unit	Reference
cubic elasticity constants	C_{11}	246.5	GPa	Hirth and Lothe [1982]
	C_{12}	147.3	GPa	
	C_{44}	124.7	GPa	
isotropic shear modulus	μ	94.66	GPa	Hirth and Lothe [1982]
Poisson ratio	ν	0.277		Hirth and Lothe [1982]
length of Burgers vector	b	0.248	nm	Cordero et al. [2008]
atomic volume	Ω	0.012	nm ³	Cordero et al. [2008]
minimum edge dipole separation	\check{d}_e	2.6	nm	Tippelt et al. [1997]
minimum screw dipole separation	\check{d}_s	12	nm	
dislocation multiplication constant	k_2	45		
edge contribution to multiplication	k_1	0.1		
initial overall dislocation density	ρ_0	$2.88 \cdot 10^{12}$	m ⁻²	
self-diffusivity (at $T = 300$ K)	D_{SD}	$3 \cdot 10^{-53}$	m ² s ⁻¹	Gottstein [2007]
solid-solution activation energy	Q_S	1.12	eV	
solid-solution concentration	c_{at}	$5 \cdot 10^{-7}$		
solid-solution size	d_{obst}	1	b	
Peierls stress	τ_P	0.1	MPa	
double kink width	w_k	10	b	
energy barrier profile constants	p	1		
	q	1		
attack frequency	ν_a	50	GHz	
dislocation viscosity	η	0.001	Pa s	
edge jog formation factor	k_3	0.01		

Table 8.1: Constitutive parameters of single-crystalline Nickel used for a simulation of wedge indentation

details) and the simulated rotation pattern. The experimentally obtained and the simulated rotation maps reveal the same features. In general, the simulation slightly overestimates the rotations compared to the experiment. Regions of high rotation can be found on both flanks of the indent and directly below the tip of the indent. A boundary running vertically down from the indenter tip divides the sample into two halves with symmetric rotation patterns but inverted sign. The out-of-plane rotations were negligibly small both in experiment and simulation.

The observation that the absolute values of the rotations are higher in the simulations compared to the experiments can be explained in terms of the fact that the highest reorientation would be expected to occur close to the interface between indenter and crystal. However, the metallographic preparation required for the EBSD characterization leads to a modest curvature of the sample edges. Hence, the contact area between tool and metal cannot be mapped.

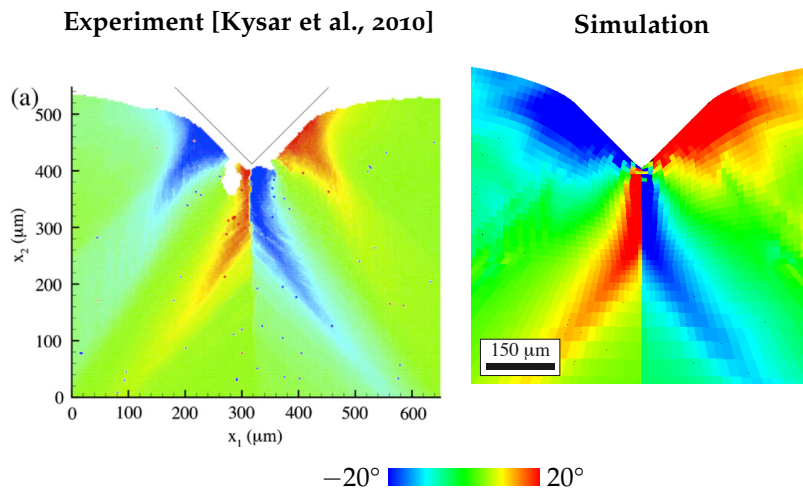


Figure 8.3: In-plane lattice rotation below the wedge indent as obtained from experiment and from simulation.

8.2.2 Strain and stress states

For understanding the material behavior especially with respect to dislocation activity it is helpful to map the strain and stress state below the indenter.

Figure 8.4 shows a map of the von Mises logarithmic strain after unloading. It reveals several distinct regions of concentrated strain and a symmetric distribution with respect to the vertical indentation axis. The highest strains of about 1 occur directly under the indenter tip. Around the tip one observes a triangular region with still comparably high strains around 0.5 that encloses approximately the same area as the actual indent. Within this central region two deformation modes prevail. Directly under the indenter tip the material deforms by compression in z direction and extension in y direction (see right side of fig. 8.4). In the lateral corners of the triangle the material rather deforms by simple shear:

on the right side by a positive deformation gradient in z with respect to y ($F_{zy} > 0$) and on the opposite left side by a negative deformation gradient ($F_{zy} < 0$). Two regions of slightly lower equivalent strain are visible on both sides of the symmetry axis. They have a beam like shape that points away from the symmetry axis at an angle of nearly 45° and extent into the sample to approximately five times the indentation depth. The first region, which is attached to the lower sides of the central triangular region, exhibits the same deformation mode as under the indenter tip: compression in z and extension in y direction. The second region, which starts slightly below the flank of the indent, reveals biaxial strain with extension in z and compression in y direction. In between these strain concentrations, the material stays almost undeformed with $\varepsilon \lesssim 0.1$.

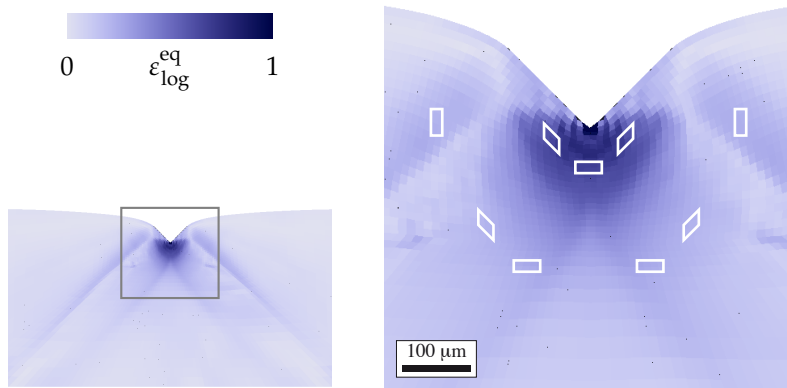


Figure 8.4: Simulated von Mises logarithmic strain distribution with schematic representation of the predominant deformation modes below a wedge indent in single-crystalline Nickel.

Figure 8.5 shows the equivalent CAUCHY stress just before unloading (left) and after unloading (right). In both the loaded and unloaded condition there are mainly two different regimes (however, less pronounced for the unloaded situation). In a circular area of about the indentation depth around the indenter the material faces almost pure hydrostatic pressure. Around this central area of hydrostatic pressure, the stress has uniaxial compressive character. The principal direction of this compressive stress points radially away from the central regime. This means, that on the indentation axis, the compressive stress acts in z direction, *i.e.*, in direction of the evolving boundary, while close to the material surface the principal axis of the stress lies almost parallel to the y axis. The highest stress occurs in between these two positions when the principal stress axis draws a 45° angle with the indentation axis, *i.e.*, is perpendicular to the indenter flanks.

While the highest strain is found in a circular area directly under the indenter, the highest stress values are found around this area. It is just at the edge of these two areas where most of the plastic shear occurs, as will be discussed next.

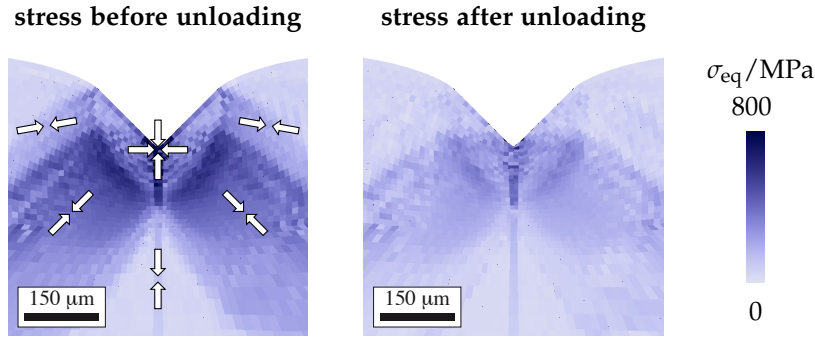


Figure 8.5: Simulated von Mises CAUCHY stress around a wedge indent before and after unloading. Main stress states are indicated by white arrows.

8.2.3 Plastic slip

The deformation of the material under the indenter is accomplished by only six slip systems (table 8.2). All other systems do not significantly contribute to plastic deformation. As shown by Rice¹² and in detail for the current geometry by Kysar et al.,¹³ the six active slip systems form three pairs of “partner” slip systems that cooperatively accomplish a plane strain deformation when subjected to a line load along the $[1\ 1\ 0]$ direction (see appendix A.6). The two collinear slip systems 3 and 6 in combination allow for slip in direction of $[1\ \bar{1}\ 0]$ on an effective slip plane (001) , hence shear in the (110) plane. The two coplanar slip systems 7 and 8 in combination allow for slip in an effective direction $[\bar{1}\ \bar{1}\ 2]$ on the slip plane $(1\ \bar{1}\ \bar{1})$, hence also shear in the (110) plane. Finally, the two coplanar slip systems 10 and 11 in combination allow for slip in an effective direction $[\bar{1}\ 1\ 2]$ on the slip plane $(\bar{1}\ \bar{1}\ \bar{1})$, hence again shear in the (110) plane. All six observed activated slip systems lead to a plane strain deformation in the (110) lattice plane, which is normal to the lab x axis.

The exact distribution of the accumulated plastic slip on the six active slip systems is shown in fig. 8.6. The two “partner” slip systems cover the same regions of activity, but with inverted signs of the accumulated slip due to the symmetric orientation of the two slip systems with respect to the indentation axis. For the slip systems 3 and 6 the opposite orientation of the slip plane normals with respect to the indentation axis entails opposite signs of the resolved shear stress on the slip plane, hence opposite signs of the plastic slip. In case of slip systems 7/8 and 10/11 the opposite orientation of the slip direction with respect to the indenter axis has the same effect. The most striking feature of the maps for slip systems 7/8 and 10/11 is the sharp edge of the slipped volume right below the indenter tip, which is in contrast to the gradual decay in slip activity elsewhere.

Figure 8.7 shows the evolution of the shear rate on two of the active slip systems with increasing indentation depth.¹⁴ On slip system 3, plastic slip starts in two bands, which point away from the surface at a 45° angle. With increasing indentation these micro-bands of concentrated slip become broader, less intense, and move

¹² J.R. Rice. Tensile Crack Tip Fields in Elastic-Ideally Plastic Crystals. *Mechanics of Materials*, 6:317–335, 1987

¹³ J.W. Kysar, Y. Saito, M.S. Oztop, D. Lee, and W.T. Huh. Experimental lower bounds on geometrically necessary dislocation density. *International Journal of Plasticity*, 26(8): 1097–1123, 2010. ISSN 0749-6419. DOI: 10.1016/j.ijplas.2010.03.009

ξ	slip plane	slip direction
1	(111)	$[0\ \bar{1}\ \bar{1}]$
2	(111)	$[\bar{1}\ 0\ 1]$
3	(111)	$[1\ \bar{1}\ 0]$
4	$(\bar{1}\ \bar{1}\ \bar{1})$	$[0\ \bar{1}\ \bar{1}]$
5	$(\bar{1}\ \bar{1}\ \bar{1})$	$[1\ 0\ 1]$
6	$(\bar{1}\ \bar{1}\ \bar{1})$	$[\bar{1}\ 1\ 0]$
7	$(1\ \bar{1}\ \bar{1})$	$[0\ \bar{1}\ \bar{1}]$
8	$(1\ \bar{1}\ \bar{1})$	$[\bar{1}\ 0\ \bar{1}]$
9	$(1\ \bar{1}\ \bar{1})$	$[1\ 1\ 0]$
10	$(\bar{1}\ \bar{1}\ \bar{1})$	$[0\ 1\ 1]$
11	$(\bar{1}\ \bar{1}\ \bar{1})$	$[1\ 0\ \bar{1}]$
12	$(\bar{1}\ \bar{1}\ \bar{1})$	$[\bar{1}\ \bar{1}\ 0]$

Table 8.2: Slip systems for a $[001]$ wedge indent. Active slip systems are typed in black, all others in light gray. Slip system numbering as introduced in table 3.1.

¹⁴ The shearrate on the other active slip systems follows from inversion according to the maps of the accumulated slip in fig. 8.6.

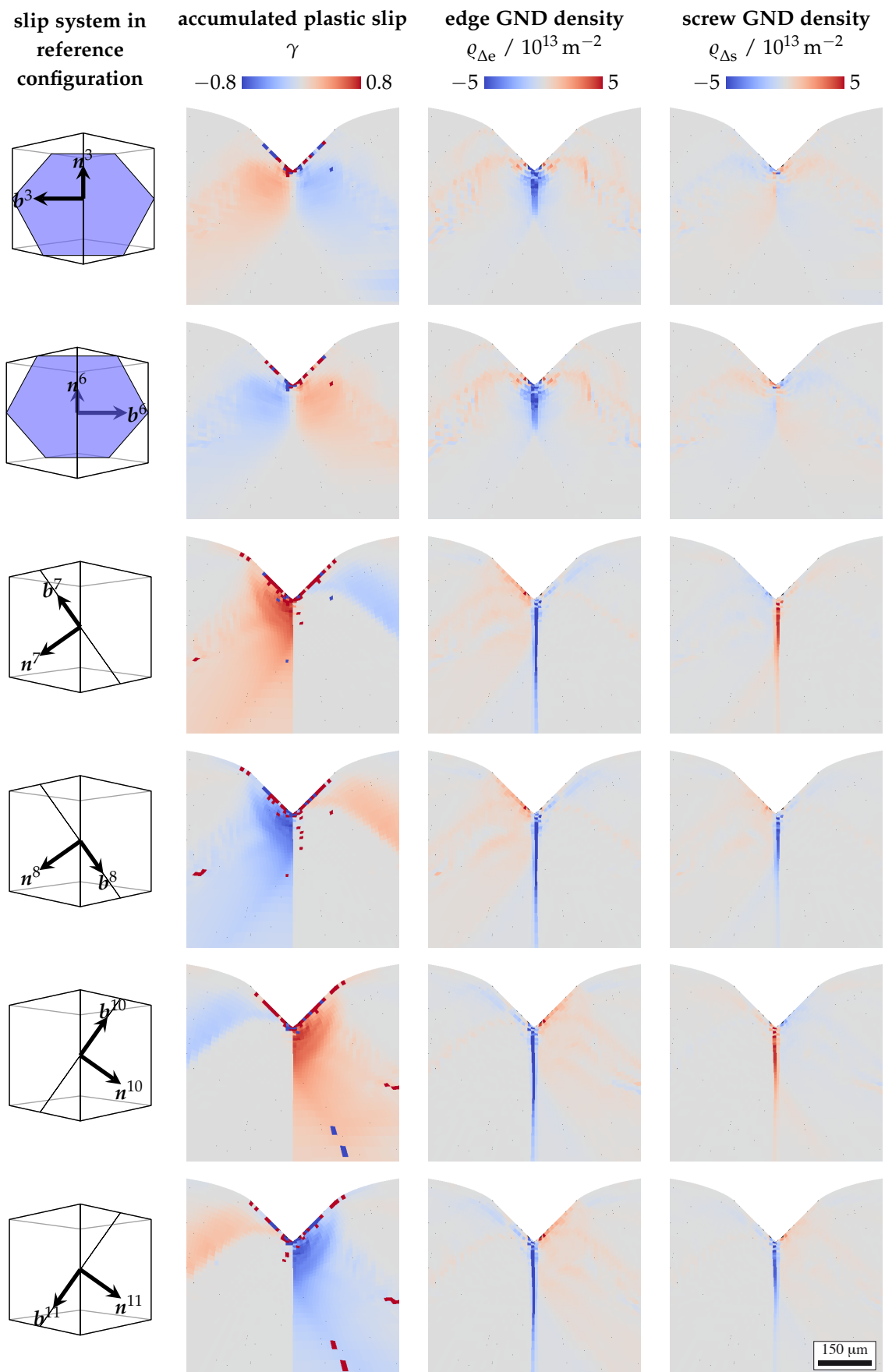
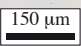


Figure 8.6: Simulated accumulated slip and edge/screw GND density for the six active slip systems below the wedge indent. 

downwards. At the same time, a region of no slip activity expands around the indenter tip. This corresponds to the hydrostatic pressure regime seen in fig. 8.5 that does not provide any resolved shear stress for plastic slip. The slip activity on slip system 11 also starts in two bands of 45° from the surface. Yet, the active regions evolve differently on both sides of the rotation boundary. The red band on the left is moving up while keeping its relative position on the indenter flank. The blue band on the right side splits up into two branches with an inflection point at the boundary that moves down. The upper branch describes an arc towards a stationary point at the same relative position on the indenter flank as where the red band starts at on the left side. With increasing indentation, the arc bows out leaving behind a region of virtually no slip activity similarly to what can be seen for slip system 3. The lower branch of the active region becomes broader to the bottom with increasing indentation and rotates towards the indentation axis.

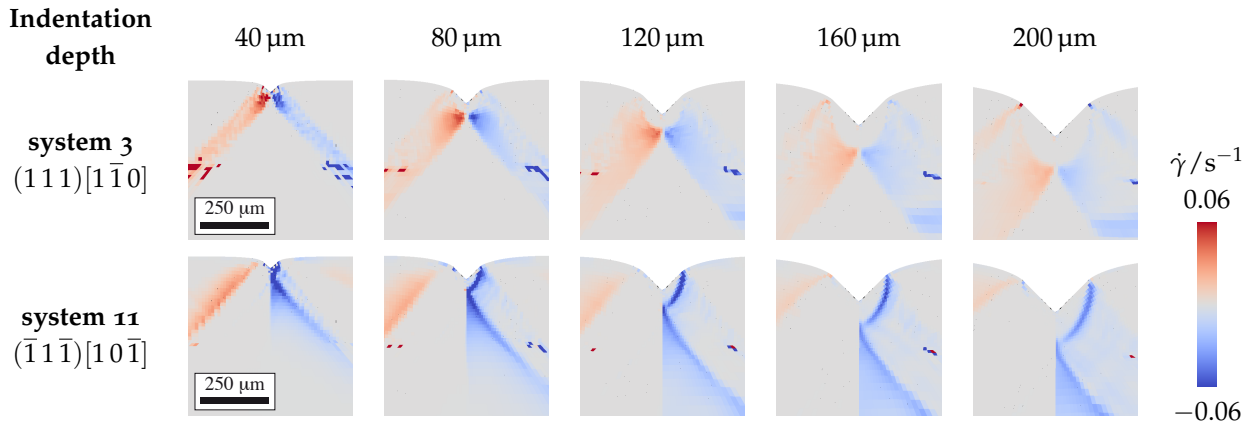


Figure 8.7: Simulated plastic shear rate on slip systems $(111)[1\bar{1}0]$ and $(\bar{1}\bar{1}\bar{1})[10\bar{1}]$ for a wedge indenter of depth 40, 80, 120, 160, and 200 μm .

Plastic slip propagates through the material in inclined or as an arc like front moving away from the indenter tip. The plastic front evolves, since the material is highly pure and initially deficient on dislocations, so the material is initially very soft and plastic slip can readily occur where the stresses reach the critical resolved shear stress. Then, the dislocation density quickly increases, the material hardens and becomes less favorable for plastic deformation leaving behind a region of high dislocation content but no plastic activity.

8.2.4 Dislocation density

Figure 8.8 shows the distribution of the dislocation density summed over all slip systems and dislocation types in terms of total and excess dislocations. Here, the first comprises the sum of *all* dislocations $\sum_{\xi} \sum_c \rho_c^{\xi}$, whereas the latter comprises the L_1 norm of the *excess* dislocations $\sum_{\xi} \sum_c \left| \rho_{\Delta c}^{\xi} \right|$.¹⁵ The highest total dislocation density can be found around the indenter tip (which corresponds to the region of highest deformation seen in fig. 8.4) and in five narrow bands: one around the deformation-induced boundary and four (less pronounced ones) at $\pm 45^\circ$ and $\pm 50^\circ$ from it. The same

¹⁵ Index ξ denotes the slip system, c the dislocation character, namely edge or screw.

pattern can also be found for the excess dislocation density. However, in the tapered bands the excess dislocation density seems not very high, thus the bands mainly contain statistically stored dislocations. In contrast, the band around the deformation-induced boundary is almost as pronounced as for the total density, which means that the boundary mainly consists of geometrically necessary dislocations.

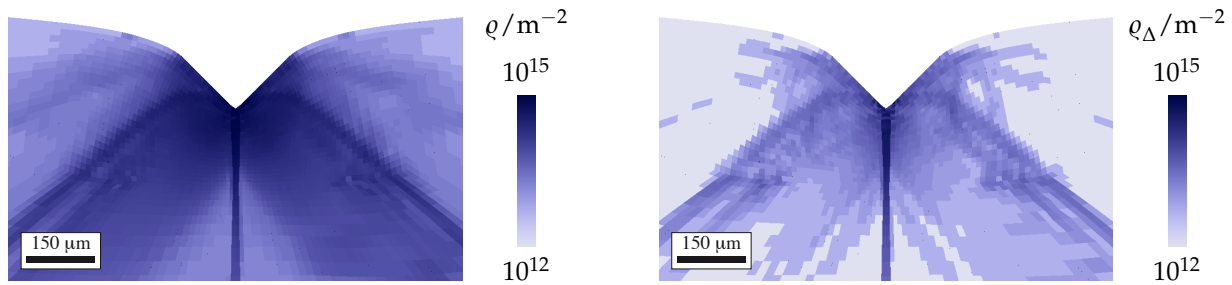


Figure 8.8: Simulated values of total and excess dislocation density under a wedge indent in single-crystalline Nickel. Dislocation densities are summed over slip systems and dislocation types.

8.3 Discussion

The presented case of wedge indentation in single-crystalline Nickel was chosen because of its well defined boundary conditions, the two-dimensional strain mode and the high symmetry orientation, which facilitates the analysis of the obtained results. Yet, the deformation mechanisms occurring in the material still reveal a high complexity and are not restricted to any special case. *E.g.*, all types of considered dislocation interactions, namely collinear junctions, glissile junctions, Hirth locks, and Lomer locks can be found in the material (however, not always all in the same place). Also the deformation state reveals different modes around the indent: biaxial extension/compression in y/z and z/y direction and positive and negative simple shear in z direction.

Deformation state While the compression zone under the indenter and the sheared region at the flanks of the indent can intuitively be understood from the geometrical constraints of the indent, the tensile strains in direction of the indentation axis to the left and right of the indent seem a bit counterintuitive in the first place (see also Bouvier and Needleman¹⁶ who observed tensile strains in indentation simulations). By taking a closer look at the involved slip systems one can, however, better understand this. Figure 8.9 schematically shows the slip traces of slip systems 7 and 8, which are the only active slip systems in this region to accommodate the deformation (compare first row in fig. 8.6). The inclination of the slip plane with respect to the sample system leads to an effective extension in the spatial z and a compression in the spatial y direction. The band-like shape of the strained region then follows from the specific orientation of the slip plane, since slip acts only in direction of the band, which is indeed a broad shear band. These shear bands can expand very easily due to the more or less single

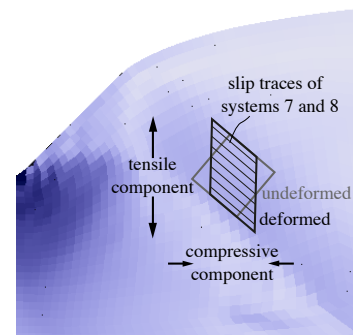


Figure 8.9: Blow-up of fig. 8.4 with a sketch of the deformation that results from active slip systems 7 and 8 in the band-like of increased strain right and left of the indent.

¹⁶S. Bouvier and A. Needleman. Effect of the number and orientation of active slip systems on plane strain single crystal indentation. *Modelling and Simulation in Materials Science and Engineering*, 14(7):1105–1125, 2006. ISSN 0965-0393. DOI: 10.1088/0965-0393/14/7/001

glide behavior. This is the reason for their very long extent of about 1 mm deep into the material compared to the small region of high deformation around the indenter tip, which extends only about 100 to 200 μm .

Active slip systems In order to understand the evolution of lattice rotations and GND densities it is useful to first have a closer look at the evolution of plastic slip on the individual slip systems. As pointed out above, the stress that drives dislocation motion is of almost pure uniaxial compressive nature with the principal axis pointing radially away from a central region of hydrostatic pressure and no slip activity. The highest stress values are found in two regions left and right of the rotation boundary, where the principal stress direction draws a 45° angle with the indentation axis. Figure 8.10 plots an $(00\bar{1})$ inverse pole figure of these two principal directions. Both directions lie on symmetry lines: the compression axis on the left side of the indent on the $[00\bar{1}]-[1\bar{1}\bar{1}]$ and the compression axis on the right side of the indent lies on the $[00\bar{1}]-[\bar{1}1\bar{1}]$ line, respectively. This would normally imply activation of slip systems 2 and 4 on the one side and activation of 1 and 5 on the other. The reason that none of these slip systems is actually active is the plane-strain deformation state that is enforced. As exemplarily shown in appendix A.6 for slip systems 1 and 5, those pairs of slip systems with the highest SCHMID factors induce a normal strain component in x direction, thus out-of-plane. As a result, dislocation glide happens on the “unexpected” slip systems 7/8, 10/11, and 3/6. A positive lattice rotation around the $x=[110]$ direction (or a negative rotation of the principal stress axis) increases the SCHMID factor of systems 10 and 11 on the right side and decreases the SCHMID factor of systems 7 and 8. The opposite holds for inverted rotation sense or on the other side of the indentation axis. Slip systems 3 and 6 initially have their highest possible SCHMID factors with respect to a rotation around the $[110]$ direction for a 45° principal stress axis, so that any change in the lattice orientation or the principal stress axis decreases the SCHMID factor.

Figure 8.11 shows the evolution of the plastic slip on the six active slip systems exemplarily for three points on the right side of the indentation axis. For the point directly next to the boundary (first row), the principal stress direction is almost aligned with the indentation axis. This stress state initially equally favors slip on 7, 8, 10, or 11.¹⁷ However, before the yield point is reached, the lattice has already rotated slightly in negative sense around the $[110]$ axis and continues to do so. As a result, slip on systems 10 and 11 is preferred and dominates the plastic behavior. Only at the end of loading, slip systems 3 and 6 start to become active due to the negative lattice rotations reorienting these slip systems to their preferential orientation. The second point (second row in fig. 8.11) is located in an area of modest lattice rotations of not more than

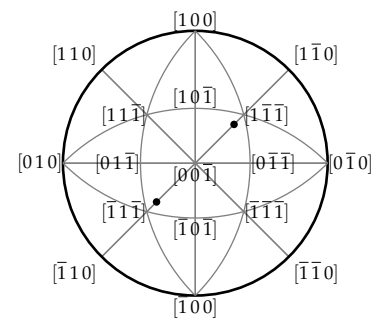


Figure 8.10: $(00\bar{1})$ inverse pole figure of the undeformed crystal with the two principal axes of compressive stress on the left and right side of the indentation axis. The lower left point corresponds to the stress axis on the right side of the indenter, the upper right point to the stress axis on the left side.

¹⁷ Slip systems 1, 2, 4, and 5 that have an equally high SCHMID factor cannot be activated due to the plane-strain deformation mode.

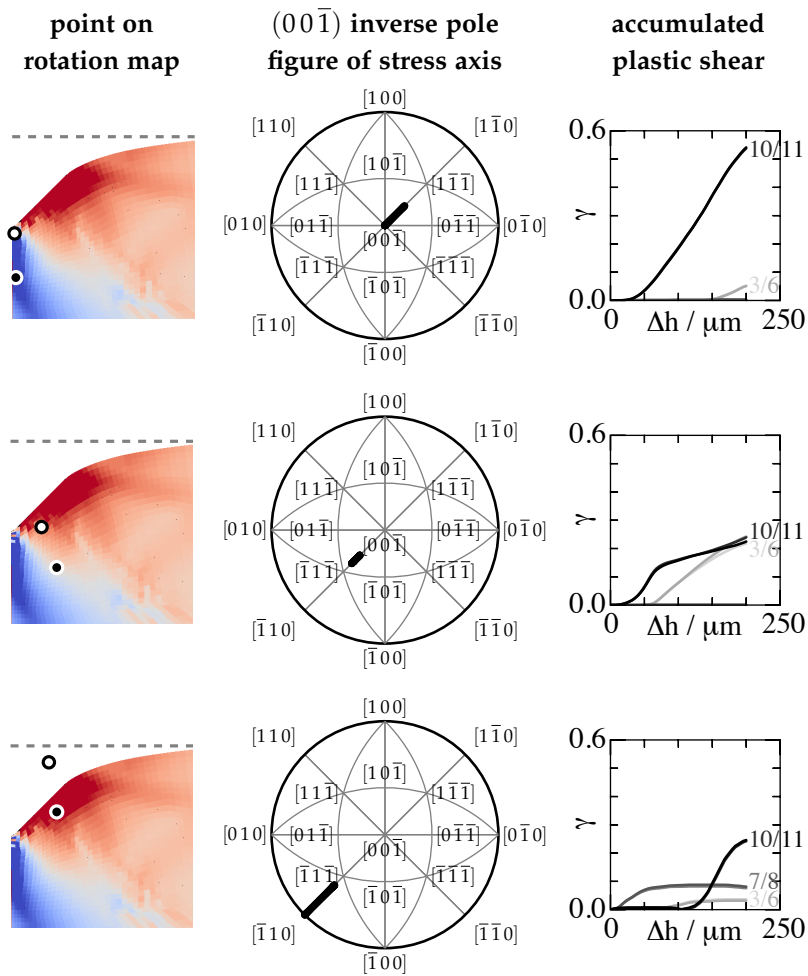


Figure 8.11: Inverse pole figures and evolution of plastic shear with indentation depth Δh for three different material points close to a wedge indenter. Positions of the material points are marked in blowups of fig. 8.12 in the first column (open circles correspond to position before loading, filled circles to positions at end of loading; the initial geometry is indicated by a dashed gray line). The $(00\bar{1})$ inverse pole figures in the second column show the rotation of the principal axis of compressive stress for the respective material points (*i.e.*, in direction of $(y, z) = (0, -1)$ for the first point, $(y, z) = (1, -1)$ for the second point, and $(y, z) = (1, 0)$ for the third point). The third column shows evolution plots of the accumulated plastic slip on the six active slip systems 3, 6, 7, 8, 10, and 11, which always act pairwise.

10°. In the course of deformation, the point actually reverts its rotation sense and finally again reaches almost its initial orientation. The principal stress axis at this point is close to a 45° angle, which favors the activation of 3/6 and particularly 10/11, but not 7/8. The reason for slip systems 3 and 6 being activated at a later stage compared to 10/11 can be attributed to the mutual strong collinear interaction, which requires higher stresses for activation. The last point (third row in fig. 8.11) lies close to the surface. The stress axis at this point is nearly aligned with the y axis. Slip systems 7 and 8 become active first, but get less favorable for slip due to the positive lattice rotation around $[1\ 1\ 0]$. Plastic deformation becomes harder and enforces further lattice rotation in order to accommodate for the geometrical constraints of the indenter, finally leading to such high rotations that slip systems 10/11 become favorable for slip and take over as the prevalent carriers of deformation. In general, both the rotations of the lattice and the changing stress state lead to a complex activation behavior of the slip systems.

Rotation As seen in fig. 8.3, the lattice rotation changes abruptly within a few μm across a vertical line below the indenter. More specifically, in the simulation this jump in lattice rotation occurs among neighboring integration points. If there was a gradual change in the rotation, then the lateral mesh resolution of about 5 μm did not suffice to resolve this gradient. Kysar et al. [2010] specify the resolution of their orientation measurements with 3 μm , hence, comparable to our simulation.

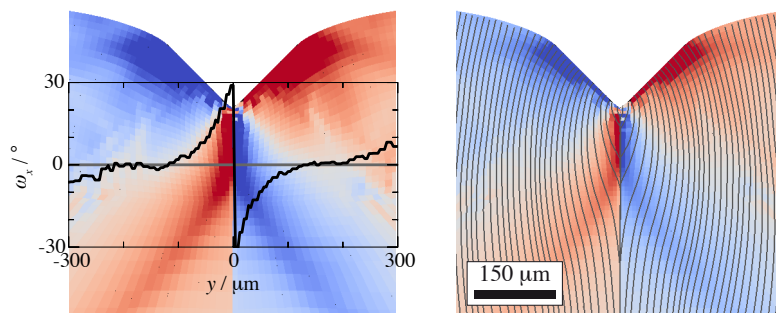


Figure 8.12: Simulated in-plane lattice rotation below a wedge indenter in single-crystalline Nickel. Left: Overlay of a line plot showing the rotation across the central antisymmetry boundary along the gray line. Right: Overlay of the (010) lattice plane traces. The nominal spacing of the traces is 10 μm .

Figure 8.12 shows the lattice rotation jump on a line across the vertical division line. This discontinuity in the lattice rotation evolves due to the left and right half of the crystal rotating away from each other. Figure 8.13 illustrates the evolution of the lattice rotations directly right and left of the boundary as a function of the position under the indenter. The lattice rotations quickly converge towards a maximum value of approximately $\pm 35^\circ$ at about 30 μm below the indenter tip already for small indentation depth Δh . These high rotation differences grow further down into the material, such that at the final indentation depth of $\Delta h = 200 \mu\text{m}$ a boundary length of more than 100 μm reveals a misorientation of

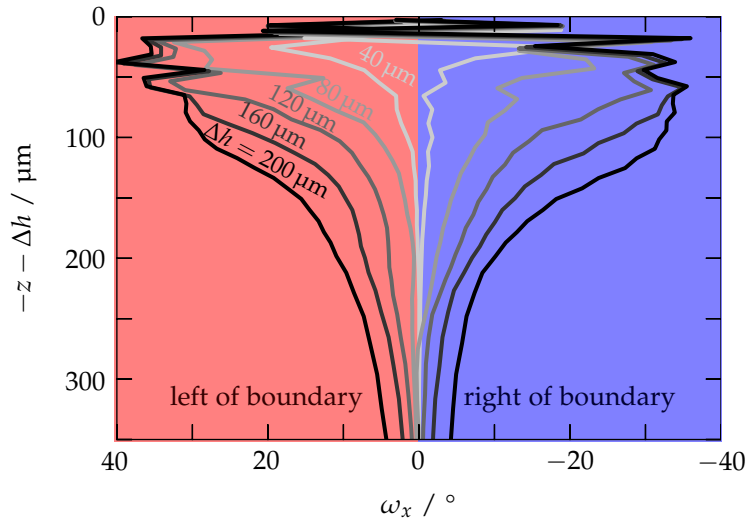


Figure 8.13: Simulated lattice rotation directly left (upper curves) and right (lower curves) of the antisymmetry boundary with evolving indentation depth Δh and along the indentation axis. The origin at $-z - \Delta h = 0$ corresponds to the indenter tip.

70° . Interestingly, this is very close to a $\langle 110 \rangle \Sigma 3$ orientation relationship of 70.5° .

The reason for this large misorientation can be understood when looking at the traces of the (010) lattice planes around the indent shown on the right hand side of fig. 8.12. Although these lattice traces do not correspond to any slip traces in the material,¹⁸ they reflect the curvature of the lattice in general. As seen in fig. 8.6, the specific crystal orientation does not allow for large plastic deformation at the upper indenter flanks, so that the material mainly performs a rigid-body rotation following the inclination angle of the indenter (The orientation dependence of the rotation pattern was already reported by Bouvier and Needleman [2006]). Thus, the (010) plane traces in fig. 8.12 hit the surface at an almost 90° angle. This induces counter-rotations further below in order to compensate for the unrotated lattice in the undeformed regions way below the indenter. The deeper the indenter penetrates into the material the deeper these counter-rotations extent.

The diverging traces of the (010) lattice plane below the indentation axis also indicate that a significant amount of material is transported there. Clearly, this is the material that is pushed away by the indenter above. The compression of material in this region leads to the hydrostatic pressure seen in fig. 8.5.

Excess dislocation density and character of deformation-induced boundary

Since the axis of principal compressive stress changes its direction across the indentation axis, the resolved shear stress on the active slip systems changes sign, and the direction of slip is reverted. Dislocations cannot travel across the indentation axis and become stored there (see third and fourth column of fig. 8.6).¹⁹ This explains why almost the entire dislocation density at the boundary has excess character (compare total and excess density in fig. 8.8). All active slip systems pile up dislocations at the boundary, the majority of dislocations yet has edge character and comes from

¹⁸ Note that the traces in fig. 8.12 should not be confused with slip traces that occur when dislocations leave the surface. Here, the traces simply show the intersection lines of the (010) lattice planes with the image plane.

¹⁹ It should be noted here, that due to the first order upwind formulation of the dislocation transport, dislocations will indeed be pushed across the boundary if the shear rate is zero on the other side. However, they will then not be able to propagate further. So, essentially this will at most result in an inaccuracy of the position of the dislocations by one integration point.

systems 7/8 and 10/11. As indicated by the (010) plane traces in fig. 8.12 these dislocations form a disclination under the indenter. This disclination exerts a stress field that is visible in fig. 8.5 as dark line below the indentation axis. The fact that this stress is still visible after unloading is understandable, because the disclination will not disappear when the external load is released. It should be emphasized that no additional gradient-dependent stress terms were used in this simulation to explicitly induce a stress field by the excess dislocations. Instead, the observed stress arises naturally from an unbalanced flux of dislocations and the accumulation of density that goes along with this and leads to a different strain and stress response.

Influence of the dislocation flux The most obvious effect of the dislocation flux is that it naturally leads to the formation of excess, *i.e.*, GND density. While the GND density is related to a curvature of the crystal lattice, it is not easily possible to (inversely) derive it solely from lattice rotations. Additional assumption have to be made, *e.g.* minimization of line energy or line length. The latter method was used by Kysar et al. [2010] to calculate a lower bound for the GND density from measured lattice orientations. As explained in detail in Kysar et al. [2010], for this special case of plane-strain deformation, this lower bound even corresponds to the exact solution where not more than two effective slip systems are active (which is the case in almost the entire sample). The obtained results fit both qualitatively and quantitatively to the simulated GND densities (see second row of fig. 8.14); this confirms the validity of the predictions from the dislocation transport model. Since the complete deformation history of each slip system is known in the simulation, the GND density can also be derived from a gradient in the dislocation slips. This method was applied to both the simulation results of the dislocation transport model and the local model variant without dislocation transport.²⁰ For the nonlocal simulation, the GND densities derived from slip gradients perfectly match the results as-obtained by the dislocation transport. In contrast, GND densities cannot adequately be reproduced from gradients in slip when dislocation transport is not included in the simulation, as the corresponding map of GND densities reveals (second row and column in fig. 8.14). The local simulation overestimates the GND density with respect to the nonlocal model and even introduces features that are not visible in the experimental results.

The influence of the dislocation transport and generation of GNDs becomes apparent in rows three and four of fig. 8.14, especially with regards to the rotation boundary. In the absence of dislocation transport, no dislocations pile up around the boundary in the local simulation and do not influence the mechanical response. In contrast, for the nonlocal model, the accumulated density at the boundary leads to an increased hardening and higher stresses that

²⁰ The applied method to calculate GNDs from a gradient in slip is described in detail in appendix A.7

are visible as dark line below the indenter (third row of fig. 8.14). It should be emphasized that no additional gradient-dependent stress terms were used in the simulation to explicitly induce a stress field by the excess dislocations. Instead, the observed stress arises naturally from an unbalanced transport of dislocations and the resulting accumulation of density.

In general, the incorporation of the dislocation transport leads to a stiffer response. In the local model, the average equivalent CAUCHY stress in the region of interest shown in fig. 8.14 is 20% lower during loading (yet slightly higher after unloading). This results in higher strains of about 10% with a larger zone of concentrated deformation under the indenter when compared to the nonlocal model.

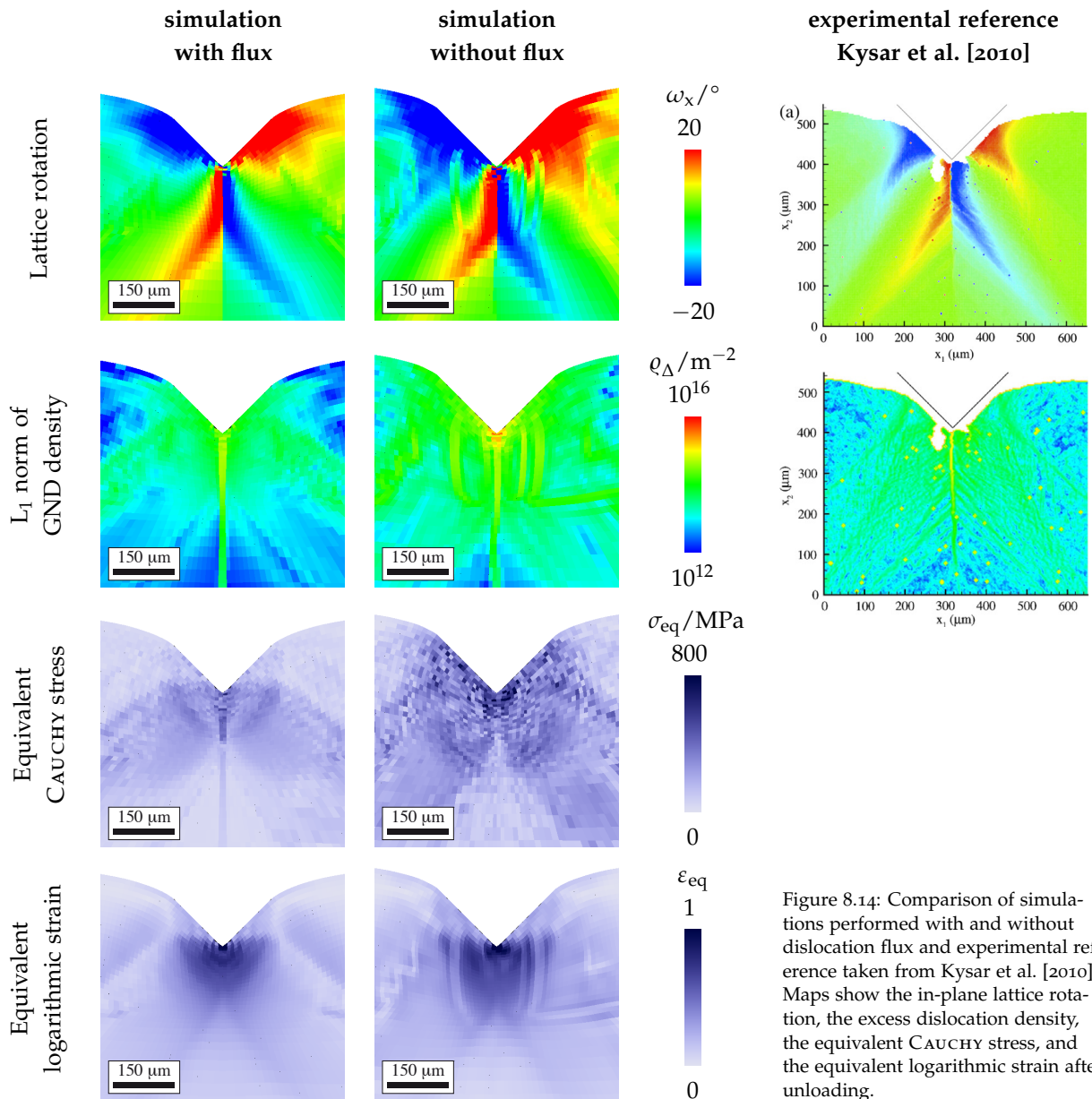


Figure 8.14: Comparison of simulations performed with and without dislocation flux and experimental reference taken from Kysar et al. [2010]. Maps show the in-plane lattice rotation, the excess dislocation density, the equivalent CAUCHY stress, and the equivalent logarithmic strain after unloading.

8.4 Conclusions

- Most of the deformation is concentrated in a region of about the size of the indent around it. Yet, two broad shear-bands form on both sides of the indenter that advance about five times the indentation depth into the material. This is possible due to only two slip systems being active there, so that almost single-glide without pronounced forest hardening is achieved. (figs. 8.4 and 8.9)
- The stress state in the material can be divided into two regions: hydrostatic pressure in a circular area around the indenter tip and more or less uniaxial compressive stress radially pointing away from the central region. The highest uniaxial stresses can be found on the indenter axis and in two broad areas that draw an 45° angle with the indentation axis. (fig. 8.5)
- The plane-strain deformation state prohibits slip on six out of the twelve fcc slip systems, although they partly have the highest theoretical SCHMID factors. The six active slip systems always have to act pairwise in order to achieve a plane-strain deformation.
- From the six active slip systems two systems harden very quickly due to strong collinear interaction and cannot contribute much to deformation. As a result, almost the entire deformation is accommodated by four slip systems, which are mainly active only on either side of the indentation axis, *i.e.*, in most of the volume there are only two systems active at the same time. (figs. 8.6 and 8.7)
- The low dislocation activity at the indenter flanks requires large rigid-body rotations in order to accommodate the geometrical constraints of the indenter, which are also observed in experiment. (fig. 8.3)
- High rotations at the indenter flank induce equally high counter-rotations below the indenter. Due to the symmetry of the orientation and the antisymmetric stress state with respect to the indentation axis, these counter-rotations have different sign on both sides of the indentation axis. (fig. 8.12)
- A high gradient in the lattice rotations on a vertical axis below the indenter arises with a change from $+35^\circ$ to -35° within a distance of at most $5\ \mu\text{m}$; this is in agreement with experimental observations. The jump of 70° is already visible in the simulation after an indentation depth of $80\ \mu\text{m}$. In the following, the magnitude of the jump does not significantly change anymore; however, the lattice rotation jump propagates further into the material along the indentation axis. (figs. 8.12 and 8.13)

- Due to a sign change of the resolved shear stress across the antisymmetry boundary, dislocations pile up on both sides and form a disclination. (figs. 8.8 and 8.12)
- The GNDs at the antisymmetry boundary induce a stress field that is also visible in the unloaded state. This residual stress field cannot be predicted by the local (non-flux) model variant. (fig. 8.14)
- In general, the local model behaves significantly softer than the nonlocal model, *i.e.*, the equivalent CAUCHY stress is on average lower by -20% during loading (yet slightly higher after unloading). This results in higher strains of about $+10\%$. Furthermore, the lattice rotations ($+13\%$) are higher in the local model and are overestimated with respect to the experimental reference values taken from literature. (fig. 8.14)
- GND densities derived from the measured lattice rotations fit both qualitatively and quantitatively to the simulated excess dislocation densities of the nonlocal model. GNDs can also indirectly be determined from spatial gradients in the accumulated plastic slip resolved onto individual slip systems. While this indirect method gives comparable results when applied to the nonlocal simulation results, a local model variant without fluxes overestimates the GND densities significantly ($+215\%$ compared to the nonlocal model). (fig. 8.14)
- While the computational costs of the nonlocal model are significantly higher than for the local model, the obtained solution for the local model contains significant numerical artifacts that are prevented in the nonlocal simulations. In this respect, the dislocation flux seems to naturally balance out numerical inaccuracies and thus improves stability. (fig. 8.14)

Summary and outlook

9

Summary and outlook

A constitutive model of crystal plasticity has been presented that describes the evolution of a crystal's microstructure in terms of dislocation densities of edge and screw type. Both edge and screw dislocation densities can either occur with monopolar properties, *i.e.*, a single dislocation with positive or negative line sense, or with dipolar properties, *i.e.*, two dislocations of opposite line sense combined. The particularity of the model lies in the description of the dislocation density evolution, which not only comprises the usual rate equations for dislocation multiplication, annihilation, and formation and dissociation of dislocation dipoles. Additionally, the spatial redistribution of dislocations by slip is explicitly accounted for. This entails an advection term for the dislocation density that turns the evolution equations for the dislocation density from ordinary into partial differential equations. The associated spatial gradients of the dislocation slip render the model intrinsically nonlocal, *i.e.*, the time integration of the state equations depends on the neighborhood of the integration point. As a result, complete information about the neighbors' states has to be provided at each integration point. The state integration itself employs a first-order upwind scheme that is based on finite volumes attached to each integration point. The constitutive model is coupled to a solver for the mechanical boundary value problem that ensures mechanical equilibrium and compatible strains.

The most essential part of the constitutive model, namely the dislocation transport or flux, has been tested by means of the redistribution of two edge dislocations of opposite signs that are reminiscent of the cross-section through an expanding dislocation loop. In the two-dimensional simulation the two edge dislocations are represented by an equivalent dislocation density that is concentrated at two integration points and surrounded by initially purely elastic integration points without any dislocation content. The results of the simulation show the propagation of the dislocation density through the formerly elastic material and the resulting plastic strain. It has been demonstrated that the dislocation density is conserved in the course of dislocation transport and the plastic strain exactly corresponds to one BURGERS step. Additionally, it has been shown that the stress field of the

dislocations is captured by solving mechanical equilibrium in a compatible continuum in conjunction with the transport of dislocations.

A still heavily debated question is whether such nonlocal theories are able to properly describe the inherently discrete phenomena associated with dislocation slip. As a contribution to this discussion (and also as an additional validation of the model), a comparison between the continuum constitutive model and discrete dislocation dynamics simulations has been made. In order to facilitate comparableness a simple simulation setup had been chosen: a two-dimensional plastic inclusion inside an elastic medium, separated by an impenetrable boundary for dislocations; only one active slip system and only edge type dislocations; no multiplication or annihilation; simple shear deformation by virtue of a homogeneously applied shear stress that is hold until an equilibrated state is reached. Different combinations of applied shear stress, inclusion size, and dislocation density have been used for the simulations. The results showed that the continuum model is able to match the discrete dislocation dynamics results to a large extent. Deviations occur when the size of the inclusion becomes smaller than approximately one micrometer. Then, the discrete dislocation simulations reveal a distinct boundary layer while the continuum model does not. This could be explained by the fact that the continuum model implicitly smears out the BURGERS vector perpendicular to the slip plane, which is equivalent to an infinite number of infinitesimal small BURGERS vectors. This results in a weaker stress field than the one exerted by a discrete number of dislocations. This effect gains importance at scales small enough so that the discrete structure of dislocations becomes apparent. It could also be shown that the concentration of dislocations on a limited number of slip planes amplifies this effect such that the boundary layer becomes larger. A nonlocal backstress term has been introduced, which is inspired by work of Mesarovic et al.¹ and Geers et al.² This backstress term depends on the average slip plane spacing and was able to account for the formation of a boundary layer in the continuum model. Assessment of the average plastic deformation of the inclusion has, however, revealed that the influence of the boundary layer on the average strain is relatively small, so that the backstress term might not be necessary. In a next step, the constitutive model has been applied to two existing experiments. The first is a simple shear test of an Aluminum bi-crystal with small-angle tilt grain boundary.³ Although the transport of dislocations led to accumulation of density around the grain boundary, the influence of the nonlocality of the constitutive model has been found to be rather small—in contrast to earlier simulation approaches to the same experiment by Ma.⁴ The overall agreement between the results from the constitutive model and the experiment is already very good when the dislocation flux is not considered, *i.e.*, the model being purely

¹ S.D. Mesarovic, R. Baskaran, and A. Panchenko. Thermodynamic coarsening of dislocation mechanics and the size-dependent continuum crystal plasticity. *Journal of the Mechanics and Physics of Solids*, 58(3): 311–329, 2010. ISSN 0022-5096. DOI: 10.1016/j.jmps.2009.12.002

² M.G.D. Geers, R.H.J. Peerlings, J.P.M. Hoefnagels, and Y. Kasyanyuk. On a Proper Account of First- and Second-Order Size Effects in Crystal Plasticity. *Adv. Eng. Mater.*, 11(3):143–147, 2009. DOI: 10.1002/adem.200800287

³ J.C. Kuo. *Mikrostrukturmechanik von Bikristallen mit Kippkorn Grenzen*. PhD thesis, RWTH Aachen, 2004

⁴ A. Ma. *Modeling the constitutive behavior of polycrystalline metals based on dislocation mechanisms*. PhD thesis, RWTH Aachen, 2006

local. At least for this rather large-scale problem it has been found that, if the kinematics of dislocation slip for the individual grains is properly described, the solution of mechanical equilibrium in a compatible continuum already suffices to correctly predict the influence of the grain boundary. Consequently, a less sophisticated phenomenological model failed in comparison to predict the influence of the grain boundary.

The second experiment that the model has been applied to is an existing indentation experiment in single-crystalline Nickel.⁵ This specific experiment has been chosen, since its special planar geometry allows to derive the GND density under the indenter from experimentally measured lattice rotations. The lattice rotations obtained in the simulation match the experimentally measured ones to a large extent. Especially, the simulations could predict a high gradient in the lattice rotations on a vertical axis below the indenter with a change from $+30^\circ$ to -30° within a distance of at most $5\ \mu\text{m}$. A local (non-flux) model variant behaved significantly softer than the nonlocal model, *i.e.*, stresses were about 20% lower while strains and lattice rotations were about 10% and 13% higher, respectively. The transport properties of the nonlocal model led to an accumulation of dislocation density on both sides of the boundary below the indenter. Since the model is able to directly predict the GND densities, it was possible to reveal the nature of the disclination that forms at the boundary. The simulated GND densities have been shown to match the GND densities that are derived from the experimentally measured lattice rotations both qualitatively and quantitatively. GNDs have also indirectly been determined from spatial gradients in the accumulated plastic slip resolved onto individual slip systems. While this indirect method gave comparable results when applied to the nonlocal simulation results, a local model variant without fluxes overestimated the GND densities significantly by more than 200% (compared to the nonlocal model). The simulated and measured GNDs at the boundary induce a stress field retained in the unloaded material. Since the local (non-flux) model variant does not account for the accumulation of GNDs at the boundary, it could not properly predict this residual stress field.

In general, the nonlocal constitutive model has been shown to improve model predictions of crystal plasticity dominated by dislocation glide, especially when applied to problems at a scale of less than a millimeter, where the transport of dislocations becomes important. For larger problems the model may still be applicable; yet, the additional effort of solving the flux balance of dislocations then does not have a big influence on the results and local models are probably better suited. For the application to very small-scale problems of less than approximately ten micrometer the model might have to include further terms that take into account the discreteness of slip. In this respect, the application of a backstress that depends on the slip plane spacing has been shown a promising

⁵ J.W. Kysar, Y. Saito, M.S. Oztop, D. Lee, and W.T. Huh. Experimental lower bounds on geometrically necessary dislocation density. *International Journal of Plasticity*, 26(8): 1097–1123, 2010. ISSN 0749-6419. DOI: 10.1016/j.ijplas.2010.03.009

approach. Perhaps even more important, dislocation multiplication can probably not anymore be treated as a strain driven process at these scales, but has to take into account the limited number of available dislocation sources.

One particular strength of the model is the prediction of GND densities, which is not directly accessible in any local constitutive model. Future studies of the influence of the GND density on the plastic response should further exploit this property of the model. Another promising application of the model is the analysis of grain/phase boundary behavior with respect to dislocation glide by altering the transmissivity property of interfaces according to *e.g.* the orientation relationship at the boundary.

Also cyclic loading could be an interesting application of the model, since a Bauschinger effect would automatically arise from the dislocation flux under reversed load.

Appendix

A

Additional material

A.1 Stress and strain measures

The following formulas can be used for conversion of the three stress measures used in this work: the first PIOLA–KIRCHHOFF stress \mathbf{P} , the second PIOLA–KIRCHHOFF stress \mathbf{S} , and the CAUCHY stress $\boldsymbol{\sigma}$.

	\mathbf{P}	\mathbf{S}	$\boldsymbol{\sigma}$
\mathbf{P}	\mathbf{P}	$\det \mathbf{F}_p \mathbf{F}_e \mathbf{S} \mathbf{F}_p^{-T}$	$\det \mathbf{F} \boldsymbol{\sigma} \mathbf{F}^{-T}$
\mathbf{S}	$\frac{1}{\det \mathbf{F}_p} \mathbf{F}_e^{-1} \mathbf{P} \mathbf{F}_p^T$	\mathbf{S}	$\det \mathbf{F}_e \mathbf{F}_e^{-1} \boldsymbol{\sigma} \mathbf{F}_e^{-T}$
$\boldsymbol{\sigma}$	$\frac{1}{\det \mathbf{F}} \mathbf{P} \mathbf{F}^T$	$\frac{1}{\det \mathbf{F}_e} \mathbf{F}_e \mathbf{S} \mathbf{F}_e^T$	$\boldsymbol{\sigma}$

Table A.1: Conversion between different stress measures

A.2 Stress field of a straight edge and screw dislocation

In an infinite and isotropic elastic medium, a straight edge dislocation of infinite length located at the origin with line direction along z and BURGERS vector along x exerts a stress field at point $\mathbf{r} = (x, y)$ given by the following set of equations:¹

$$\sigma_{xx} = -\frac{\mu b}{2\pi(1-\nu)} \frac{y(3x^2 + y^2)}{(x^2 + y^2)^2} \quad (\text{A.1a})$$

$$\sigma_{yy} = \frac{\mu b}{2\pi(1-\nu)} \frac{y(x^2 - y^2)}{(x^2 + y^2)^2} \quad (\text{A.1b})$$

$$\sigma_{zz} = -\frac{\nu \mu b}{\pi(1-\nu)} \frac{y}{x^2 + y^2} \quad (\text{A.1c})$$

$$\sigma_{xy} = \sigma_{yx} = \frac{\mu b}{2\pi(1-\nu)} \frac{x(x^2 - y^2)}{(x^2 + y^2)^2} \quad (\text{A.1d})$$

$$\sigma_{xz} = \sigma_{zx} = \sigma_{yz} = \sigma_{zy} = 0 \quad (\text{A.1e})$$

Similarly, for a straight screw dislocation of infinite length with line direction and BURGERS vector along z and the normal of the habit plane along y exerts a stress field at point $\mathbf{r} = (x, y)$ that is defined

¹ J.P. Hirth and J. Lothe. *Theory of dislocations*. John Wiley & Sons, New York, 1982

by:

$$\sigma_{xz} = \sigma_{zx} = -\frac{\mu b}{2\pi} \frac{y}{x^2 + y^2} \quad (\text{A.2a})$$

$$\sigma_{yz} = \sigma_{zy} = \frac{\mu b}{2\pi} \frac{x}{x^2 + y^2} \quad (\text{A.2b})$$

$$\sigma_{xx} = \sigma_{yy} = \sigma_{zz} = \sigma_{xy} = \sigma_{yx} = 0 \quad (\text{A.2c})$$

A.3 Stable dislocation dipole height

A dislocation dipole forms if two dislocations of character c and opposite sign pass each other in close distance. The passing distance below which a stable dipolar configuration exists is termed stable dislocation dipole height \hat{d}_c . It can be directly derived from the stress field of dislocations given in appendix A.2.

For edge dislocations the stress that drives dislocation motion is defined by the only non-zero shear stress component

$$\tau = Dx \frac{x^2 - d^2}{(x^2 + d^2)^2} \quad \text{with} \quad D = \frac{\mu b}{2\pi(1-\nu)} \quad (\text{A.3})$$

The maximum stress that is felt by a dislocation passing in distance d can be derived by simple differentiation of the stress field with respect to the direction of motion x .

$$\frac{d\tau}{dx} = -D \frac{x^4 - 6d^2x^2 + d^4}{(x^2 + d^2)^3} = 0 \quad (\text{A.4})$$

$$x^4 - 6d^2x^2 + d^4 = 0 \quad (\text{A.5})$$

This quartic equation has four real valued solutions.

$$x = \pm \sqrt{3 \pm 2\sqrt{2}} d \quad (\text{A.6})$$

Inserting these into eq. (A.3) yields the following maximum stress at distance d .

$$\tau = D \frac{1}{4d} \quad (\text{A.7})$$

Now, the stable dipole height \hat{d}_e can be defined as the distance at which the applied stress is just below the stress given in eq. (A.7).

$$\hat{d}_e = \frac{D}{4\tau} = \frac{\mu b}{8\pi(1-\nu)} \frac{1}{\tau} \quad (\text{A.8})$$

Similarly, one can derive the maximum stable dipole height for screw dislocations \hat{d}_s .

$$\hat{d}_s = \frac{D}{4\tau} = \frac{\mu b}{4\pi} \frac{1}{\tau} \quad (\text{A.9})$$

A.4 Partial derivative of the plastic velocity gradient

For the time integration of the stress one needs the derivative of the constitutive function h with respect to the stress expressed by the

second PIOLA–KIRCHHOFF stress. The constitutive function h describes the plastic velocity gradient resulting from combined dislocation glide on all slip systems.

$$h(\mathbf{S}, \boldsymbol{\omega}) = \mathbf{L}_p = \sum_{\xi} \mathbf{L}_p^{\xi} = \sum_{\xi} \dot{\gamma}^{\xi} \mathbf{s}^{\xi} \otimes \mathbf{n}^{\xi} \quad (\text{A.10})$$

Hence, the partial derivative of h with respect to the second PIOLA–KIRCHHOFF stress is defined by the sum of the derivatives of the plastic velocity gradient of the respective slip systems.

$$h(\mathbf{S}, \boldsymbol{\omega})_{,s} = \mathbf{L}_{p,s} = \sum_{\xi} \mathbf{L}_{p,s}^{\xi} \quad (\text{A.11})$$

The single derivatives can be obtained as follows:

$$\begin{aligned} \mathbf{L}_{p,s}^{\xi} &= \left(\dot{\gamma}^{\xi} \mathbf{s}^{\xi} \otimes \mathbf{n}^{\xi} \right)_{,s} \\ &= \left(\mathbf{s}^{\xi} \otimes \mathbf{n}^{\xi} \right) \odot \dot{\gamma}^{\xi}_{,s} \\ &= \partial_{\tau^{\xi}} \dot{\gamma}^{\xi} \left(\mathbf{s}^{\xi} \otimes \mathbf{n}^{\xi} \right) \odot \tau^{\xi}_{,s} \\ &= \partial_{\tau^{\xi}} \dot{\gamma}^{\xi} \left(\mathbf{s}^{\xi} \otimes \mathbf{n}^{\xi} \right) \odot \left(\left(\mathbf{s}^{\xi} \otimes \mathbf{n}^{\xi} \right) : \mathbf{S} \right)_{,s} \\ &= \partial_{\tau^{\xi}} \dot{\gamma}^{\xi} \left(\mathbf{s}^{\xi} \otimes \mathbf{n}^{\xi} \right) \odot \text{sym} \left(\mathbf{s}^{\xi} \otimes \mathbf{n}^{\xi} \right) \end{aligned} \quad (\text{A.12})$$

where symmetry of \mathbf{S} was used in the last row. The corresponding derivative in different tensor notation reads

$$\mathbf{L}_{p,s}^{\xi} = \partial_{\tau^{\xi}} \dot{\gamma}^{\xi} \left(\mathbf{s}^{\xi} \otimes \mathbf{n}^{\xi} \right) \otimes \text{sym} \left(\mathbf{s}^{\xi} \otimes \mathbf{n}^{\xi} \right). \quad (\text{A.13})$$

In the latter two equations the derivative of the plastic slip rate can be obtained by the chainrule.

$$\partial_{\tau^{\xi}} \dot{\gamma}^{\xi} = \rho^{\xi} b \partial_{\tau^{\xi}} v^{\xi} \quad (\text{A.14})$$

Finally, one needs the stress derivate of the dislocation velocity, which is defined in eq. (3.51).

$$\partial_{\tau} v = -v^2 \left(\frac{\partial_{\tau} t_p}{\lambda_p} + \frac{\partial_{\tau} t_s}{\lambda_s} - \frac{\eta \text{sign } \tau}{b \tau_{\text{eff}}^2} \right) \quad (\text{A.15})$$

$$\partial_{\tau} t_p = -t_p \frac{p q V_p}{k_B T} \left(1 - \left(\frac{|\tau_{\text{eff}}|}{\tau_p} \right)^p \right)^{(q-1)} \left(\frac{|\tau_{\text{eff}}|}{\tau_p} \right)^{(p-1)} \text{sign } \tau \quad (\text{A.16})$$

$$\partial_{\tau} t_s = -t_s \frac{p q V_s}{k_B T} \left(1 - \left(\frac{|\tau_{\text{eff}}|}{\tau_s} \right)^p \right)^{(q-1)} \left(\frac{|\tau_{\text{eff}}|}{\tau_s} \right)^{(p-1)} \text{sign } \tau \quad (\text{A.17})$$

A.5 Analysis of the linearized partial differential equation for a dislocation flux with flowstress

One can describe the transport of positive and negative dislocation density under consideration of a flowstress that depends on the

square root of the total density by the following system of first-order nonlinear partial differential equations.

$$\partial_t \varrho - \partial_x ((a - c\sqrt{\varrho}) \kappa) = 0 \quad (\text{A.18a})$$

$$\partial_t \kappa + \partial_x ((a - c\sqrt{\varrho}) \varrho) = 0 \quad (\text{A.18b})$$

where the two constants $a = B\tau$ and $c = \alpha\mu bB$ are used. A linearized version of the latter equation for small perturbations ϱ^* and κ^* around an existing solution ϱ_0 and κ_0 reads

$$\partial_t \varrho^* - (a - c\sqrt{\varrho_0}) \partial_x \kappa^* + \frac{c}{2} \frac{\kappa_0}{\sqrt{\varrho_0}} \partial_x \varrho^* = 0 \quad (\text{A.19a})$$

$$\partial_t \kappa^* + \left(a - \frac{3}{2} c \sqrt{\varrho_0} \right) \partial_x \varrho^* = 0 \quad (\text{A.19b})$$

By differentiation of eq. (A.19a) and substitution of the mixed term by eq. (A.19b) one obtains a second order PDE for ϱ^*

$$\partial_{tt} \varrho^* + (a - c\sqrt{\varrho_0}) \left(a - \frac{3}{2} c \sqrt{\varrho_0} \right) \partial_{xx} \varrho^* + \frac{c}{2} \frac{\kappa_0}{\sqrt{\varrho_0}} \partial_{xt} \varrho^* = 0 \quad (\text{A.20})$$

with coefficients

$$A = 1, \quad B = \frac{c}{2} \frac{\kappa_0}{\sqrt{\varrho_0}}, \quad C = (a - c\sqrt{\varrho_0}) \left(a - \frac{3}{2} c \sqrt{\varrho_0} \right). \quad (\text{A.21})$$

The sign of the discriminant $B^2 - 4AC$ determines the character of the PDE.

$$B^2 - 4AC = \frac{1}{4} c^2 \frac{\kappa_0^2}{\varrho_0} - 6c^2 \varrho_0 + 10ac\sqrt{\varrho_0} - 4a^2 \quad (\text{A.22})$$

After resubstitution of the constants a and c and some simplification one arrives at the following equation for the discriminant.

$$B^2 - 4AC = -4 \left(\tau^2 - \frac{5}{2} \tau \tau_{\text{cr}} + \left(\frac{3}{2} - \frac{1}{16} \frac{\kappa_0^2}{\varrho_0^2} \right) \tau_{\text{cr}}^2 \right) \quad (\text{A.23})$$

The PDE has hyperbolic character if the discriminant is positive. By finding the roots of the quadratic equation eq. (A.23) one can determine the conditions under which this occurs.

$$\left(\frac{5}{4} - \frac{1}{4} \sqrt{1 + \frac{\kappa_0^2}{\varrho_0^2}} \right) \tau_{\text{cr}} < \tau < \left(\frac{5}{4} + \frac{1}{4} \sqrt{1 + \frac{\kappa_0^2}{\varrho_0^2}} \right) \tau_{\text{cr}} \quad (\text{A.24})$$

In this inequality, the ratio of the squares of the excess and total dislocation density can only take values between 0 and 1, namely when either the entire dislocation density is of SSD or GND character. For these two limiting cases one finds:

$$\tau_{\text{cr}} < \tau < 1.5\tau_{\text{cr}} \quad \text{if } \kappa_0 = 0 \quad (\text{A.25})$$

$$0.89\tau_{\text{cr}} < \tau < 1.61\tau_{\text{cr}} \quad \text{if } \kappa_0^2 = \varrho_0^2 \quad (\text{A.26})$$

This means that whenever the resolved shear stress reaches the flowstress and the material starts to become plastic, the linearized PDE turns hyperbolic.

A.6 Active slip systems in an fcc crystal under line load in $[110]$ direction

The stress acting on the material can in general be described in the deformed configuration by a symmetric CAUCHY stress tensor σ .

$$\sigma = \begin{pmatrix} \sigma_{xx} & \sigma_{xy} & \sigma_{xz} \\ \sigma_{xy} & \sigma_{yy} & \sigma_{yz} \\ \sigma_{xz} & \sigma_{yz} & \sigma_{zz} \end{pmatrix} \quad (\text{A.27})$$

The initial orientation of the sample in EULER angles is $\varphi_1 = 315^\circ$, $\phi = 0^\circ$, $\varphi_2 = 0^\circ$. This corresponds to the following orientation matrix \mathbf{O} :

$$\mathbf{O} = \frac{1}{\sqrt{2}} \begin{pmatrix} 1 & -1 & 0 \\ 1 & 1 & 0 \\ 0 & 0 & \sqrt{2} \end{pmatrix}. \quad (\text{A.28})$$

If one assumes lattice rotations to happen exclusively around the sample x -axis (with angle ω), then the combined rotation from the current frame into the lattice frame reads

$$\mathbf{R} = \mathbf{O} \begin{pmatrix} 1 & 0 & 0 \\ 0 & \cos \omega & \sin \omega \\ 0 & -\sin \omega & \cos \omega \end{pmatrix} = \frac{1}{\sqrt{2}} \begin{pmatrix} 1 & -\cos \omega & -\sin \omega \\ 1 & \cos \omega & \sin \omega \\ 0 & -\sqrt{2} \sin \omega & \sqrt{2} \cos \omega \end{pmatrix} \quad (\text{A.29})$$

The second PIOLA-KIRCHHOFF stress is then obtained by rotation of the CAUCHY stress into the lattice frame.

$$\mathbf{S} = \mathbf{R}\sigma\mathbf{R}^T \quad (\text{A.30})$$

The resolved shear stress on any slip system ξ can be calculated from the projection of the second PIOLA-KIRCHHOFF stress onto the SCHMID matrix.

$$\tau^\xi = \mathbf{S} : (\mathbf{s}^\xi \otimes \mathbf{n}^\xi) \quad (\text{A.31})$$

For slip system 1 (numbering according to table 3.1) one obtains

$$\begin{aligned} \tau^1 = \frac{1}{\sqrt{6}} & \left(\sigma_{xx} + \frac{1}{2} \sigma_{yy} \left(-1 + \cos(2\omega) - \frac{1}{\sqrt{2}} \sin(2\omega) \right) \right. \\ & + \frac{1}{2} \sigma_{zz} \left(-1 - \cos(2\omega) + \frac{1}{\sqrt{2}} \sin(2\omega) \right) \\ & + \sigma_{yz} \left(\sin(2\omega) + \frac{1}{\sqrt{2}} \cos(2\omega) \right) \\ & + \sigma_{xy} \left(\cos \omega + \frac{1}{\sqrt{2}} \sin \omega \right) \\ & \left. + \sigma_{xz} \left(\sin \omega - \frac{1}{\sqrt{2}} \cos \omega \right) \right) \quad (\text{A.32}) \end{aligned}$$

Similarly, one obtains for slip system 5

$$\begin{aligned} \tau^5 = \frac{1}{\sqrt{6}} & \left(-\sigma_{xx} - \frac{1}{2}\sigma_{yy} \left(-1 + \cos(2\omega) - \frac{1}{\sqrt{2}} \sin(2\omega) \right) \right. \\ & - \frac{1}{2}\sigma_{zz} \left(-1 - \cos(2\omega) + \frac{1}{\sqrt{2}} \sin(2\omega) \right) \\ & - \sigma_{yz} \left(\sin(2\omega) + \frac{1}{\sqrt{2}} \cos(2\omega) \right) \\ & + \sigma_{xy} \left(\cos \omega + \frac{1}{\sqrt{2}} \sin \omega \right) \\ & \left. + \sigma_{xz} \left(\sin \omega - \frac{1}{\sqrt{2}} \cos \omega \right) \right) \end{aligned} \quad (\text{A.33})$$

If one assumes that the shear stress components in xy and xz are negligible under a line load in x -direction, then the resolved stress on slip systems 1 and 5 are indeed of same absolute value, but opposite sign. Similar results hold for slip system pairs 2/4, 3/6, 7/8, 9/12, and 10/11, which means that they tend to act pairwise. As a consequence of the equally high resolved shear stress on slip systems 1 and 5, the effective plastic velocity of both systems is proportional to the difference in the SCHMID matrices.

$$L_p \propto s^1 \otimes n^1 - s^5 \otimes n^5 = \frac{1}{\sqrt{6}} \begin{pmatrix} 1 & 1 & -1 \\ 1 & 1 & 1 \\ 0 & 0 & -2 \end{pmatrix} \quad (\text{A.34})$$

If one rotates this tensor back into the current configuration, one obtains

$$R^T L_p R \propto \begin{pmatrix} 1 & 1 & 0 \\ -1 & 1 & 0 \\ 0 & 0 & \sqrt{2} \end{pmatrix} \begin{pmatrix} 1 & 1 & 1 \\ 1 & 1 & -1 \\ 0 & 0 & -2 \end{pmatrix} \begin{pmatrix} 1 & -1 & 0 \\ 1 & 1 & 0 \\ 0 & 0 & \sqrt{2} \end{pmatrix} \quad (\text{A.35})$$

$$= \begin{pmatrix} 2 & 0 & 0 \\ 0 & -2 \sin^2 \omega - \frac{1}{\sqrt{2}} \sin(2\omega) & \sqrt{2} \cos^2 \omega + \sin(2\omega) \\ 0 & \sin(2\omega) - \sqrt{2} \sin^2 \omega & \frac{1}{\sqrt{2}} \sin(2\omega) - 2 \cos^2 \omega \end{pmatrix} \quad (\text{A.36})$$

The xx component in this tensor would lead to compression or tension in x direction, which is clearly not possible in plane-strain deformation. Hence, these two slip systems cannot be activated, although they might have a high SCHMID factor. Similar results can be obtained for the slip system pairs 2/4 and 9/12. On the other hand, combined slip on the system pairs 3/6, 7/8, and 10/11 results in a pure plane-strain deformation mode.

A.7 Geometrically necessary dislocation density derived from plastic shear gradients

The amount of geometrically necessary dislocations is closely related to spatial gradients in the plastic slip gradient. It is these

gradients in the plastic strain that necessitate the presence of GNDs in order to maintain compatibility. Thus, if one knows the individual contributions of the plastic shear on all slip systems, one can determine the amount of GNDs. If one integrates the evolution equations for the excess dislocation density of eq. (3.20) one obtains

$$\varrho_{\Delta e}^{\xi} = -\frac{\text{grad } \gamma^{\xi} \cdot \mathbf{s}^{\xi}}{b} \quad (\text{A.37a})$$

for the excess dislocation density of edge type and

$$\varrho_{\Delta s}^{\xi} = -\frac{\text{grad } \gamma^{\xi} \cdot (\mathbf{n}^{\xi} \times \mathbf{s}^{\xi})}{b} \quad (\text{A.37b})$$

for the corresponding screw type. Thus, the GND densities of edge and screw type are proportional to projections of the shear gradients onto the respective directions of motions. The shear gradient can be calculated from central differences with six different neighboring integration points (denoted in the following by an index $i, j \in 1, \dots, 6$). The position of the neighboring integration points in the current configuration is known and denoted by \mathbf{r} . For better readability, two short-hand notations are introduced for the differences between two position vectors and the plastic shears on slip system ξ :

$$\mathbf{r}_{ij} := \mathbf{r}_i - \mathbf{r}_j \quad \text{and} \quad \gamma_{ij}^{\xi} := \gamma_i^{\xi} - \gamma_j^{\xi}. \quad (\text{A.38})$$

The shear difference between two neighbors 1 and 2 can then be derived from the shear gradient.

$$\gamma_{12}^{\xi} = \text{grad } \gamma^{\xi} \cdot (\mathbf{F}_e^{-1} \mathbf{r}_{12}) \quad (\text{A.39})$$

Note that the integration point coordinates are mapped into the lattice frame by means of the elastic deformation gradient \mathbf{F}_e . Similar formulations can be given for four more integration point neighbors and one finally obtains an equation for the plastic shear gradient on a specific slip system.

$$\text{grad } \gamma^{\xi} = \mathbf{F}_e^T \begin{pmatrix} \mathbf{r}_{12} & \mathbf{r}_{34} & \mathbf{r}_{56} \end{pmatrix}^{-T} \begin{pmatrix} \gamma_{12}^{\xi} \\ \gamma_{34}^{\xi} \\ \gamma_{56}^{\xi} \end{pmatrix} \quad (\text{A.40})$$

Inserting the last equation into eq. (A.37) results in an expression for the GND density of edge and screw type on each slip system.

A.8 Efficient cutback algorithm

Algorithm: main cutback and wind forward procedure

```

f = 0
 $\Delta f$  = 2
todo = 1
converges = 0
clearToWindForward = 1
clearToCutback = 1
sync = 0
syncCompleted = 0
enforceCutback = 0
while any todo do
    determine synchronization (see fig. A.2)
    foreach integration point i do
        if converged[i] and clearToWindForward[i] then
             $\Delta f_{old} = \Delta f[i]$ 
             $f[i] = f[i] + \Delta f[i]$ 
             $\Delta f[i] = \min(1 - f[i], \Delta f[i])$ 
            if  $\Delta f[i] > 0$  then
                wind forward variables
                if sync[i] then
                    syncCompleted[i] = 1
                    sync[i] = 0
                    todo[i] = 0
                else todo[i] = 1
            else if  $\Delta f_{old} > 0$  then todo[i] = 0
        else if not converged[i] and clearToCutback[i] then
            if sync[i] then  $\Delta f[i] = \tilde{f}$ 
            else  $\Delta f[i] = 0.5\Delta f[i]$ 
            restore variables
            if  $\Delta f[i] > \Delta f_{min}$  then todo[i] = 1
            else todo[i] = 0
        if todo[i] and (clearToWindForward[i] or
        clearToCutback[i]) then converged[i] = 0
    if any todo then
        do calculations // this will change converge
        todo = 0
    foreach integration point i do
        if not converged[i] and  $\Delta f[i] > f_{min}$  then todo[i] = 1

```

Figure A.1: Algorithm that winds forward or does a cutback.

Algorithm: synchronization

```

if any syncCompleted then
    foreach integration point i do
        if syncCompleted[i] then converged[i] = 0
        syncCompleted[i] = 0
        clearToWindForward[i] = 0
        clearToCutback[i] = not (converged[i])
else
    clearToWindForward[i] = 0
    clearToCutback[i] = 0
    if all converged then
        if all  $f + \Delta f \geq 1$  then clearToWindForward = 1
        else
            foreach integration point i do
                if  $\Delta f$ [i] < 1 then clearToCutback[i] = 1
                else clearToCutback[i] = 0
        else
             $\tilde{f} = \max(f)$ 
            if  $\tilde{f} = 0$  then
                enforceCutback = 0
                foreach integration point i do
                    foreach neighbor n of i do
                        if not converged[n] then enforceCutback[i] = 1
                    foreach integration point i do
                        if enforceCutback[i] then converged[i] = 0
                else
                    sync = 0
                    foreach integration point i do
                        foreach neighbor n of i do
                            if not converged[n] then sync[i] = 1
                        foreach integration point i do
                            if sync[i] then converged[i] = 0
                    foreach integration point i do
                        if  $\Delta f$ [i] < 1 then converged = 0
                if any sync then
                    clearToWindForward[i] = 0
                    clearToCutback[i] = sync[i]
                else
                    foreach integration point i do
                        if not converged[i] then clearToCutback[i] = 1
foreach integration point i do
    if not converged[i] then  $\Delta f$ [i] =  $\min(\Delta f)$ 
    if not (clearToWindForward[i] or clearToCutback[i]) then
        todo[i] = 0
    
```

Figure A.2: Algorithm that determines which integration points do a cutback or wind forward their data.

B

Notation and tensor operations

Vector products

$$c = \mathbf{a} \cdot \mathbf{b} = a^i b^j \mathbf{g}_i \cdot \mathbf{g}_j$$

$$\mathbf{C} = \mathbf{a} \otimes \mathbf{b} = a^i b^j \mathbf{g}_i \otimes \mathbf{g}_j$$

$$c = \mathbf{a} \times \mathbf{b} = a_j b_k \epsilon^{ijk} \mathbf{g}_i$$

$$\mathbf{C} = \mathbf{a} \times \mathbf{B} = a_j B_{kl} \epsilon^{ijk} \mathbf{g}_i \otimes \mathbf{g}_l$$

$$\mathbf{C} = \mathbf{A} \times \mathbf{b} = A_{jk} b_l \epsilon^{ijk} \mathbf{g}_i \otimes \mathbf{g}_l$$

Tensor products

$$\mathbb{C} = \mathbf{A} \otimes \mathbf{B} = A^{ij} B^{kl} \mathbf{g}_i \otimes \mathbf{g}_j \otimes \mathbf{g}_k \otimes \mathbf{g}_l$$

$$\mathbb{C} = \mathbf{A} \odot \mathbf{B} = A^{ij} B^{kl} \mathbf{g}_i \otimes \mathbf{g}_k \otimes \mathbf{g}_l \otimes \mathbf{g}_j$$

$$= A^{il} B^{jk} \mathbf{g}_i \otimes \mathbf{g}_j \otimes \mathbf{g}_k \otimes \mathbf{g}_l$$

$$\mathbb{C} = \mathbf{A} \boxtimes \mathbf{B} = A^{ij} B^{kl} \mathbf{g}_i \otimes \mathbf{g}_k \otimes \mathbf{g}_j \otimes \mathbf{g}_l$$

$$= A^{ik} B^{jl} \mathbf{g}_i \otimes \mathbf{g}_j \otimes \mathbf{g}_k \otimes \mathbf{g}_l$$

Single contraction

$$c = \mathbf{A} \mathbf{b} = A^i{}_j b^j \mathbf{g}_i$$

$$\mathbf{C} = \mathbf{A} \mathbf{B} = A^i{}_k B^{kj} \mathbf{g}_i \otimes \mathbf{g}_j$$

$$\mathbb{C} = \mathbb{A} \mathbf{B} = A^{ijkm} B_m{}^l \mathbf{g}_i \otimes \mathbf{g}_j \otimes \mathbf{g}_k \otimes \mathbf{g}_l$$

Double contraction

$$c = \mathbf{A} : \mathbf{B} = A^{ij} B_{ij}$$

$$\mathbf{C} = \mathbb{A} : \mathbf{B} = A^{ijkl} B_{kl} \mathbf{g}_i \otimes \mathbf{g}_j$$

$$\mathbf{C} = \mathbf{A} : \mathbb{B} = A^{ij} B_{ijkl} \mathbf{g}_k \otimes \mathbf{g}_l$$

$$\mathbb{C} = \mathbb{A} : \mathbb{B} = A^{ijkl} B_{klmn} \mathbf{g}_i \otimes \mathbf{g}_j \otimes \mathbf{g}^m \otimes \mathbf{g}^n$$

$$\mathbf{C} = \mathbb{A} \bullet \mathbf{B} = A^{ijkl} B_{jk} \mathbf{g}_i \otimes \mathbf{g}_l$$

$$\mathbf{C} = \mathbf{A} \bullet \mathbb{B} = A_{il} B^{ijkl} \mathbf{g}_j \otimes \mathbf{g}_k$$

$$\mathbb{C} = \mathbb{A} \bullet \mathbb{B} = A^{ijkl} B_{jmnk} \mathbf{g}_i \otimes \mathbf{g}^m \otimes \mathbf{g}^n \otimes \mathbf{g}_l$$

$$\mathbf{C} = \mathbb{A} \bullet \mathbf{B} = A^{ijkl} B_{il} \mathbf{g}_j \otimes \mathbf{g}_k$$

$$\mathbf{C} = \mathbf{A} \bullet \mathbb{B} = A_{jk} B^{ijkl} \mathbf{g}_i \otimes \mathbf{g}_l$$

$$\mathbb{C} = \mathbb{A} \bullet \mathbb{B} = A^{ijkl} B_{miln} \mathbf{g}^m \otimes \mathbf{g}_j \otimes \mathbf{g}_k \otimes \mathbf{g}^n$$

Table B.1: Tensor operations

Identity tensors
$I = \mathbf{g}_i \otimes \mathbf{g}^i$
$\mathbb{I} = I \otimes I = \mathbf{g}_i \otimes \mathbf{g}^i \otimes \mathbf{g}_j \otimes \mathbf{g}^j$
$\mathbb{I}^R = I \boxtimes I = \mathbf{g}_i \otimes \mathbf{g}^j \otimes \mathbf{g}^i \otimes \mathbf{g}_j$
$\mathbb{I}^L = I \odot I = \mathbf{g}_i \otimes \mathbf{g}_j \otimes \mathbf{g}^j \otimes \mathbf{g}^i$
Identities
$\mathbb{I} \circ \mathbb{A} = \mathbb{A} \circ \mathbb{I} = \mathbb{A}$
$\mathbb{I} \bullet \mathbb{A} = \mathbb{A} \bullet \mathbb{I} = \mathbb{A}$
$\mathbb{I}^R : \mathbb{A} = \mathbb{A} : \mathbb{I}^R = \mathbb{A}$
$\mathbb{I}^R : A = \mathbb{I} \circ A = \mathbb{I} \bullet A = A$
$\mathbb{I}^L : A = \mathbb{I}^R \circ A = \mathbb{I}^R \bullet A = A^T$
$\mathbb{I} : A = \mathbb{I}^L \circ A = \mathbb{I}^L \bullet A = I \operatorname{tr} A$

Table B.2: Second- and fourth-order identity tensors

Basis rearrangement
$\mathbb{A}^R = A^{ijkl} \mathbf{g}_i \otimes \mathbf{g}_l \otimes \mathbf{g}_j \otimes \mathbf{g}_k$
$= A^{iklj} \mathbf{g}_i \otimes \mathbf{g}_j \otimes \mathbf{g}_k \otimes \mathbf{g}_l$
$\mathbb{A}^L = A^{ijkl} \mathbf{g}_i \otimes \mathbf{g}_k \otimes \mathbf{g}_l \otimes \mathbf{g}_j$
$= A^{iljk} \mathbf{g}_i \otimes \mathbf{g}_j \otimes \mathbf{g}_k \otimes \mathbf{g}_l$

Table B.3: Basis rearrangement of fourth-order tensors

Partial derivative
$A_{,B} = \frac{\partial A_{ij}}{\partial B_{kl}} \mathbf{g}^i \otimes \mathbf{g}_k \otimes \mathbf{g}_l \otimes \mathbf{g}^j$
$A_{;B} = \frac{\partial A_{ij}}{\partial B_{kl}} \mathbf{g}^i \otimes \mathbf{g}^j \otimes \mathbf{g}_k \otimes \mathbf{g}_l$
$A_{,B} = (A_{;B})^L$
$A_{;B} = (A_{,B})^R$
Chain and product rule
$A_{,B} = A_{,C} \bullet C_{,B}$
$(AB)_{,C} = A_{,C} B + AB_{,C}$
Special derivatives
$A_{,A} = \mathbb{I}$
$A_{,A^T} = A^T_{,A} = \mathbb{I}^R$
$A^{-1}_{,A} = -A^{-1} \otimes A^{-1}$
$A_{,A^{-1}} = -A \otimes A$
$A^{-T}_{,A} = -A^{-T} \boxtimes A^{-T}$
$A^{-1}_{,A^T} = -A^{-1} \boxtimes A^{-1}$

Table B.4: Derivatives of tensor-valued tensor functions

Bibliography

- A. Arsenlis and D.M. Parks. Modeling the evolution of crystallographic dislocation density in crystal plasticity. *J. Mech. Phys. Solids*, 50(9):1979–2009, 2002. DOI: 10.1016/S0022-5096(01)00134-X.
- A. Arsenlis, D.M. Parks, R. Becker, and V.V. Bulatov. On the evolution of crystallographic dislocation density in non-homogeneously deforming crystals. *J. Mech. Phys. Solids*, 52: 1213–1246, 2004. DOI: 10.1016/j.jmps.2003.12.007.
- M.F. Ashby. The deformation of plastically non-homogeneous materials. *Philosophical Magazine*, 21(170):399–424, 1970. DOI: 10.1080/14786437008238426.
- R. Baskaran, S. Akarapu, S.D. Mesarovic, and H.M. Zbib. Energies and distributions of dislocations in stacked pile-ups. *International Journal of Solids and Structures*, 47(9):1144–1153, 2010. ISSN 0020-7683. DOI: 10.1016/j.ijsolstr.2010.01.007.
- C.J. Bayley, W.A.M. Brekelmans, and M.G.D. Geers. A comparison of dislocation induced back stress formulations in strain gradient crystal plasticity. *Int. J. Solids Struct.*, 43(24):7268–7286, 2006. DOI: 10.1016/j.ijsolstr.2006.05.011.
- A.A. Benzerga, Y. Bréchet, A. Needleman, and E. Van der Giessen. Incorporating three-dimensional mechanisms into dislocation dynamics. *Modelling Simul. Mater. Sci. Eng.*, 12:159–196, 2004.
- B.A. Bilby and E. Smith. Continuous Distributions of Dislocations. III. *Proc. Roy. Soc. London A*, 236(1207):481–505, 1956.
- B.A. Bilby, L.R.T. Gardner, and A.N. Stroh. Continuous distributions of dislocations and the theory of plasticity. In *Proc. 9th Int. Congr. Appl. Mech.*, volume 8, pages 35–44, Bruxelles, 1957. Université de Bruxelles.
- S. Bouvier and A. Needleman. Effect of the number and orientation of active slip systems on plane strain single crystal indentation. *Modelling and Simulation in Materials Science and Engineering*, 14(7): 1105–1125, 2006. ISSN 0965-0393. DOI: 10.1088/0965-0393/14/7/001.
- H.J. Bunge. *Texture Analysis in Materials Science*. Butterworths, London, 1982.

- W. Cai, V.V. Bulatov, T.G. Pierce, M. Hiratani, M. Rhee, M. Bartelt, and M. Tang. *Solid Mechanics and Its Applications*, volume 115, chapter Massively-parallel dislocation dynamics simulations, page 1. Kluwer Academic, Dordrecht, The Netherlands, 2004.
- J.R. Cash and A.H. Karp. A variable order Runge-Kutta method for initial value problems with rapidly varying right-hand sides. *ACM Transactions on Mathematical Software*, 16(3):201–222, 1990. ISSN 0098-3500. DOI: 10.1145/79505.79507.
- K.-S. Cheong and E.P. Busso. Discrete dislocation density modelling of single phase FCC polycrystal aggregates. *Acta Materialia*, 52(19):5665–5675, 2004. DOI: 10.1016/j.actamat.2004.08.044.
- B. Cordero, V. Gómez, A.E. Platero-Prats, M. Revés, J. Echeverría, E. Cremades, F. Barragán, and S. Alvarez. Covalent radii revisited. *Dalton Transactions*, (21):2832–, 2008. ISSN 1477-9226. DOI: 10.1039/b801115j.
- DAMASK. Düsseldorf Advanced Material Simulation Kit. URL <http://damask.mpie.de/>.
- T.P. Darby, R. Schindler, and R.W. Balluffi. On the interaction of lattice dislocations with grain boundaries. *Philosophical Magazine A*, 37(2):245–256, 1978. ISSN 0141-8610. DOI: 10.1080/01418617808235438.
- G. Dehm. Miniaturized single-crystalline fcc metals deformed in tension: New insights in size-dependent plasticity. *Progress in Materials Science*, 54(6):664–688, 2009. ISSN 0079-6425. DOI: 10.1016/j.pmatsci.2009.03.005.
- P. Eisenlohr. *On the role of dislocation dipoles in unidirectional deformation of crystals*. PhD thesis, Universität Erlangen-Nürnberg, 2004.
- P. Eisenlohr, M. Diehl, R.A. Lebensohn, and F. Roters. A spectral method solution to crystal elasto-viscoplasticity at finite strains. *International Journal of Plasticity*, 46:37–53, 2013. DOI: 10.1016/j.ijplas.2012.09.012.
- U. Essmann and H. Mughrabi. Annihilation of dislocations during tensile and cyclic deformation and limits of dislocation densities. *Philosophical Magazine A*, 40(6):731–756, 1979. DOI: 10.1080/01418617908234871.
- Y. Estrin, L.S. Tóth, A. Molinari, and Y. Bréchet. A dislocation based model for all hardening stages in large strain deformation. *Acta Mater.*, 46(15):5509–5522, 1998. DOI: 10.1016/S1359-6454(98)00196-7.
- L.P. Evers. *Strain Gradient Crystal Plasticity based on Dislocation Densities*. PhD thesis, Technische Universiteit Eindhoven, 2003.

- N.A. Fleck, G.M. Muller, M.F. Ashby, and J.W. Hutchinson. Strain gradient plasticity: Theory and experiment. *Acta Metall. Mater.*, 42(2):475–487, 1994. DOI: 10.1016/0956-7151(94)90502-9.
- J. Frenkel. Zur Theorie der Elastizitätsgrenze und der Festigkeit kristallinischer Körper. *Zeitschrift für Physik*, 37:572–609, 1926.
- J. Friedel. *Dislocations*. Addison-Wesley, Reading, Massachusetts, 1964.
- M.G.D. Geers, R.H.J. Peerlings, J.P.M. Hoefnagels, and Y. Kasyanyuk. On a Proper Account of First- and Second-Order Size Effects in Crystal Plasticity. *Adv. Eng. Mater.*, 11(3):143–147, 2009. DOI: 10.1002/adem.200800287.
- G. Gottstein. *Physikalische Grundlagen der Materialkunde*. Springer, Berlin, 2007.
- G. Gottstein and A.S. Argon. Dislocation theory of steady state deformation and its approach in creep and dynamic tests. *Acta Metallurgica*, 35(6):1261–1271, 1987. ISSN 0001-6160. DOI: 10.1016/0001-6160(87)90007-1.
- I. Groma, F.F. Csikor, and M. Zaiser. Spatial correlations and higher-order gradient terms in a continuum description of dislocation dynamics. *Acta Materialia*, 51(5):1271–1281, 2003. ISSN 1359-6454. DOI: 10.1016/S1359-6454(02)00517-7.
- J.P. Hirth and J. Lothe. *Theory of dislocations*. John Wiley & Sons, New York, 1982.
- T. Hochrainer. *Evolving systems of curved dislocations: Mathematical foundations of a statistical theory*. PhD thesis, Universität Karlsruhe (TH), Aachen, 2006.
- T. Hochrainer, M. Zaiser, and P. Gumbsch. A three-dimensional continuum theory of dislocation systems: kinematics and mean-field formulation. *Philosophical Magazine*, 87(8-9):1261–1282, 2007. ISSN 1478-6435. DOI: 10.1080/14786430600930218.
- D. Hull and D.J. Bacon. *Introduction to Dislocations*. Butterworth-Heinemann, 2001.
- J.W. Hutchinson. Bounds and Self-Consistent Estimates for Creep of Polycrystalline Materials. *Proceedings of the Royal Society A: Mathematical, Physical and Engineering Sciences*, 348:101–127, 1976.
- S.R. Kalidindi, C.A. Bronkhorst, and L. Anand. Crystallographic texture evolution in bulk deformation processing of fcc metals. *J. Mech. Phys. Solids*, 40(3):537–569, 1992. DOI: 10.1016/0022-5096(92)80003-9.
- C. Keller, E. Hug, and D. Chateigner. On the origin of the stress decrease for nickel polycrystals with few grains across the thickness. *Materials Science and Engineering: A*, 500(1-2):207–215, 2009. ISSN 0921-5093. DOI: 10.1016/j.msea.2008.09.054.

- U.F. Kocks. Laws for work-hardening and low-temperature creep. *J. Eng. Mater. Tech. (ASME-H)*, 98:76–85, 1976.
- U.F. Kocks, A.S. Argon, and M.F. Ashby. Thermodynamics and Kinetics of Slip. *Progress in Materials Science*, 19:1–291, 1975.
- E. Kröner. *Kontinuumstheorie der Versetzungen und Eigenspannungen*, volume 5 of *Ergebnisse der angewandten Mathematik*. Springer, Berlin, 1958.
- E. Kröner. Allgemeine Kontinuumstheorie der Versetzungen und Eigenspannungen. *Arch. Ration. Mech. An.*, 4:273–334, 1960.
- L. Kubin, B. Devincere, and T. Hoc. Modeling dislocation storage rates and mean free paths in face-centered cubic crystals. *Acta Mater.*, 56(20):6040–6049, 2008. DOI: 10.1016/j.actamat.2008.08.012.
- L.P. Kubin, G. Canova, M. Condat, B. Devincere, V. Pontikis, and Y. Bréchet. Dislocation microstructures and plastic flow: a 3D simulation. *Solid State Phenomena*, 23–24:455–472, 1992.
- J.C. Kuo. *Mikrostrukturmechanik von Bikristallen mit Kippkorngrenzen*. PhD thesis, RWTH Aachen, 2004.
- J. Kysar, Y. Gan, T. Morse, X. Chen, and M. Jones. High strain gradient plasticity associated with wedge indentation into face-centered cubic single crystals: Geometrically necessary dislocation densities. *Journal of the Mechanics and Physics of Solids*, 55(7):1554–1573, 2007. ISSN 0022-5096. DOI: 10.1016/j.jmps.2006.09.009.
- J.W. Kysar, Y. Saito, M.S. Oztog, D. Lee, and W.T. Huh. Experimental lower bounds on geometrically necessary dislocation density. *International Journal of Plasticity*, 26(8): 1097–1123, 2010. ISSN 0749-6419. DOI: 10.1016/j.ijplas.2010.03.009.
- E.H. Lee. Elastic-plastic deformation at finite strains. *J. Appl. Mech. ASME*, 36(1):1–6, 1969.
- E.H. Lee and D.T. Liu. Finite-Strain Elastic—Plastic Theory with Application to Plane-Wave Analysis. *J. Appl. Phys.*, 38(1):19–27, 1967. DOI: 10.1063/1.1708953.
- T.C. Lee, I.M. Robertson, and H.K. Birnbaum. TEM in situ deformation study of the interaction of lattice dislocations with grain boundaries in metals. *Philosophical Magazine A*, 62(1): 131–153, 1990. ISSN 0141-8610. DOI: 10.1080/01418619008244340.
- B. Liu, D. Raabe, P. Eisenlohr, F. Roters, A. Arsenlis, and G. Hommes. Dislocation interactions and low-angle grain boundary strengthening. *Acta Materialia*, 59(19):7125–7134, 2011. ISSN 1359-6454. DOI: 10.1016/j.actamat.2011.07.067.

- X.-D. Liu, S. Osher, and T. Chan. Weighted Essentially Non-oscillatory Schemes. *Journal of Computational Physics*, 115(1): 200–212, 1994. ISSN 0021-9991. DOI: 10.1006/jcph.1994.1187.
- Z.L. Liu, X.M. Liu, Z. Zhuang, and X.C. You. A multi-scale computational model of crystal plasticity at submicron-to-nanometer scales. *International Journal of Plasticity*, 25(8):1436–1455, 2009. ISSN 0749-6419. DOI: 10.1016/j.ijplas.2008.11.006.
- J.D. Livingston and B. Chalmers. Multiple slip in bicrystal deformation. *Acta Metallurgica*, 5(6):322–327, 1957. ISSN 0001-6160. DOI: 10.1016/0001-6160(57)90044-5.
- A. Ma. *Modeling the constitutive behavior of polycrystalline metals based on dislocation mechanisms*. PhD thesis, RWTH Aachen, 2006.
- A. Ma and F. Roters. A constitutive model for fcc single crystals based on dislocation densities and its application to uniaxial compression of aluminium single crystals. *Acta Mater.*, 52(12): 3603–3612, 2004. DOI: 10.1016/j.actamat.2004.04.012.
- S.D. Mesarovic, R. Baskaran, and A. Panchenko. Thermodynamic coarsening of dislocation mechanics and the size-dependent continuum crystal plasticity. *Journal of the Mechanics and Physics of Solids*, 58(3):311–329, 2010. ISSN 0022-5096. DOI: 10.1016/j.jmps.2009.12.002.
- C. Motz, D. Weygand, J. Senger, and P. Gumbsch. Initial dislocation structures in 3-D discrete dislocation dynamics and their influence on microscale plasticity. *Acta Mater.*, 57(6):1744–1754, 2009. DOI: 10.1016/j.actamat.2008.12.020.
- T. Mura. *Micromechanics of Defects in Solids*. Martinus Nijhoff Publishers, Dordrecht, 2nd edition, 1987.
- P.D. Neumann. The interactions between dislocations and dislocation dipoles. *Acta Metall.*, 19(11):1233–1241, 1971. DOI: 10.1016/0001-6160(71)90057-5.
- J.F. Nye. Some geometrical relations in dislocated crystals. *Acta Metall.*, 1(2):153–162, 1953. DOI: 10.1016/0001-6160(53)90054-6.
- E. Orowan. Zur Kristallplastizität I.–III. *Z. Phys.*, 89:605–659, 1934.
- E. Orowan. Problems of plastic gliding. *Proc. Phys. Soc.*, 52(1):8–22, 1940. DOI: 10.1088/0959-5309/52/1/303.
- M. Polanyi. Über eine Art Gitterstörung, die einen Kristall plastisch machen könnte. *Z. Phys.*, 89:660–664, 1934.
- S. Puri, A. Acharya, and A.D. Rollett. Controlling Plastic Flow across Grain Boundaries in a Continuum Model. *Metallurgical and Materials Transactions A*, 42(3):669–675, 2011. ISSN 1073-5623. DOI: 10.1007/s11661-010-0257-8.

- J.R. Rice. Inelastic constitutive relations for solids: an internal variable theory and its application to metal plasticity. *J. Mech. Phys. Solids*, 19:433–455, 1971.
- J.R. Rice. Tensile Crack Tip Fields in Elastic-Ideally Plastic Crystals. *Mechanics of Materials*, 6:317–335, 1987.
- F. Roters, D. Raabe, and G. Gottstein. Work hardening in heterogeneous alloys – a microstructural approach based on three internal state variables. *Acta Materialia*, 48(17):4181–4189, 2000. DOI: 10.1016/S1359-6454(00)00289-5.
- F. Roters, Y.W. Wang, J.C. Kuo, and D. Raabe. Comparison of single crystal simple shear deformation experiments with crystal plasticity finite element simulations. *Adv. Eng. Mater.*, 6(8): 653–656, 2004. DOI: 10.1002/adem.200400079.
- F. Roters, P. Eisenlohr, L. Hantcherli, D.D. Tjahjanto, T.R. Bieler, and D. Raabe. Overview of constitutive laws, kinematics, homogenization, and multiscale methods in crystal plasticity finite element modeling: theory, experiments, applications. *Acta Materialia*, 58:1152–1211, 2010. DOI: 10.1016/j.actamat.2009.10.058.
- A. Roy, R.H.J. Peerlings, M.G.D. Geers, and Y. Kasyanyuk. Continuum modeling of dislocation interactions: Why discreteness matters? *Materials Science and Engineering: A*, 486(1-2):653–661, 2008. ISSN 0921-5093. DOI: 10.1016/j.msea.2007.09.074.
- S. Sandfeld, T. Hochrainer, P. Gumbsch, and M. Zaiser. Numerical implementation of a 3D continuum theory of dislocation dynamics and application to micro-bending. *Philosophical Magazine*, 90(27-28):3697–3728, 2010. ISSN 1478-6435. DOI: 10.1080/14786430903236073.
- S. Sandfeld, T. Hochrainer, M. Zaiser, and P. Gumbsch. Continuum modeling of dislocation plasticity: Theory, numerical implementation, and validation by discrete dislocation simulations. *Journal of Materials Research*, 26(05):623–632, 2011. ISSN 0884-2914. DOI: 10.1557/jmr.2010.92.
- M.D. Sangid, T. Ezaz, H. Sehitoglu, and I.M. Robertson. Energy of slip transmission and nucleation at grain boundaries. *Acta Materialia*, 59(1):283–296, 2011. ISSN 1359-6454. DOI: 10.1016/j.actamat.2010.09.032.
- K.W. Schwarz. Simulations of dislocations on the mesoscopic scale. I. Methods and examples. *J. Appl. Phys.*, 85:108–119, 1999.
- R. Sedláček, J. Kratochvíl, and E. Werner. The importance of being curved: bowing dislocations in a continuum description. *Philosophical Magazine*, 83(31):3735–3752, 2003. ISSN 1478-6435. DOI: 10.1080/14786430310001600213.

- A. Seeger. The Temperature Dependence of the Critical Shear Stress and of Work-hardening of Metal Crystals. *Philosophical Magazine Series 7*, 45(366):771–773, 1954. DOI: 10.1080/14786440708520489.
- Z. Shen, R.H. Wagoner, and W.A.T. Clark. Dislocation and grain boundary interactions in metals. *Acta Metallurgica*, 36(12): 3231–3242, 1988. DOI: 10.1016/0001-6160(88)90058-2.
- J.S. Stölken and A.G. Evans. A microbend test method for measuring the plasticity length scale. *Acta Materialia*, 46(14): 5109–5115, 1998. DOI: 10.1016/S1359-6454(98)00153-0.
- G. Taylor. The Mechanism of Plastic Deformation of Crystals. Part I. Theoretical. *Proceedings of the Royal Society of London. Series A, Containing Papers of a Mathematical and Physical Character (1905-1934)*, 145(855):362–387, 1934. DOI: 10.1098/rspa.1934.0106.
- B. Tippelt, J. Breitschneider, and P. Hähner. The Dislocation Microstructure of Cyclically Deformed Nickel Single Crystals at Different Temperatures. *physica status solidi (a)*, 163(1):11–26, 1997. ISSN 0031-8965. DOI: 10.1002/1521-396X(199709)163:1<11::AID-PSSA11>3.0.CO;2-X.
- M.D. Uchic, D.M. Dimiduk, J.N. Florando, and W.D. Nix. Sample Dimensions Influence Strength and Crystal Plasticity. *Science*, 305(5686):986–989, 2004. ISSN 0036-8075. DOI: 10.1126/science.1098993.
- E. Van der Giessen and A. Needleman. Discrete dislocation plasticity: a simple planar model. *Modelling Simul. Mater. Sci. Eng.*, 3:689–735, 1995.
- V. Volterra. Sur l'équilibre des corps élastiques multiplément connexes. *Ann. Sci. Ecole Norm. Super.*, 24:401–517, 1907.
- D. Walgraef and E.C. Aifantis. On the formation and stability of dislocation patterns—I: One-dimensional considerations. *International Journal of Engineering Science*, 23(12):1351–1358, 1985. DOI: 10.1016/0020-7225(85)90113-2.
- D. Weygand, L.H. Friedman, E. Van der Giessen, and A. Needleman. Aspects of boundary-value problem solutions with three-dimensional dislocation dynamics. *Modelling Simul. Mater. Sci. Eng.*, 10:437–468, 2002.
- S. Yefimov. *Discrete dislocation and nonlocal crystal plasticity modelling*. PhD thesis, Rijksuniversiteit Groningen, 2004.
- N. Zaafarani. *Experimental and theoretical investigation of nanoindentation in a Cu-single crystal*. PhD thesis, RWTH Aachen, 2008.
- H.M. Zbib, M. Rhee, and J.P. Hirth. On plastic deformation and the dynamics of 3D dislocations. *Int. J. Mech. Sci.*, 40:113–127, 1998.

M. Zehetbauer and V. Seumer. Cold Work Hardening in Stages IV and V of f.c.c. Metals – I. Experiments and Interpretation. *Acta Metallurgica et Materialia*, 41:577–588, 1993. DOI: 10.1016/0956-7151(93)90088-A.

Abstract

This dissertation presents a physics-based constitutive model of dislocation glide in metals that explicitly accounts for the redistribution of dislocations due to their motion. In this respect, it is settled between a) discrete dislocation dynamics models, which solve the equation of motion for every discretely represented dislocation segment by superposition of all dislocation stress fields, and b) local continuum dislocation-based models of crystal-plasticity, which represent the dislocation content by a dislocation density field and solve for mechanical equilibrium in a compatible medium. The model parametrizes the complex microstructure by dislocation densities of edge and screw character, which either occur with monopolar properties, *i.e.*, a single dislocation with positive or negative line sense, or with dipolar properties, *i.e.*, two dislocations of opposite line sense combined. The particularity of the model lies in the description of the dislocation density evolution, which not only comprises the usual rate equations for dislocation multiplication, annihilation, and formation and dissociation of dislocation dipoles. Additionally, the spatial redistribution of dislocations by slip is explicitly accounted for. This entails an advection term for the dislocation density that turns the evolution equations for the dislocation density from ordinary into partial differential equations. The associated spatial gradients of the dislocation slip render the model intrinsically nonlocal, *i.e.*, the time integration of the state equations depends on the neighborhood of the integration point.

After an assessment of the transport properties of the constitutive model, the predictions for a simple test case are compared to discrete dislocation dynamics results of the same setup. It is discussed what happens at the transition from the discrete to the continuum description. It is found that the continuum model is able to match the discrete dislocation dynamics results to a large extent.

The model is applied to two existing experiments: simple shear of an Aluminum bi-crystal with small-angle tilt grain boundary¹ and indentation in single-crystalline Nickel.² Both simulations reveal a very good match between model predictions and experimental data. It is found that for the large scale simple shear experiment the redistribution of the dislocation density has, however, little influence on the plastic response, and the influence of the grain

¹ J.C. Kuo. *Mikrostrukturmechanik von Bikristallen mit Kippkorngrenzen*. PhD thesis, RWTH Aachen, 2004

² J.W. Kysar, Y. Saito, M.S. Oztog, D. Lee, and W.T. Huh. Experimental lower bounds on geometrically necessary dislocation density. *International Journal of Plasticity*, 26(8): 1097–1123, 2010. ISSN 0749-6419. DOI: 10.1016/j.ijplas.2010.03.009

boundary is already captured by a local model variant without dislocation transport, yet not for a phenomenological constitutive model. This is in contrast to previous results that indicated the need of a *nonlocal* model in order to properly represent the grain boundary behavior.³ In the simulation of the Nickel indent, the dislocation transport led to accumulation of GND density around a vertical boundary with a high orientation gradient below the indenter that is decisive for the plastic material response. A local model variant without dislocation transport is shown to behave significantly softer, which results in an overestimation of the lattice rotations compared to experiment.

³ A. Ma. *Modeling the constitutive behavior of polycrystalline metals based on dislocation mechanisms*. PhD thesis, RWTH Aachen, 2006

Zusammenfassung

In dieser Dissertation wird ein physikalisch-basiertes konstitutives Materialmodell für Versetzungsgleitung in Metallen entwickelt, das den Transport von Versetzungen explizit berücksichtigt. Das Modell ist angesiedelt an der Schnittstelle zwischen a) diskreten Versetzungsmodellen, die die Versetzungslinien durch diskrete Segmente darstellen und die dazugehörigen Bewegungsgleichungen mittels der Spannungsfelder der Versetzungen bestimmen und b) lokalen versetzungs-basierten Kristallplastizitätsmodellen, die Versetzungen durch Versetzungsdichte modellieren und die mechanischen Gleichgewichtsbedingungen in einem kompatiblen Medium lösen. Das Modell parametrisiert die Mikrostruktur durch Versetzungsdichten mit Stufen- oder Schraubencharakter, die entweder mit monopolen Eigenschaften auftreten, das heisst einzelne Versetzungen mit positiver beziehungsweise negativer Linienrichtung, oder als Versetzungsdipol. Die Besonderheit des Modells liegt in der Beschreibung der Versetzungsdichteevolution, die nicht nur die gewöhnlichen Ratengleichungen für Multiplikation, Annihilation und Bildung und Zerfall von Dipolen beinhaltet. Zusätzlich wird die Umverteilung von Versetzungsdichte berücksichtigt. Dies führt zu einem Transportterm, der den Charakter der Evolutionsgleichungen von gewöhnlichen Differentialgleichungen zu partiellen Differentialgleichungen ändert. Die dadurch auftretenden räumlichen Ableitungen der plastischen Scherung bedingen eine Nichtlokalität des Modells, das heisst die Zeitintegration der Evolutionsgleichungen hängt von der Nachbarschaft jedes Integrationspunktes ab.

Anhand eines Vergleiches der Modellvorhersagen mit diskreten Versetzungsrechnungen für einen einfachen Testfall wird diskutiert, welche Effekte beim Übergang von einer diskreten zu einer Kontinuumbeschreibung von Versetzungsbewegung auftreten. Ein Resultat ist, dass die Vorhersagen des Kontinuumsmodells in guter Übereinstimmung mit dem diskreten Modell stehen.

Das Modell wird im Anschluss auf zwei existierende Experimente angewendet: die Scherverformung eines Aluminium Bikristalls mit Kleinwinkel-Kippkorngrenze⁴ und die Indentierung von einkristallinem Nickel.⁵ Beide Simulationen zeigen gute Übereinstimmung mit den Experimenten. Dabei zeigt sich, dass der

⁴ J.C. Kuo. *Mikrostrukturmechanik von Bikristallen mit Kippkorngrenzen*. PhD thesis, RWTH Aachen, 2004

⁵ J.W. Kysar, Y. Saito, M.S. Oztog, D. Lee, and W.T. Huh. Experimental lower bounds on geometrically necessary dislocation density. *International Journal of Plasticity*, 26(8): 1097–1123, 2010. ISSN 0749-6419. DOI: 10.1016/j.ijplas.2010.03.009

Einfluss des Versetzungstransportes auf das Verformungsverhalten beim großskaligen Scherversuch gering ist, da der Einfluss der Korngrenze schon durch eine lokale Modellvariante ohne Versetzungstransport beschrieben werden kann. Dies steht in teilweiseem Widerspruch zu früheren Ergebnissen, die darauf hindeuteten, dass das Verhalten der Korngrenze nur durch einen nichtlokalen Ansatz beschrieben werden kann.⁶ In der Simulation der Indentierung von Nickel führt der Transport von Versetzungen zu einem Aufstau von geometrisch notwendigen Versetzungen an einer vertikalen Grenze unterhalb des Indenters, die einen hohen Orientierungsgradienten aufweist und entscheidend für das Verformungsverhalten der Probe ist. Eine lokale Modellvariante ohne Versetzungstransport führt zu einem signifikant weicherem Materialverhalten und einer Überschätzung der Gitterrotationen im Vergleich zum Experiment.

⁶ A. Ma. *Modeling the constitutive behavior of polycrystalline metals based on dislocation mechanisms*. PhD thesis, RWTH Aachen, 2006